

VOLUME 35

JANUARY 1957

NUMBER 1

Canadian Journal of Physics

Editor: H. E. DUCKWORTH

Associate Editors:

L. G. ELLIOTT, *Atomic Energy of Canada, Ltd., Chalk River*

J. S. FOSTER, *McGill University*

G. HERZBERG, *National Research Council of Canada*

L. LEPRINCE-RINGUET, *Ecole Polytechnique, Paris*

B. W. SARGENT, *Queen's University*

G. M. VOLKOFF, *University of British Columbia*

W. H. WATSON, *University of Toronto*

G. A. WOONTON, *McGill University*

**Published by THE NATIONAL RESEARCH COUNCIL
OTTAWA CANADA**

CANADIAN JOURNAL OF PHYSICS

(Formerly Section A, Canadian Journal of Research)

Under the authority of the Chairman of the Committee of the Privy Council on Scientific and Industrial Research, the National Research Council issues THE CANADIAN JOURNAL OF PHYSICS and six other journals devoted to the publication, in English or French, of the results of original scientific research. Matters of general policy concerning these journals are the responsibility of a joint Editorial Board consisting of: members representing the National Research Council of Canada; the Editors of the Journals; and members representing the Royal Society of Canada and four other scientific societies.

EDITORIAL BOARD

Representatives of the National Research Council

A. N. Campbell, *University of Manitoba*
G. E. Hall, *University of Western Ontario*
W. H. Watson (Chairman), *University of Toronto*
H. G. Thode, *McMaster University*
D. L. Thomson, *McGill University*

Editors of the Journals

D. L. Bailey, *University of Toronto*
T. W. M. Cameron, *Macdonald College*
H. E. Duckworth, *McMaster University*
R. G. E. Murray, *University of Western Ontario*
K. A. C. Elliott, *Montreal Neurological Institute*
G. A. Ledingham, *National Research Council*
Léo Marion, *National Research Council*

Representatives of Societies

D. L. Bailey, *University of Toronto*
Royal Society of Canada
T. W. M. Cameron, *Macdonald College*
Royal Society of Canada
H. E. Duckworth, *McMaster University*
Royal Society of Canada
Canadian Association of Physicists
K. A. C. Elliott, *Montreal Neurological Institute*
Canadian Physiological Society
R. G. E. Murray, *University of Western Ontario*
Canadian Society of Microbiologists
H. G. Thode, *McMaster University*
Chemical Institute of Canada
T. Thorvaldson, *University of Saskatchewan*
Royal Society of Canada

Ex officio

Léo Marion (Editor-in-Chief), *National Research Council*
F. T. Rosser, Director, Division of Administration, *National Research Council*

Manuscripts for publication should be submitted to Dr. Léo Marion, Editor-in-Chief, Canadian Journal of Physics, National Research Council, Ottawa 2, Canada.

(For instructions on preparation of copy, see **Notes to Contributors** (inside back cover).)

Proof, correspondence concerning proof, and orders for reprints should be sent to the Manager, Editorial Office (Research Journals), Division of Administration, National Research Council, Ottawa 2, Canada.

Subscriptions, renewals, requests for single or back numbers, and all remittances should be sent to Division of Administration, National Research Council, Ottawa 2, Canada. Remittances should be made payable to the Receiver General of Canada, credit National Research Council.

The journals published, frequency of publication, and prices are:

Canadian Journal of Biochemistry and Physiology	Monthly	\$3.00 a year
Canadian Journal of Botany	Bimonthly	\$4.00 a year
Canadian Journal of Chemistry	Monthly	\$5.00 a year
Canadian Journal of Microbiology	Bimonthly	\$3.00 a year
Canadian Journal of Physics	Monthly	\$4.00 a year
Canadian Journal of Technology	Bimonthly	\$3.00 a year
Canadian Journal of Zoology	Bimonthly	\$3.00 a year

The price of single numbers of all journals is 75 cents.

Canadian Journal of Physics

Editor: H. E. DUCKWORTH

Associate Editors:

L. G. ELLIOTT, *Atomic Energy of Canada, Ltd., Chalk River*
J. S. FOSTER, *McGill University*
G. HERZBERG, *National Research Council of Canada*
L. LEPRINCE-RINGUET, *Ecole Polytechnique, Paris*
B. W. SARGENT, *Queen's University*
G. M. VOLKOFF, *University of British Columbia*
W. H. WATSON, *University of Toronto*
G. A. WOONTON, *McGill University*

**Published by THE NATIONAL RESEARCH COUNCIL
OTTAWA CANADA**

THE
JOURNAL OF
THE
ROYAL ANTHROPOLOGICAL INSTITUTE
OF GREAT BRITAIN AND IRELAND
VOLUME 100 PART 1 2000

Canadian Journal of Physics

Issued by THE NATIONAL RESEARCH COUNCIL OF CANADA

VOLUME 35

JANUARY 1957

NUMBER 1

HIGHER-ORDER FOCUSING IN THE $\pi\sqrt{2}$ β -SPECTROMETER¹

G. E. LEE-WHITING AND E. A. TAYLOR

ABSTRACT

The expansion coefficients of that magnetic field which gives best focusing in the high-aperture double-focusing spectrometer have been determined to the sixth order. The analytical calculations have been checked by numerical integration of the equations of the orbits. The third- and fourth-order coefficients published by Stoker *et al.* (1954) are not in agreement with our results.

1. INTRODUCTION

It seems to be admitted universally that the double-focusing principle introduced into β -spectrometry by Svartholm and Siegbahn (1946) is most advantageous. The flat field of the original 180° type is replaced by an inhomogeneous field having the correct slope at the central orbit to produce first-order radial focusing after an angle of $\pi\sqrt{2}$ radians. For this particular value of the slope, $\alpha = -\frac{1}{2}$ in the notation of Siegbahn (1955), first-order axial focusing also occurs, bringing the great benefit of a much reduced image height. The question of the best value of the coefficient of the quadratic term in the expansion of the magnetic field, β in the notation of Siegbahn, is not so easily answered. The choices $\beta = \frac{1}{4}$, $\frac{1}{2}$, and $\frac{3}{4}$ have been suggested. We shall show that both $\frac{1}{4}$ and $\frac{3}{4}$ are superior to $\frac{1}{2}$ when a rectangular aperture is used, except possibly at very high transmission. The decision between $\frac{1}{4}$ and $\frac{3}{4}$ is not so clear-cut, though there are several minor advantages to be gained by adopting the latter. For either choice, but for no other, it is possible to bring about a great improvement in transmission by employing higher-order focusing. Higher-order focusing requires a more accurate control of the field shape. Though the accuracy required may not be possible with an iron-cored instrument, there is no obvious reason why focusing to say the fourth order should not be possible with air-cored coils. In addition, iron-free spectrometers have other well-known advantages. Moussa and Bellicard (1954) and Siegbahn and Edvarson (1956) have succeeded in building double-focusing spectrometers with different types of air-cored coils.

A spectrometer with higher-order focusing based on the choice $\beta = \frac{1}{4}$ will have a much reduced radial aberration for those orbits lying near the plane of symmetry. The theory of such spectrometers has been given by many

¹Manuscript received September 11, 1956.

Contribution from Chalk River Laboratory, Atomic Energy of Canada Limited, Chalk River, Ontario. Issued as A.E.C.L. No. 373.

authors; we give references in Section 3. A spectrometer with higher-order focusing based on the choice $\beta = \frac{1}{2}$ favors orbits lying near the right cylinder standing on the central orbit. Our main purpose in writing this paper is to give the optimum field parameters as far as the sixth order. Though it may not be possible to fit the field beyond the fourth order, the fifth- and sixth-order terms should at least be useful in calculating the residual aberrations. Our parameters, which do not agree with the fourth-order results of Stoker *et al.* (1954), are confirmed by numerical integration of the equations of the orbits. The optimum field form is very close to $r^{-\frac{1}{2}}$, the shape approximated by the solenoids of Siegbahn and Edvarson (1956).

In undertaking the complex problem of a higher-order orbit calculation it is well to begin with a systematic treatment of the properties of the various expansion coefficients of the magnetic field. Such a discussion is given in Section 2. The first- and second-order properties of the spectrometer are reviewed in some detail in Section 3 in order to permit us to give a reasonable discussion of the advantages of the different choices for β . The results of the higher-order calculations are presented in Sections 4 and 5.

Following Svartholm (1946) we eliminate the time from the equations of motion and obtain differential equations in the spatial variables for the electron orbits. These differential equations are solved by a method of successive approximations.

2. DESCRIPTION OF THE MAGNETIC FIELD

We restrict our discussion to magnetic fields having an axis of cylindrical symmetry perpendicular to a plane of symmetry. Assume a cylindrical coordinate system (r, ϕ, z) with its z -axis in the axis of symmetry and its origin in the plane of symmetry. For the magnetic fields under discussion only the ϕ -component of the vector-potential is non-zero; call this component A . The radial and axial components of the magnetic field are then

$$(1) \quad \mathfrak{H}_r(r, z) = -\frac{\partial A}{\partial z},$$

$$(2) \quad \mathfrak{H}_z(r, z) = \frac{1}{r} \frac{\partial rA}{\partial r}.$$

In a shaped-field β -spectrometer the source and detector will be located on a particular circle in the plane of symmetry centered at the origin. We call this circle the optic circle. Its radius, a fixed parameter of the spectrometer, we represent by the symbol r_0 . Stationary motion on the optic circle can exist for electrons of a given wholly tangential momentum, say p_0 , if the field at the optic circle, \mathfrak{H}_0 , is adjusted to satisfy the relation

$$(3) \quad \mathfrak{H}_z(r_0, 0) \equiv \mathfrak{H}_0 = -p_0(e r_0)^{-1}.$$

We shall use differential equations for the electron orbits in the form given by Svartholm (1946). The properties of the magnetic field enter these equations only through the product rA . A method of finding the coefficients in a certain

expansion of this product is the chief business of this section. It is convenient to transform from the coordinates (r, z, ϕ) to the coordinates (η, τ, ψ) defined by

$$(4) \quad \eta = (r - r_0)/r_0, \quad \tau = z/r_0, \quad \psi = \phi/\sqrt{2}.$$

We write the vector-potential in the neighborhood of the optic circle in the form

$$(5) \quad rA = r_0 A_0 + \frac{1}{2} r_0^2 \sum_{m,n=0}^{\infty} c_{mn} \tau^m \eta^n,$$

in which $c_{00} = 0$. Since $z = 0$ is a plane of symmetry, the coefficients with m odd are necessarily zero. We demand that $c_{01} = 1$, in order that the field on the optic circle derived from (5) be consistent with stationary motion on the optic circle of electrons with tangential momentum p_0 , i.e. in order that (3) be satisfied. The differential equations for the orbits depend on the initial conditions. Let us consider an orbit for which $\eta = h$, $\tau = t$, $\eta' = H$, and $\tau' = T$ at $\psi = 0$. The angle between the initial momentum vector and the tangent to the optic circle at $\psi = 0$, γ , is given by the relation

$$(6) \quad \cos \gamma = [1 + \frac{1}{2}(1+h)^{-2}(H^2 + T^2)]^{-\frac{1}{2}}.$$

Let the absolute value of the momentum of the electron in question be $p = p_0(1+\epsilon)$. We shall need the function F defined by

$$(7) \quad F = (1+\epsilon)(1+h)\cos \gamma + \sum_{m,n} c_{mn}(\tau^m \eta^n - t^m h^n),$$

and its derivatives as defined by

$$(8) \quad P \equiv \frac{\partial F}{\partial \eta}, \quad Q \equiv \frac{\partial F}{\partial \tau}.$$

The differential equations for the orbits are

$$(9) \quad \eta'' + \left[\frac{P}{F} \eta' + \frac{Q}{F} \tau' - \frac{2}{1+\eta} \eta' \right] \eta' = -2 \left[(1+\eta)^2 \frac{P}{F} - 1 - \eta \right],$$

$$(10) \quad \tau'' + \left[\frac{P}{F} \eta' + \frac{Q}{F} \tau' - \frac{2}{1+\eta} \eta' \right] \tau' = -2(1+\eta)^2 \frac{Q}{F}.$$

For $\epsilon = 0$ these equations are identical with Svartholm's equations (18).

The coefficients c_{mn} introduced in (5) are not all independent. Of the two Maxwell equations applicable to a static magnetic field *in vacuo*, one is automatically satisfied by a field derived from a vector-potential. Under the symmetry here imposed the other reduces to

$$(11) \quad \frac{\partial \mathfrak{F}_r}{\partial \tau} = \frac{\partial \mathfrak{F}_z}{\partial \eta}.$$

By substituting (1) and (2) derived from (5) in (11) and equating coefficients of $\tau^m \eta^n$ from the two sides of the equation, we obtain

$$(12) \quad (m+2)(m+1)[c_{m+2, n+1} + c_{m+2, n}] = -(n+2)[(n+3)c_{m, n+3} + nc_{m, n+2}]$$

valid for $n \geq 0$, and

$$(13) \quad (m+2)(m+1)c_{m+2, 0} = -2c_{m2} + c_{m1}.$$

It follows from (12) and (13) that, given c_{mn} for fixed m and all n , we can compute $c_{m+2, n}$ for all n . For, after using relation (13) to find $c_{m+2, 0}$ in terms of known quantities, one can employ (12) as a recurrence relation to increase the value of n in unit steps. Thus we have shown that the matrix of coefficients c_{mn} is completely determined when we fix the row c_{0n} . Since Maxwell's equations have been satisfied, the coefficients c_{0n} are independent.

The variation with r of the field intensity in the equatorial plane, i.e. the function $\Phi_z(r, 0)$, is customarily used to describe the magnetic field of a β -spectrometer. To show that a knowledge of this function is equivalent to a knowledge of the set of coefficients c_{0n} , we expand the function about the point $r = r_0$:

$$(14) \quad \Phi_z(r, 0) = \Phi_0 \sum_{n=0}^{\infty} a_n \eta^n.$$

In order that (14) should satisfy (3), we must make the definition $a_0 = 1$. (The coefficients a_n defined by (14) are identical with those used by Stoker *et al.* (1954). The α and β of Siegbahn (1955) are a_1 and a_2 respectively; the α and β of Shull and Dennison (1947) are $-a_1$ and a_2 respectively. The coefficient a_3 used by Svartholm is our c_{03} .) By equating expressions (2) and (14) for $\Phi_z(r, 0)$ it is not difficult to show that

$$(15) \quad nc_{0n} = a_{n-1} + a_{n-2}$$

for $n \geq 2$; the relation is true for $n = 1$ too, if we make the definition $a_{-1} = 0$. From (15) the set c_{0n} may be calculated if we are given the set a_n . Conversely, since $a_0 = 1$, we may use (15) as a recurrence relation to generate the a_n from the c_{0n} . Hence the properties of the magnetic field in the neighborhood of the optic circle are completely and uniquely defined by either set of independent coefficients, the c_{0n} or the a_n .

There are several relations between the c_{mn} and the a_n which are useful in checking results obtained by the equations already given. In cylindrical coordinates the equation $\text{div } \vec{\Phi} = 0$ becomes

$$(16) \quad \frac{1}{r} \frac{\partial}{\partial r} (r\Phi_r) + \frac{\partial \Phi_z}{\partial z} = 0.$$

Differentiation of (16) with respect to z and the use of (11) leads to

$$(17) \quad -(1+\eta) \frac{\partial^2 \Phi_z}{\partial r^2} = \frac{\partial \Phi_z}{\partial \eta} + (1+\eta) \frac{\partial^2 \Phi_z}{\partial \eta^2}.$$

We shall use this relation in the special case $r = 0$. By substituting the Φ_z obtained from (2) in the left-hand side of (17) and that of (14) in the right-hand side we obtain

$$(18) \quad -2c_{2n} = na_n + (n+1)a_{n+1}.$$

Simple expressions analogous to (15) and (18) do not seem to exist for $m > 2$. Relation (19), the inverse of (15), is easily obtained either directly from the definitions or from (15):

$$(19) \quad a_n = \sum_{r=0}^n (-)^{n-r} (r+1) c_{0, r+1}.$$

In the design of spectrometers built with iron-cored coils the set of coefficients a_n is probably the most useful description of the field. For air-cored coils, on the other hand, convenient expressions are available for the vector-potential itself. We have found that the independent set of coefficients which is most easily computed from coil dimensions is not the c_{0n} , but is the one defined by c_{m0} , c_{m1} ; the rest of the matrix and the a_n may be obtained by using (12), (13), and (15) as recurrence relations in n .

3. SECOND-ORDER SOLUTION

To solve equations (9) and (10) we use the method suggested by Svartholm (1946). It is assumed the H , T , h , t , and ϵ are all small compared to unity. If we retain terms in (9) and (10) as far as the first order only, then the approximate equations (20) are the result:

$$(20a) \quad \eta'' + \omega_1^2 = 2\epsilon,$$

$$(20b) \quad \tau'' + \omega_2^2 \tau = 0.$$

We have made the definitions $\omega_1^2 = 4c_{02}$ and $\omega_2^2 = 4c_{20}$. The solutions of (20) corresponding to orbits originating in a point source on the optic circle at $\psi = 0$ are:

$$(21a) \quad \eta = \omega_1^{-1} H \sin(\omega_1 \psi) + 2\epsilon \omega_1^{-2} [1 - \cos(\omega_1 \psi)],$$

$$(21b) \quad \tau = \omega_2^{-1} T \sin(\omega_2 \psi).$$

Double, i.e. two-directional, focusing occurs in the plane $\psi = \psi_0$, if

$$(22) \quad \omega_1 \psi_0 = \omega_2 \psi_0 = \pi.$$

The coefficients c_{02} and c_{20} , upon which ω_1 and ω_2 depend, are not independent, being related through

$$(23) \quad c_{02} + c_{20} = \frac{1}{2},$$

which relation is readily obtained from (13) in the special case $m = 0$. The unique solution of equations (22) and (23) is $c_{02} = c_{20} = \frac{1}{4}$, $\psi_0 = \pi$. From (15) it is easily shown that

$$(24) \quad 2c_{02} = 1 + a_1.$$

Thus double-focusing occurs, as Svartholm and Siegbahn (1946) discovered, for $a_1 = -\frac{1}{2}$; the focal plane is situated at $\phi_0 = \psi_0 \sqrt{2} = \pi \sqrt{2}$. It may be seen from equation (21a) that the radial separation in the focal plane of the images of electron groups with fractional momentum difference ϵ is $4\epsilon r_0$.

The results which we have obtained so far are well known. Before proceeding to the second order, we point out that the first-order aberrations which occur when a_1 is not quite equal to $-\frac{1}{2}$ are easily found from equations (21); we give them, in expressions (25), for later use:

$$(25a) \quad \eta(\pi) \approx -\pi(a_1 + \frac{1}{2})H,$$

$$(25b) \quad \tau(\pi) \approx \pi(a_1 + \frac{1}{2})T.$$

In the remainder of this work it is to be assumed that a_1 is exactly equal to $-\frac{1}{2}$. Also, since we are not interested in higher-order corrections to the dispersion,

we shall keep $\epsilon = 0$ henceforth. On the other hand, since we must deal with sources of finite size, we shall no longer restrict our discussion to orbits originating on the optic circle. The appropriate first-order solution is given by the equations

$$(26a) \quad \eta = H \sin \psi + h \cos \psi,$$

$$(26b) \quad \tau = T \sin \psi + t \cos \psi.$$

As defined in the preceding section, h and t are the initial values of η and τ , while H and T are the initial values of η' and τ' . If $h = t = 0$, then H and T are also the extreme values of η and τ respectively; these extreme values occur for $\psi = \pi/2$. Though h and t are not actually zero, they are sufficiently small that H and T may be considered to be good approximations to the first-order maximum departures from the optic circle. In our later work we shall consider only those orbits which satisfy the conditions

$$-H_0 < H < H_0, \quad -T_0 < T < T_0,$$

and refer to the permitted range of H and T as the aperture. The required selection of orbits could be made, to the first approximation, by a rectangular baffle with an opening of dimensions $2H_0r_0 \times 2T_0r_0$ placed in the plane $\psi = \frac{1}{2}\pi$.

The transmission \mathcal{T} , defined as the percentage of all electrons emitted by the source accepted by the spectrometer, is simply related to the size of the aperture. We define ϕ_r as the angle between the projection of the initial velocity vector on the plane of symmetry and the tangent to the optic circle at the point $\psi = 0$. Similarly, ϕ_z is the angle between this same tangent and the projection of the initial velocity vector on the plane which contains that tangent and a line parallel to the z -axis. It is not difficult to show that

$$(27) \quad \sqrt{2} \tan \phi_r = H \text{ and } \sqrt{2} \tan \phi_z = T.$$

A sufficiently good approximation to the transmission is

$$\mathcal{T} \approx 2(\phi_r)_0 \cdot 2(\phi_z)_0 \cdot (4\pi)^{-1} \times 100\%,$$

$(\phi_r)_0$ and $(\phi_z)_0$ being the maximum values of $|\phi_r|$ and $|\phi_z|$ respectively. Using (27) we find

$$(28) \quad \mathcal{T} \approx H_0 T_0 (2\pi)^{-1} \times 100\%.$$

We are now prepared to obtain the second-order solution. Following Svartholm, we write equations (9) and (10) in the form

$$(29a) \quad \eta'' + \eta = R(\eta, \tau, \eta', \tau', H, T, h, t),$$

$$(29b) \quad \tau'' + \tau = S(\eta, \tau, \eta', \tau', H, T, h, t).$$

The right-hand sides of equations (29) can be obtained as power series in all the parameters indicated; there are no terms of degree lower than the second. We call the equations obtained by discarding third- and higher-order terms the second-order orbital equations. These equations are then approximated by the pair of equations formed by substituting the first-order forms of η and τ (26) in the second-order terms. The simple, linear, inhomogeneous equations thus obtained are easily solved, subject to the initial conditions stated in the

preceding section. For the moment we give only the results for $\psi = \pi$, which we term the aberration; the solutions for general values of ψ are included in the lists of results in the next section.

$$(30a) \quad \eta(\pi) = -h + \frac{1}{3}(1-8a_2)H^2 + (\frac{2}{3}a_2-1)T^2 \\ + \frac{2}{3}(1-2a_2)h^2 + (\frac{1}{3}a_2-1)l^2,$$

$$(30b) \quad \tau(\pi) = -t + 2(\frac{2}{3}a_2-1)HT + \frac{2}{3}a_2th.$$

The relations (30) are precisely equivalent to the formulae obtained by Shull and Dennison (1947) by solution of the time-dependent equations of motion. Svartholm gave the terms in H and T only.

Because the dispersion is in the radial direction, choice of the best value of a_2 must be dictated primarily by the need to minimize the radial aberration. The second- and higher-order terms in h may be ignored, because the presence of the first-order terms in (30a) demands that h be exceedingly small. The limits of the first two terms remaining in $\eta(\pi)$ depend on the size of aperture, that of the last on the height of the source. To maximize the efficiency of the spectrometer we must minimize the aberration caused by each of the three terms. By proper choice of a_2 , namely $a_2 = \frac{1}{3}$, $\frac{2}{3}$, or $\frac{4}{3}$, we can make any one of these three terms zero, but not all three simultaneously. The least significant of the three terms is that proportional to l^2 . For a spectrometer of reasonable size the dimensions of sources available will usually be such that $l \ll 1$. If a source of greater height is to be used, it can be curved in such a way that the second-order aberration in l^2 is cancelled by the first-order aberration in h ; the central line of the source should fall along the curve

$$(31) \quad -h + (\frac{1}{3}a_2-1)l^2 = 0.$$

The cancellation will hold, of course, only on the central line of the source, leaving an aberration proportional to the width of the source.

The relative importance of the two remaining terms of the radial aberration depends upon the shape of the aperture. Ideally one ought to find the shape of aperture that, for fixed resolution, maximizes the transmission. The aperture shape so determined, and the corresponding value of the transmission, would be functions of a_2 and of the desired resolution; the best value of a_2 would be that which gives the largest transmission. Because of the neglect of the higher-order terms, the procedure just outlined is probably not worth the effort required. Instead we shall arbitrarily restrict the problem to that of finding the best aperture of rectangular shape. For simplicity we shall fix the basal line-width, σ , rather than the resolution. Now we may write

$$(32) \quad \sigma = p H_0^2 + q T_0^2$$

where $p = \frac{1}{3} | 8a_2 - 1 |$ and $q = | \frac{2}{3}a_2 - 1 |$. It is not difficult to show that the maximum transmission, under the constraint of constant σ , is attained when

$$(33) \quad H_0^2 = \sigma/2p \text{ and } T_0^2 = \sigma/2q.$$

The axial and radial dimensions are given equal weight in making up the permitted line-width σ ; note that this does not occur for equal radial and axial

dimensions unless $p = q$, which equality implies $a_2 = \frac{1}{4}$. With the optimum rectangular aperture we find

$$(34) \quad \mathcal{T} = \sigma(4\pi)^{-1}(pq)^{-\frac{1}{2}} \times 100\%.$$

The quantity pq is roughly equal to $64/9 a_2^2$ for large values of $|a_2|$; it vanishes at $a_2 = \frac{1}{8}$ and at $a_2 = \frac{3}{8}$; between the roots it reaches a local maximum at $a_2 = \frac{1}{4}$. Thus the best choice of a_2 is either $\frac{1}{8}$ or $\frac{3}{8}$; values of a_2 very much smaller than $\frac{1}{8}$ or very much larger than $\frac{3}{8}$ give much poorer transmission; in the range $\frac{1}{8} < a_2 < \frac{3}{8}$ the worst possible choice is $a_2 = \frac{1}{4}$. This last statement, at first sight, seems to contradict the findings of Rosenblum (1947), who showed that, with a given circular aperture, the smallest basal line-width is obtained for $a_2 = \frac{1}{4}$. The arbitrary restriction to circular apertures is responsible for the paradox. We can see no good reason for making such a restriction, except possibly when an instrument with large higher-order terms is used at high transmission. It is interesting to note that Rosenblum's calculation performed for a square aperture gives a constant line-width for a_2 in the range $\frac{1}{8}$ to $\frac{3}{8}$; outside this range the line-width increases rapidly.

The analysis of the preceding paragraph has shown that the best transmission for given resolution, with a variable rectangular aperture, occurs when a_2 is either $\frac{1}{8}$ or $\frac{3}{8}$. Consider the former case first. A large transmission is obtained because, for $p = 0$, H_0 is permitted to become very large; the limit on H_0 will be set by the third- and higher-order terms, which we have omitted from (32). These terms will limit H_0 to values sufficiently small that expression (28) for the transmission remains applicable. For this choice of a_2 the value of q is $\frac{3}{8}$; the value of T_0 , fixed by σ , is much smaller than that of H_0 . Terms in (32) containing high powers of T_0 or products of T_0^2 with powers of H_0 may be ignored. The dominant terms in σ are the powers of H_0 . Since Maxwell's equations allow us one free parameter for each order used in the description of the magnetic field, we can make the coefficients of the powers of H_0 in the expansion of σ all zero by proper choice of our free parameters. If, in an actual spectrometer, a few of the a_n beyond a_2 were fitted to their optimum values, a much larger value of H_0 could be used. Such an instrument we shall call a wide-aperture spectrometer. The required values of the coefficients a_n , up to $n = 4$ or 5, have been published by several authors: Verster (1950), Pavinski (1954), Saulit (1954), and Huster *et al.* (1955).

When we look at the other choice of a_2 , viz. $\frac{3}{8}$, we see that the roles of H_0 and T_0 are reversed. Here the residual second-order aberration is $\frac{3}{8}H_0^2$; it is now H_0 that must be kept small. The dominant terms in the expansion of T are now those proportional to $T_0^2H_0$, T_0^4 , $T_0^4H_0$, T_0^6 , Again there is one large term for each of the a_n . We can choose the a_n so that the expansion coefficients can be made zero; a large value of T_0 may then be employed. Such an instrument we shall term a high-aperture spectrometer. Calculation of the required optimum values of the a_n , up to $n = 6$, was the main purpose of the work which we are now reporting; these coefficients are supplied in the following section. Their calculation is much more difficult than that of the corresponding coefficients for the wide-aperture type, because orbits not confined to the plane of symmetry must now be considered.

Though it is certain that either the wide-aperture or the high-aperture instrument, i.e. either $a_2 = \frac{1}{3}$ or $a_2 = \frac{2}{3}$, can be superior to one built with any other choice of a_2 , it does not seem possible to ascribe an overwhelming superiority to one over the other. In the matter of transmission at given resolution the two spectrometers should be almost equally satisfactory, if the same number of coefficients a_n is properly fitted for each. The odd-order dominant aberrations of the wide-aperture and of the high-aperture types of spectrometer are proportional to H_0^{2n+1} and to $H_0 T_0^{2n}$ respectively; the latter has a slight advantage because it contains the smaller factor H_0 . Nevertheless, superiority in transmission cannot be claimed for either type without reference to the method of providing the required magnetic field. For a given method of generating the magnetic field the highest transmission will be obtained with the spectrometer for which the largest number of a_n can be fitted to their optimum values.

There are, however, three minor advantages in favor of the high-aperture type:

(1) By good luck the choice $a_2 = \frac{2}{3}$ also gives second-order axial focusing, i.e. the coefficient of HT in (30b) vanishes; for the appropriate value of a_3 the third-order terms are small. For the choice $a_2 = \frac{1}{3}$, on the other hand, the second-order axial aberration is $-\frac{1}{3}HT$. The better axial focusing for the former case, though probably not important at apertures corresponding to 0.01% resolution, might be useful at apertures corresponding to 1% resolution. For example, for the high-aperture case with $H = 0.25$, $T = 0.4$, we find that $\tau(\pi) = 0.0088$; for the wide-aperture case with $H = 0.4$, $T = 0.25$, we find that $\tau(\pi) = 0.13$.

(2) For $a_2 = \frac{2}{3}$ the coefficient of t^2 in $\eta(\pi)$ is $-\frac{1}{2}$; for $a_2 = \frac{1}{3}$ this coefficient is $-\frac{5}{6}$. Hence linear sources 30% higher may be used for the former case with the same resolution.

(3) The required magnetic field for the high-aperture type has a shape very near to that of the function $1/\sqrt{r}$. This means that the spectrometer will have good focusing properties for r_0 's chosen from the whole fitted range of r , and therefore that it will focus electron groups of considerably different momenta simultaneously. This property is useful in that it enables one, with photographic detection, to examine an appreciable part of the spectrum in one operation.

4. HIGHER-ORDER CALCULATIONS

Having decided to use $a_1 = -\frac{1}{2}$ and $a_2 = \frac{2}{3}$, we next proceed to work out the optimum values of a_n for $n > 2$. The first step is to solve equations (29) to the desired order of approximation by a generalization of the procedure by which we found the second-order solution. Because the effect of the finite size of the source can be estimated with sufficient accuracy in the second-order approximation, we now put $h = t = 0$. The approximate solution of order $(n+1)$ is obtained by substituting that of order n in the right-hand sides of the equation (29). The simple, linear, inhomogeneous differential equations

thus obtained may be solved in a straightforward manner; the amount of labor required mounts rapidly with the order. In this fashion we generate approximate expressions for η and τ which are polynomials in H and T , the coefficients being functions of ψ . Though it would be difficult to prove that the approximate method is mathematically legitimate, it is true, as Svartholm points out, that the form of the solution obtained is that which is of interest practically; the excellent agreement of the analytical formulae with the results of the numerical integrations, to be described later, shows that the procedure for obtaining the approximate solutions is indeed a very good one.

We write

$$(35a) \quad \eta = \sum_{mn} F_{mn}(\psi) H^m T^n,$$

$$(35b) \quad \tau = \sum_{mn} G_{mn}(\psi) H^m T^n.$$

Because of the symmetry of the magnetic field, only even powers of T occur in η and only odd powers in τ . All terms in the approximate solutions (35) as far as the fourth order have been obtained; because of their possible usefulness in baffle calculations, we give these terms in full.

$$F_{10} = \sin \psi \quad F_{02} = -\frac{1}{4} \sin^2 \psi \quad F_{20} = \frac{5}{12} \sin^2 \psi + \frac{1}{3} (\cos \psi - 1)$$

$$F_{12} = \left(\frac{1}{2} c_{22} - \frac{21}{64} \right) \sin^3 \psi + \left(\frac{3}{2} c_{22} - \frac{7}{64} \right) (\psi \cos \psi - \sin \psi)$$

$$F_{30} = \left(c_{04} - \frac{1}{192} \right) \sin^3 \psi + \left(3c_{04} - \frac{11}{192} \right) (\psi \cos \psi - \sin \psi) \\ + \frac{5}{18} \sin \psi (\cos \psi - 1)$$

$$F_{04} = \left(\frac{16}{15} c_{41} - \frac{8}{15} c_{22} + \frac{32}{15} c_{40} + \frac{11}{240} \right) (\cos \psi - 1) \\ + \left(\frac{8}{15} c_{41} - \frac{4}{15} c_{22} + \frac{77}{30} c_{40} + \frac{209}{1920} \right) \sin^2 \psi \\ + \left(\frac{2}{15} c_{41} - \frac{1}{15} c_{22} - \frac{7}{30} c_{40} + \frac{131}{1920} \right) \sin^4 \psi \\ - \left(\frac{3}{4} c_{40} + \frac{7}{256} \right) \psi \sin 2\psi$$

$$F_{22} = \left(\frac{16}{5} (c_{23} - c_{04} + c_{22}) - \frac{19}{120} \right) (\cos \psi - 1) \\ + \left(\frac{8}{5} (c_{23} - c_{04}) + \frac{11}{10} c_{22} - \frac{61}{960} \right) \sin^2 \psi \\ + \left(\frac{2}{5} (c_{23} - c_{04}) + \frac{61}{90} c_{22} - \frac{59}{960} \right) \sin^4 \psi \\ + \left(\frac{1}{6} c_{22} - \frac{7}{64} \right) \sin^2 \psi \cos \psi + \left(\frac{13}{192} - \frac{1}{6} c_{22} \right) \psi \sin \psi$$

$$\begin{aligned}
& + \left(\frac{1}{4} c_{22} - \frac{7}{384} \right) \psi \sin 2\psi \\
F_{40} = & \left(\frac{16}{3} c_{05} - \frac{37}{432} \right) (\cos \psi - 1) + \left(\frac{8}{3} c_{05} - \frac{5}{2} c_{04} - \frac{355}{3456} \right) \sin^2 \psi \\
& + \left(\frac{2}{3} c_{05} + \frac{3}{2} c_{04} - \frac{193}{3456} \right) \sin^4 \psi + \left(c_{04} - \frac{1}{192} \right) \sin^2 \psi \cos \psi \\
& + \left(\frac{11}{576} - c_{04} \right) \psi \sin \psi + \left(\frac{5}{4} c_{04} - \frac{55}{2304} \right) \psi \sin 2\psi \\
G_{01} = & \sin \psi \quad G_{11} = \frac{1}{2} \sin^2 \psi \\
G_{03} = & \left(c_{40} - \frac{11}{64} \right) \sin^3 \psi + \left(3 c_{40} + \frac{7}{64} \right) (\psi \cos \psi - \sin \psi) \\
G_{21} = & \left(\frac{1}{2} c_{22} + \frac{1}{192} \right) \sin^3 \psi \\
& + \left(\frac{3}{2} c_{22} - \frac{7}{64} \right) (\psi \cos \psi - \sin \psi) + \frac{1}{6} \sin \psi (\cos \psi - 1) \\
G_{13} = & \left(\frac{128}{15} c_{40} + \frac{64}{15} c_{41} - \frac{32}{15} c_{22} + \frac{11}{60} \right) (\cos \psi - 1) \\
& + \left(\frac{83}{30} c_{40} + \frac{32}{15} c_{41} - \frac{109}{60} c_{22} - \frac{1}{30} \right) \sin^2 \psi \\
& + \left(\frac{47}{30} c_{40} + \frac{8}{15} c_{41} - \frac{1}{60} c_{22} - \frac{17}{240} \right) \sin^4 \psi \\
& + \left(\frac{3}{4} c_{40} + \frac{3}{8} c_{22} \right) \psi \sin 2\psi \\
G_{31} = & \left(\frac{32}{15} (c_{22} + c_{23} - c_{04}) + \frac{1}{180} \right) (\cos \psi - 1) \\
& + \left(\frac{16}{15} c_{23} + \frac{19}{60} c_{22} - \frac{77}{30} c_{04} - \frac{1}{90} \right) \sin^2 \psi \\
& + \left(\frac{7}{30} c_{04} + \frac{133}{180} c_{22} + \frac{4}{15} c_{23} - \frac{67}{720} \right) \sin^4 \psi \\
& + \left(\frac{1}{3} c_{22} + \frac{1}{288} \right) \sin^2 \psi \cos \psi - \left(\frac{1}{3} c_{22} + \frac{1}{32} \right) \psi \sin \psi \\
& + \left(\frac{3}{4} c_{04} + \frac{3}{8} c_{22} - \frac{1}{24} \right) \psi \sin 2\psi
\end{aligned}$$

In addition, we give the values at $\psi = \pi$ of those fifth- and sixth-order terms which affect the focusing significantly.

$$\begin{aligned}
F_{14}(\pi) = & \pi \left(-\frac{5}{4} c_{42} - \frac{121}{48} c_{41} - \frac{1237}{384} c_{40} - \frac{15}{32} c_{04} + \frac{15}{16} c_{23} \right. \\
& \left. + \frac{145}{96} c_{22} + \frac{35}{16} c_{22}^2 + \frac{35}{4} c_{22} c_{40} - \frac{5513}{49,152} \right)
\end{aligned}$$

$$\begin{aligned}
 F_{06}(\pi) = & \frac{2176}{525} c_{41} - \frac{289}{175} c_{22} + \frac{3838}{525} c_{40} - \frac{192}{35} c_{60} - \frac{64}{35} c_{61} \\
 & + \frac{4}{35} c_{04} - \frac{12}{35} c_{23} + \frac{32}{35} c_{42} + \frac{8192}{175} c_{40}^2 + \frac{512}{175} c_{22} c_{41} \\
 & - \frac{256}{175} c_{22}^2 - \frac{1024}{175} c_{22} c_{40} + \frac{4096}{175} c_{40} c_{41} + \frac{74}{525} \\
 & - \frac{\pi^2}{4} \left(3 c_{40} + \frac{7}{64} \right)^2 \\
 G_{06}(\pi) = & \pi \left(\frac{15}{16} c_{41} - \frac{15}{64} c_{22} + \frac{357}{128} c_{40} + \frac{105}{4} c_{40}^2 - \frac{15}{4} c_{60} + \frac{905}{16,384} \right)
 \end{aligned}$$

The coefficients c_{mn} upon which the functions $F_{mn}(\psi)$ and $G_{mn}(\psi)$ listed depend can, as is shown in Section 2, all be expressed in terms of the coefficients a_n . Though putting a_n equal to its optimum value before proceeding to work out terms of order $(n+1)$ would have lightened the algebraic labor enormously, we did not do so because we wished to calculate orbits in fields other than the optimum, principally that of Stoker *et al.* (1954) and that which varies like $1/\sqrt{r}$.

The possession of formulae for $F_{1n}(\psi)$ and $F_{0n}(\psi)$ enables us to determine the optimum values of a_n for the high-aperture spectrometer. From the equations

$$F_{1n}(\pi) = 0 \text{ for } n = 2 \text{ and } 4,$$

$$F_{0n}(\pi) = 0 \text{ for } n = 4 \text{ and } 6,$$

we have calculated the required values of a_3 , a_4 , a_5 , and a_6 . These values are listed in the second column of Table I. In the third column of this table we

TABLE I
VALUES OF MAGNETIC FIELD EXPANSION COEFFICIENTS

n	Optimum	$1/\sqrt{r}$	Δa_n
0	1	1	—
1	$-\frac{1}{2}$	$-\frac{1}{2}$	-0.0013
2	$\frac{3}{8}$	$\frac{3}{8}$	0.0004
3	$-\frac{43}{144} = -0.2986 \dots$	$-\frac{5}{16} = -0.3125$	0.0063
4	$\frac{553}{2304} = 0.2400 \dots$	$\frac{35}{128} = 0.2734 \dots$	-0.0058
5	$-\frac{69,709}{345,600} = -0.2017 \dots$	$-\frac{63}{256} = -0.2461 \dots$	-0.050
6	$\frac{60,299}{345,600} + \frac{35\pi^2}{147,456} = 0.1768 \dots$	$\frac{231}{1024} = 0.2256 \dots$	0.075

give the expansion coefficients for a field which varies like $1/\sqrt{r}$. The similarity of the two sets of numbers is striking, and is probably responsible for the good focusing properties of instruments built with a field varying like $1/\sqrt{r}$. The significance of the numbers in the fourth column will be explained in the next section.

By substituting the values of the c_{mn} derived from the optimum values of the a_n in the expansion for $F_{mn}(\pi)$ and $G_{mn}(\pi)$ we obtain formulae for the aberrations, viz.

$$(36a) \quad \eta(\pi) = -\frac{2H^2}{3} + \frac{8}{45}H^2T^2 + \frac{8}{27}H^4,$$

$$(36b) \quad \tau(\pi) = -\frac{\pi}{24}T^3 - \frac{14}{135}H^2T + 0.019635T^6.$$

The relations (36a) and (36b) are complete as far as the fourth order, and contain the important terms, for the high-aperture spectrometer, as far as the sixth and fifth orders respectively. The coefficients of H^3 in the former and HT , H^2T , and HT^3 in the latter vanish accidentally.

Because the values of a_3 and a_4 which we obtained did not agree with those published by Stoker *et al.* (1954), namely $-5/24$ and $37/192$, we thought it advisable to check our solutions by some other means. The unexpected occurrence of π^2 in a_6 , which could not be removed by persistent recalculation, also excited suspicion that something might be wrong. Accordingly, we decided to compare the aberrations calculated analytically with aberrations obtained by a direct numerical integration of equations (9) and (10). We are much indebted to Mr. G. A. Chisnall* for carrying out these numerical integrations on FERUT, the Ferranti Computer at the Computation Centre of the University of Toronto. The method used in the integration was that devised by Adams and Bashforth. The results obtained by numerical integration with the optimum field appear in the columns under the symbol N in Table II.

TABLE II
COMPARISON OF NUMERICAL AND ANALYTICAL CALCULATIONS OF
THE ABERRATION IN THE OPTIMUM FIELD

T	H	$-\eta(\pi) \times 10^3$		$-\tau(\pi) \times 10^3$	
		N	A	N	A
0	+0.1	6.637	6.637	0	0
	-0.1	6.637	6.637	0	0
0.1	+0.1	6.622	6.619	0.140	0.141
	0	0.000	0	0.131	0.131
	-0.1	6.618	6.619	0.119	0.121
0.2	+0.025	0.412	0.413	1.040	1.041
	0	0.000	0	1.041	1.041
	-0.025	0.411	0.413	1.040	1.041
0.3	+0.025	0.408	0.407	3.477	3.486
	0	-0.003	0	3.481	3.486
	-0.025	0.401	0.407	3.481	3.486

*Now at the Department of Astronomy, University of Manchester, Manchester, England.

Aberrations calculated from the formulae (36) appear under the symbol A . The agreement is excellent, the small discrepancy which appears for larger values of T being of a size easily explained by the higher-order terms neglected in (36). Similar comparisons have been made with the same sort of agreement for the field of Stoker *et al.*, and for that which varies like $1/\sqrt{r}$. We believe that we are justified, therefore, in claiming that our analytical solutions and our set of optimum values for the coefficients a_n are correct and that those of Stoker *et al.* are incorrect.

5. THE IMAGE OF A POINT SOURCE

The expansions of the aberrations (36) in powers of the aperture dimensions are more likely to give a good description of the image when the aperture used is small, as it is at high resolution. We shall examine the image at an aperture corresponding to a resolution of 0.01%. First some suitable value of H_0 must be assumed. Put the residual second-order aberration, $\frac{2}{3}H_0^2$, equal to the separation in $\eta(\pi)$ of two electron groups differing by 0.01% in momentum. In the absence of other aberrations and of finite source width, this procedure corresponds to a complete resolution of the two lines. From our knowledge of the dispersion of the instrument we can say that the separation in $\eta(\pi)$ of the two groups is 4×10^{-4} ; hence $H_0 = 0.025$. In Fig. 1 (a), (b), and (c) we show the images of a point source on the optic circle made by our optimum field, by the field of Stoker *et al.*, and by the field of the form $1/\sqrt{r}$. Lines labelled $H = \pm 0.025$ or $H = 0$ are the loci of the traces on the focal plane of orbits with the indicated values of H . Similarly the lines labelled with a value of T are the loci of the traces of orbits having that value of T . The quality of the fit to the optimum field which we have been able to obtain with a system of pairs of air-cored coils suggests that values of T up to $T_0 = 0.3$ are not unreasonable. Inspection shows that the image made by the Stoker field is much inferior to that made by our optimum field. The image made by the $1/\sqrt{r}$ field, though appreciably wider than that of the optimum field, is still very good.

The transmission attainable at a resolution of 0.01% depends on the maximum allowable value of T_0 . Fig. 1(a) shows that no appreciable broadening has occurred, for the optimum field, for values of T as large as 0.3. Though FERUT calculations indicate that the broadening of the image is negligible for T as large as 0.5, in any real instrument the effect of the higher-order, uncanceled aberrations would probably be very serious at such large values of T . We shall content ourselves with pointing out that for $T_0 = 0.3$ the transmission is about 0.12%.

At a resolution of 1% the criterion for finding H_0 which we used in the last paragraph gives $H_0 = 0.25$. If values of T_0 as large as 0.4 can be used, then a transmission of 1.5% should be achieved.

The radial defocusing occurring when a_n is not quite equal to its optimum value can be calculated from the formulae which we have given. For the first and second orders use (25a) and (30a) respectively; for higher orders use the formulae for $F_{1m}(\pi)$ and $F_{0m}(\pi)$. To give some idea of the closeness of fit

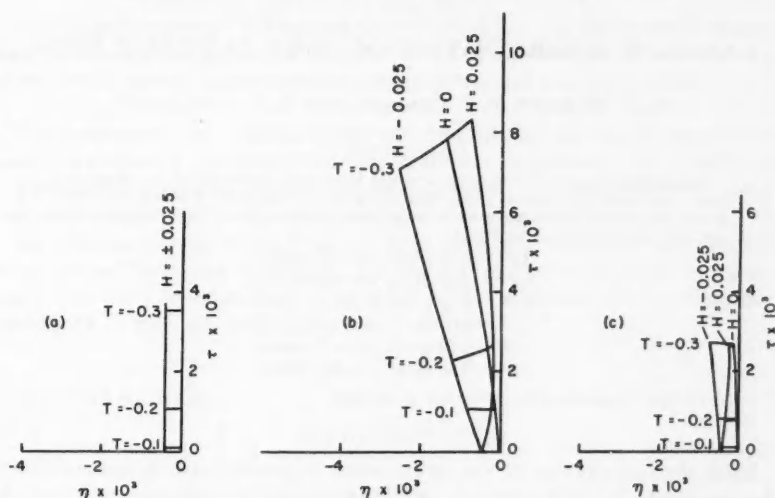


FIG. 1. Image of a point source on the optic circle; (a) refers to the optimum field, (b) to that of Stoker *et al.*, and (c) to that of the form $1/\sqrt{r}$.

required we give the numbers in the last column of Table I. The quantity Δa_n is defined as the increment in a_n producing an increment in $\eta(\pi)$ of 10^{-4} at $H = 0.025$, $T = 0.3$; all earlier a_n are assumed to have their optimum values, and the effect of the increment in a_n is calculated in the n th order only. Under these conditions the relation between $\eta(\pi)$ and a_n is approximately linear.

ACKNOWLEDGMENTS

We are greatly indebted to Mr. G. A. Chisnall for devising the FERUT program for integrating the orbital equation. Acknowledgment is due to Mrs. A. R. Jones and to Miss N. A. O. Stewart for assistance in curve drawing and in some of the algebraic manipulation.

REFERENCES

- HUSTER, E., LEHR, G., and WALCHER, W. 1955. *Z. Naturforsch.* **10a**, 83.
 MOUSSA, A. and BELLICARD, J.-B. 1954. *J. phys. radium*, **15**, 85A.
 PAVINSKI, P. P. 1954. *Izvest. Akad. Nauk S.S.S.R. Ser. Phys.* **18**, 175.
 ROSENBLUM, E. S. 1947. *Phys. Rev.* **72**, 731.
 SAULIT, V. R. 1954. *Izvest. Akad. Nauk S.S.S.R. Ser. Phys.* **18**, 227.
 SHULL, F. B. and DENNISON, D. M. 1947. *Phys. Rev.* **71**, 681; **72**, 256.
 SIEGBAHN, K. 1955. *Beta- and gamma-ray spectroscopy* (North-Holland Pub. Co., Amsterdam).
 SIEGBAHN, K. and EDVARSON, K. 1956. *Nuclear Phys.* **1**, 137.
 STOKER, P. H., ONG PING HOK, DE HAAN, E. F., and SIZOO, G. J. 1954. *Physica*, **20**, 337.
 SVARTHOLM, N. 1946. *Arkiv Mat. Astron. Fysik*, **33A**, No. 24.
 SVARTHOLM, N. and SIEGBAHN, K. 1946. *Arkiv Mat. Astron. Fysik*, **33A**, No. 21.
 VERSTER, N. F. 1950. *Physica*, **16**, 815.

HALF-LIFE DETERMINATION OF SOME RADIONUCLIDES¹

W. F. MERRITT, P. J. CAMPION, AND R. C. HAWKINGS²

ABSTRACT

The half-lives of the following nuclides have been determined by absolute counting techniques using a 4π beta proportional counter. The period over which the observations were made is indicated in brackets. The errors quoted are the statistical counting errors.

Na ²²	2.58 ± 0.03 years (2 years),
Ru ¹⁰⁶	1.02 ± 0.01 years (5 years),
Ce ¹³⁴	2.19 ± 0.02 years (5 years),
Ce ¹⁴⁴	285 ± 2 days (4 years),
Pm ¹⁴⁷	2.64 ± 0.02 years (4 years),
Tl ²⁰⁴	3.56 ± 0.05 years (4 years).

A review of previous determinations is included.

1. INTRODUCTION

Since the introduction of the proportional β counter with 4π geometry to this laboratory in 1950, accurate determinations of the disintegration rate of solutions of various radioisotopes have been made. Several of these nuclides have half-lives of the order of 1–5 years and a redetermination of the disintegration rate of the solutions provides a direct method of measuring their half-lives.

2. METHOD

The counting techniques used have been fully described elsewhere (Hawkings *et al.* 1951). In most cases, the original sources were available for counting. Otherwise, new sources were made from the solutions which had been stored in pyrex bottles with greased glass stoppers. These were deposited on the same type of source mount used in the previous determination, usually a laminated zapon-formvar film of $\approx 100 \mu\text{g./cm.}^2$ superficial density, with a conducting layer of gold vacuum distilled on to both sides. The same counters were used in both series of observations.

The following checks on the counting system were made at frequent intervals during the determinations:

(1) Reference sources of Sr⁹⁰ and of Ra D + E were counted at regular intervals to ensure that the system remained stable.

(2) The resolving time of the system was measured several times during the course of the observations. This was done by observing the apparent counting rate of a high activity (35,000 c./s.) Sr⁹⁰ source. The true counting rate of this source was previously determined in a counting system whose dead time had been measured directly by observing the decay of 24.99 minute I¹³¹.

¹Manuscript received August 17, 1956.

Contribution from the Nuclear Physics I Branch, Atomic Energy of Canada Limited, Chalk River, Ontario. Issued as A.E.C.L. No. 371.

²Present address: Development Chemistry Branch, Atomic Energy of Canada Limited, Chalk River, Ontario.

(3) Where necessary, the sources were counted in a low background laboratory remote from large sources of radioactivity. This was done for sources with a low counting rate where the background correction was appreciable.

To demonstrate the validity of the counting techniques, the disintegration rate of a sample of Cl^{36} which had been used in a measurement of its half-life in 1953 was redetermined (Bartholomew *et al.* 1955). This agreed with previous results to within 0.6%, well within the quoted standard error.

In addition, sources of Ra D + E (Pb^{210}) have been observed over a period of $5\frac{1}{2}$ years. These give a value for the half-life of 22.4 ± 0.4 years, in agreement with the values quoted by Curie *et al.* (1931) of 22 years, but in disagreement with Tobailem's (1955) value of 19.40 years.

3. CALCULATIONS

From the equation

$$(1) \quad N = N_0 e^{-\lambda T}$$

it follows that

$$(2) \quad T_{\frac{1}{2}} = 0.69315 T / \ln(N_0/N)$$

where N_0 and N are the disintegration rates at the beginning and end of the period of observation. $T_{\frac{1}{2}}$ is the half-life and λ the disintegration constant. In considering the errors involved in the determinations, it can be shown that by differentiating equation (2), the error in the half-life is related to the error in the counting rates by

$$(3) \quad \frac{\Delta T_{\frac{1}{2}}}{T_{\frac{1}{2}}} = \frac{-T_{\frac{1}{2}}}{0.69315 T} \frac{\Delta N_0/N}{N_0/N}.$$

Fig. 1 shows the fractional error in $T_{\frac{1}{2}}$ plotted against the period of observation measured in half-lives for a 1% error in N_0/N . This curve shows that the period of observation should be at least equal to one half-life and preferably more if reasonable accuracy is to be obtained.

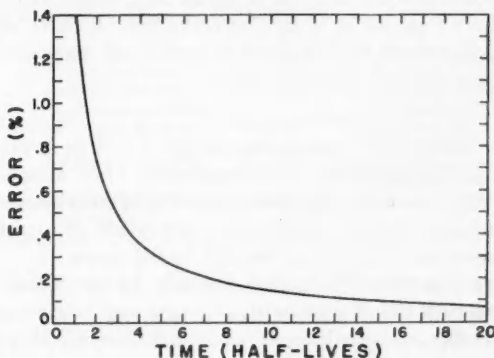


FIG. 1. A plot of equation (3) showing the fractional error in half-life as a function of the period of observation assuming an error of 1% in N_0/N .

For those nuclides where the original sources were available, the errors quoted are the standard deviations from the mean. In the case of those samples for which new sources had to be prepared from the original solutions, the errors quoted are calculated from the above equation using an estimate for the maximum error in N_0/N . This estimate includes statistical errors and the spread in disintegration rate values as observed from several sources.

4. MEASUREMENTS

Na^{22}

Laslett (1949) observed a sample of Na^{22} over a 3-year period with a Lauritsen electroscope and reported a half-life of 2.60 years. By irradiating fluorspar with polonium α -particles, Saha (1939-41) prepared a sample of Na^{22} which he observed with a point counter. From his measurements he estimated a half-life of 2.8 years.

We received a sample of Na^{22} from the National Bureau of Standards, Washington, in 1954. Four sources prepared from this solution were counted immediately and recounted after a period of 2 years. A half-life of 2.59 ± 0.02 years was obtained.

At about the same time a shipment of Na^{22} was received from the Atomic Energy Research Establishment, Harwell. Because this sample had a high solids content, it was purified by elution from a 1 meter long column of Colloidal Dowex 50 ion exchange resin, following the method of Beukenkamp and Rieman (1950), and its disintegration rate determined. A redetermination of this rate yielded a half-life value of 2.55 ± 0.05 years, in good agreement with the N.B.S. sample.

Because the original sources were available for the N.B.S. sample and because the A.E.R.E. sample was of high solids content we quote a weighted average of 2.58 ± 0.03 years.

Ru^{106}

Glendenin and Steinberg (1951) reported a half-life of 1.0 year for Ru^{106} .

In 1951 we counted three sources prepared from a solution of Ru^{106} which had been carefully purified by a distillation technique. A redetermination of the disintegration rate of these sources after 5 years showed a decay corresponding to a half-life of 1.02 ± 0.01 years.

Cs^{134}

Kalbfell and Cooley (1940) prepared a sample of Cs^{134} by bombarding cesium with cyclotron-produced neutrons and deuterons. They obtained a value for the half-life of 20 ± 1 months. Glendenin (1951) irradiated cesium with thermal neutrons in a nuclear reactor, followed its decay for 13 months using G-M counters, and reported a half-life value of 2.3 ± 0.3 years.

We irradiated "Specpure"* cesium chloride in the Chalk River NRX Reactor and removed the chlorine with an anion exchange resin. Five sources were recounted after a 5 year interval and a half-life of 2.19 ± 0.02 years was obtained.

*Trademark of Johnson and Matthey Company Limited, London.

Ce¹⁴⁴

In 1944 F. Joliot reported a value of 290 days. Schuman and Camilli (1951) followed a sample of aged fission product Ce^{144} for two half-lives in a flow type β proportional counter and reported a half-life of 285 ± 3 days. Burgus *et al.* (1951) followed a sample for 660 days using G-M counters and found a half-life of 275 days.

Sources were prepared from a solution of aged fission product Ce^{144} and counted in 1952. Four years later the solution was restandardized by the preparation and counting of fresh sources. A decay corresponding to a half-life of 285 ± 2 days was obtained.

Pm¹⁴⁷

Inghram *et al.* (1950) estimated the half-life of Pm^{147} from the yield curve of the fission products as 2.26 years. Schuman and Camilli (1951) followed a source for 1 year and reported a half-life of 2.6 ± 0.2 years. Melaika *et al.* (1955) measured the half-life of Pm^{147} from the growth of Sm^{147} with respect to Sm^{149} using a mass spectrometer. Observations over a period of 5.6 years gave a value of 2.52 ± 0.08 years.

In 1952 we received a solution of Pm^{147} which had been purified by ion exchange techniques. Five sources prepared from this solution were counted immediately, and recounted after a period of 4 years. A half-life of 2.64 ± 0.02 years was obtained.

Tl²⁰⁴

The wide spread in reported values for the half-life of Tl^{204} is shown in Table I.

TABLE I

Date	Workers	Apparatus	Period of observation	Source of material	Half-life
1941	Fajans and Voight	Bubble type G-M counters, Lauritsen electroscope	300 days	Cyclotron irradiation of thallium	3.5 ± 0.5 years
1953	Locket and Thomas	TQQ β electroscope	8 months		2.71 ± 0.05 years
1953	Reynolds and Brooksbank	G-M and proportional counters	15 months	Pile irradiation of thallium	2.7 years
1953	Harbottle	Flow type β proportional counter	2.9 years	Oak Ridge thallium pile produced	4.0 ± 0.1 years
1954	Horrocks and Voight	Lauritsen electro-scope	3 years	Oak Ridge thallium pile produced	4.1 ± 0.1 years
1955	Cheng <i>et al.</i>	Ionization chamber	10 years	Cyclotron irradiation of thallium	2.50 ± 0.03 years
1955	Tobailem and Robert	Differential ionization chamber	45 days	U.S.A.E.C. Tl^{204}	4.26 ± 0.06 years

We have measured the decay of two solutions of Tl^{204} , one for $4\frac{1}{2}$ years, the other for 3 years. The first solution was prepared from thallium metal which had been irradiated in the NRX Reactor in 1949. Subsequent spectroscopic examination of the metal has shown no significant impurity. This sample was dissolved in strong nitric acid and counted in 1951. The other solution was

produced by neutron irradiation of "Specpure" thallium carbonate in the NRX Reactor in 1953 followed by dissolution in strong nitric acid. The gamma-ray spectrum for this sample was examined with a 5 in. \times 4 in. NaI(Tl) crystal for possible impurities. In the range 32 kev. to 1.7 Mev. only the characteristic X-ray of mercury was observed.

Recently these solutions have been restandardized by the preparation and counting of fresh sources. A decay of the older and younger solutions corresponding to half-lives of 3.54 ± 0.05 years and 3.59 ± 0.05 years respectively was obtained. We quote a mean value of 3.56 ± 0.05 years.

REFERENCES

- BARTHOLOMEW, R. M., BOYD, A. E., BROWN, F., HAWKINGS, R. C., LOUNSBURY, M., and MERRITT, W. F. 1955. *Can. J. Phys.* **33**, 43.
 BEUKENKAMP, J. and RIEMAN, W., III. 1950. *Anal. Chem.* **22**, 582.
 BURGUS, W. H., WINSBERG, L., SEILER, J. A., and RUBINSON, W. 1951. *National Nuclear Energy Series, Div. IV, Vol. 9* (McGraw-Hill Book Company, Inc., New York), p. 1195.
 CHENG, L. T., RIDOLFO, V. C., POOL, M. L., and KUNDU, D. N. 1955. *Phys. Rev.* **98**, 231A.
 CURIE, M., DEBIERNE, A., EVE, A. S., GEIGER, H., HAHN, O., LIND, S. C., MEYER, St., RUTHERFORD, E., and SCHWEIDLER, E. 1931. *Revs. Mod. Phys.* **3**, 427.
 FAJANS, K. and VOIGHT, A. F. 1941. *Phys. Rev.* **60**, 619.
 GLENDENIN, L. E. 1951. *National Nuclear Energy Series, Div. IV, Vol. 9* (McGraw-Hill Book Company, Inc., New York), p. 1931.
 GLENDENIN, L. E. and STEINBERG, E. P. 1951. *National Nuclear Energy Series, Div. IV, Vol. 9* (McGraw-Hill Book Company, Inc., New York), p. 793.
 HARBOTTLE, G. 1953. *Phys. Rev.* **91**, 1234.
 HAWKINGS, R. C., MERRITT, W. F., and CRAVEN, J. H. 1951. *Symposium on Recent Developments and Techniques in the Maintenance of Standards, Natl. Phys. Lab., England (May). Reissued as Atomic Energy of Canada Limited Report, A.E.C.L. No. 43* (1952).
 HORROCKS, D. L. and VOIGHT, A. F. 1954. *Phys. Rev.* **95**, 1205.
 INGRAM, M. G., HAYDEN, R. J., and HESS, D. C., Jr. 1950. *Phys. Rev.* **79**, 271.
 JOLIOT, F. 1944. *Compt. rend.* **218**, 733.
 KALBFELL, D. C. and COOLEY, R. A. 1940. *Phys. Rev.* **58**, 91.
 LASLETT, L. J. 1949. *Phys. Rev.* **76**, 858.
 LOCKET, E. E. and THOMAS, R. H. 1953. *Nucleonics*, **11**(3), 14.
 MELAIKA, E. A., PARKER, M. J., PETRUSKA, J. A., and TOMLINSON, R. H. 1955. *Can. J. Chem.* **33**, 830.
 REYNOLDS, S. A. and BROOKSBANK, W. A., Jr. 1953. *Nucleonics*, **11**(11), 46.
 SAHA, N. K. 1939-41. *Trans. Bose Research Inst. Calcutta*, **14**, 57; *Chem. Abstr.* **42**, 450i (1948).
 SCHUMAN, R. P. and CAMILLI, A. 1951. *Phys. Rev.* **84**, 158.
 TOBAILEM, J. 1955. *J. phys. radium*, **16**, 235.
 TOBAILEM, J. and ROBERT, J. 1955. *J. phys. radium*, **16**, 340.

SPALLATION YIELDS FROM HIGH ENERGY PROTON BOMBARDMENT OF HEAVY ELEMENTS¹

J. D. JACKSON

ABSTRACT

The Monte Carlo calculations of McManus and Sharp (unpublished) for the prompt nuclear processes occurring upon bombardment of heavy elements by 400 Mev. protons are combined with a description of the subsequent neutron evaporation to determine spallation cross sections for comparison with experiment. The model employed is a schematic one which suppresses the detailed characteristics of individual nuclei, but gives the over-all behavior to be expected. Many-particle and collective effects such as alpha particle emission and fission are ignored. The computed cross sections are presented in a variety of different graphical forms which illustrate quantitatively the qualitative picture of high energy reactions first given by Serber (1947). The calculations are in general agreement with existing data when fission is not an important effect, but the agreement does not imply a very stringent test of the various features of the model.

1. INTRODUCTION

The qualitative features of nuclear reactions at high energies (over 100 Mev.) were first described by Serber (1947) nearly ten years ago. Since that time a large amount of experimental work has been done on high energy spallation and fission yields for various types and energies of bombarding particle, and for targets of different mass numbers. Essentially all the work has been radiochemical in nature. It will suffice to refer to a few of the more recent papers from which earlier references can be obtained (Bennett 1954; Nervik and Seaborg 1955; Lindner and Osborne 1956). The experimental data confirm in broad outline the behavior predicted by Serber. At any given bombarding energy, a large number of different reactions proceed with comparable yield, while individual yields vary relatively slowly with energy. For all but the heaviest elements, the most likely reactions are those which give rise to product nuclei lying less than 10 or so mass units below the target mass, although nuclei 20 or more mass units below the target are formed in significant amounts. In the heavy element region, fission competes with spallation, giving a broad mass yield distribution centered somewhat below half of the target mass. The fission contribution increases rapidly as a function of atomic number—for tantalum bombarded by 340-Mev. protons fission occurs less than 1% of the time (Nervik and Seaborg 1955), while for uranium it occurs in more than 70% of the interactions (Jungerman and Steiner 1956).

Serber described the impact of a high energy nucleon or group of nucleons with a target nucleus as a two-stage process. The first process is a series of quasi-free, two-body collisions between the incident particle and the nucleons within the nucleus in which, on the average, relatively small amounts (~30 Mev.) of energy are transferred. Commonly the incident particle either passes through the nucleus without any interaction, or makes a few collisions, knocking some of the nucleons out of the nucleus and perhaps emerging

¹Manuscript received August 30, 1956.

Contribution from the Radiation Laboratory, McGill University, Montreal, Quebec.

itself. In this way a few prompt particles, carrying away varying amounts of kinetic energy, are emitted, leaving the residual nucleus with a wide range of different excitations. The second stage of the reaction is the dissipation of this excitation energy by the emission of further particles (evaporation particles) in the manner well known at low energies. These two steps give rise to the general behavior of the cross sections outlined above.

A number of theoretical calculations have been made on different aspects of the problem of high energy reactions. Horning and Baumhoff (1949) discussed stars in photographic emulsions induced by 190 Mev. deuterons, using an analytic approach. Goldberger (1948) was the first to use the so-called Monte Carlo method to describe the prompt processes occurring upon collision of a high energy nucleon with a nucleus. More elaborate Monte Carlo calculations have been made by Bernardini, Booth, and Lindenbaum (1952) for high energy nucleons incident on medium weight elements, and in particular by McManus and Sharp (McManus, Sharp, and Gellmann 1954; McManus and Sharp, unpublished). The evaporation process has been treated by LeCouteur (1950, 1952), and Fujimoto and Yamaguchi (1950), among others. Recently the present writer has discussed (p, xn) reactions in heavy elements, giving a simplified description of neutron evaporation (Jackson 1956).

The present paper presents a theoretical description of spallation yields from heavy elements bombarded by 400 Mev. protons. The Chalk River Monte Carlo calculations (McManus and Sharp, unpublished) are used for the description of the prompt processes, while the evaporation stage is described in a simplified way which suppresses the detailed properties of individual nuclei. Fission as a mode of de-excitation is ignored, although some qualitative remarks are made about it (see Section 5).

The aim of the work has been to combine the theoretical descriptions of the prompt and evaporation processes to yield an over-all, schematic picture of high energy spallation reactions in heavy elements for explicit comparison with experiment. The statistical accuracy of the Monte Carlo computations is not high (see Section 2). Consequently all of the calculated cross sections are uncertain to some extent, aside from the inadequacies of the model employed, and the less likely processes are given only as to order of magnitude. Nevertheless, it is hoped that the present crude calculations will indicate the behavior expected from a model which ignores many-particle and collective effects, such as alpha particle emission and fission.

A summary of the results of the Monte Carlo calculations is presented in Section 2. The model for the evaporation process is outlined in Section 3, while the calculated cross sections are given in Section 4. Comparison with experiment appears in Section 5, and a summary and conclusions in Section 6. Mathematical details of the evaporation model are described in an Appendix.

2. PROMPT PROCESSES

The Monte Carlo calculations for the prompt cascade used in the present work are those of McManus and Sharp (unpublished). These authors employed a weighted two-dimensional model using the observed nucleon-

nucleon scattering cross sections to describe the internal collisions and a Fermi gas model for the nucleons in the nucleus. They distinguished between neutrons and protons, and included Coulomb and centrifugal barriers for the emerging particles by means of cutoffs. The validity of the cutoff procedure was checked by a detailed computation of barrier penetration factors for a sample of the computer runs. Meson production was neglected. The computations were performed on the Ferranti computer at the University of Toronto Computation Centre for both neutrons and protons incident, and for several energies and target elements. The specific results used here are those for 400-Mev. protons incident on uranium, but because of the relative insensitivity of the prompt processes to small changes in nuclear charge and mass, they should be valid for any heavy element.

The computations yield the number, energies, and directions of nucleons emerging from the nucleus for each particle incident. From this information the charge, mass, and excitation of the residual nucleus can be inferred. For the purposes of evaluating reaction yields only the number of neutrons and protons emerging and the state of excitation of the residual nucleus are relevant. The results of computer runs for 200 protons incident at 400 Mev. on uranium are shown in Figs. 1 and 2.

Fig. 1 presents a three-dimensional histogram of the frequency distribution of prompt emission of protons and neutrons. The most probable event is the emission of one neutron and one proton, corresponding generally to a single n - p collision within the nucleus. The distributions are not sharply peaked, however. The mean number of prompt protons (neutrons) emitted per interaction at 400 Mev. is 1.3 (1.6), while the r.m.s. deviation from the mean is 0.9 (1.3). The interaction cross section is 0.84 times the geometrical cross section of the nucleus.

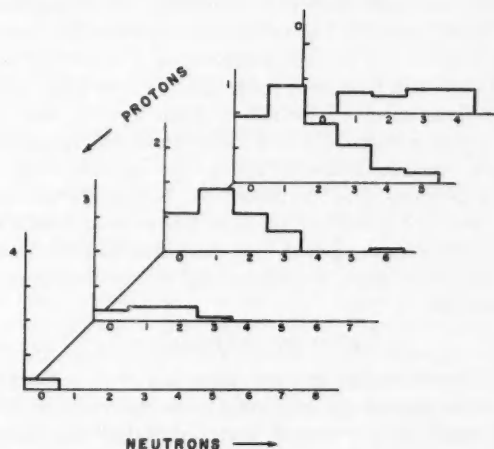


FIG. 1. Calculated frequency distribution of numbers of prompt protons and neutrons ejected from a heavy nucleus bombarded by 400-Mev. protons (McManus and Sharp, unpublished).

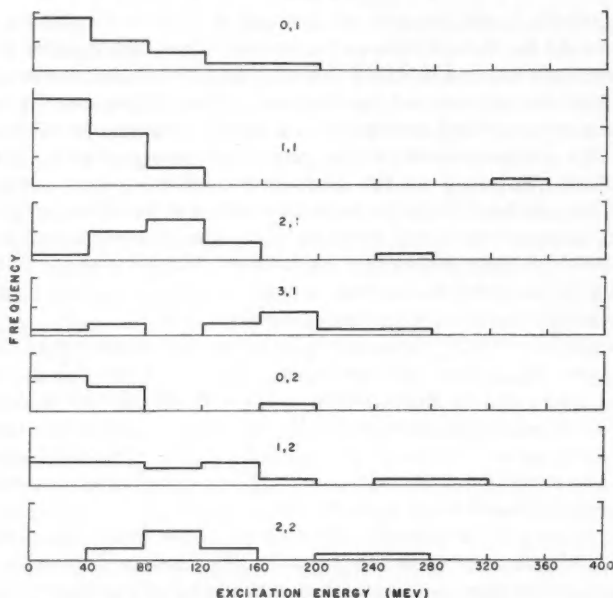


FIG. 2. Calculated distributions of residual excitation for several types of prompt events. The pair of numbers (i, j) correspond to ejection of i prompt neutrons and j prompt protons (McManus and Sharp, unpublished).

In Fig. 2 are shown the residual excitation distributions for various types of prompt events. Only the more probable are presented; even then the statistical accuracy is such that it is necessary to average over 40-Mev. intervals in excitation energy. The events are characterized by two numbers (i, j) corresponding to the prompt emission of i neutrons and j protons. A noteworthy, if expected, feature of these distributions is the peaking towards low energies for those events in which a single proton, two protons, or a neutron and a proton emerge. By and large these events correspond to one dominant nucleon-nucleon collision within the nucleus, with the collision partner perhaps escaping and perhaps not. Relatively small amounts of energy are imparted to the residual nucleus. For interactions in which several neutrons and/or protons are ejected, the excitation distributions are broader and extend to higher energies, corresponding to the development of a sizeable internal cascade.

3. NEUTRON EVAPORATION

Dissipation of the excitation energy remaining after the prompt processes occurs by the successive evaporation of one or more nucleons or groups of nucleons in the well-known manner first elaborated by Weisskopf (1937), (Blatt and Weisskopf 1952). In general the detailed calculation of the relative probabilities of evaporation is very difficult, and only approximate solutions

on the average behavior and the fluctuations have been obtained (LeCouteur 1950, 1952; Fujimoto and Yamaguchi 1950). In heavy nuclei, however, a simplifying assumption can be made. Because of the high Coulomb barriers the emission probabilities for charged particles are very small compared to those for neutrons, and one can to a good approximation neglect all but neutron evaporation.

As will be seen in the next section the averaging of the evaporation probabilities over the broad excitation distributions of Fig. 2 means that only the mean behavior of the evaporation process is important. The details of a simplified evaporation model (Jackson 1956), which assumes a constant nuclear temperature, and its averaged properties are presented in an Appendix, along with the average behavior of neutron evaporation assuming a nuclear temperature varying as the square root of the maximum available energy.

For comparison with experiment it is necessary to know neutron binding energies and empirical nuclear temperatures. Very few neutron binding energies are known experimentally, especially on the neutron deficient side of the stable valley, and one must estimate them from semiempirical mass formulas. In the region of bismuth as a target the mass formula implies that the average neutron binding energy (apart from the odd-even alternation of about ± 0.6 Mev.) increases by about 0.13 Mev. per neutron emitted, and decreases by about 0.2 Mev. per proton emitted for fixed neutron number. For simplicity, in the calculation of the cross sections it was assumed that the average binding energy of successive neutrons was constant and equal to 7.5 Mev., regardless of the mass and charge of the residual nucleus. In view of the statistical uncertainties in the Monte Carlo calculations, as well as lack of knowledge of the nuclear temperature, this simplification will not add appreciably to the uncertainty of the results.

Experimental data on nuclear temperatures at high energies are few. Measurements on the energy spectrum of evaporation neutrons from 190-Mev. proton bombardment of various targets (Gross 1956) imply an average temperature of 1.9 ± 0.1 Mev. and an average excitation energy of 85 ± 15 Mev. for gold and uranium targets. In a similar experiment with 40-Mev. protons Heckman (1956) inferred temperatures of about 1.4 Mev. for heavy elements. On the other hand the shapes and positions of (p, xn) excitation functions for lead and bismuth from 10 to 90 Mev. imply a nuclear temperature of around 1.8 Mev. (Jackson 1956). A reasonable theoretical expectation is that the excitation energy E should be roughly proportional to the square of the nuclear temperature T . Lang and LeCouteur (1954) have made an analysis of the available data at low and high energies to determine an empirical relation between temperature and excitation for various mass numbers. In rough approximation their empirical equation can be replaced by the expression $T^2 = \epsilon E$, where the level density parameter ϵ has the value $\epsilon \simeq (8.5/A)$ Mev. The data of Gross and Heckman for $A \sim 200$ imply $\epsilon \simeq 0.04$ Mev. in good agreement with the empirical expression, while the (p, xn) excitation functions of lead and bismuth at 30 to 40 Mev. would imply $\epsilon \simeq 0.10$.

± 1.5 in neutron number for fixed excitation. In view of the broadness of the distributions of residual excitation shown in Fig. 2 these various possibilities will not lead to qualitatively significant differences in cross sections, although the detailed behavior will depend on the particular dependence assumed. In the calculations of Section 4 two examples are considered: Assumption A—constant binding energy (7.5 Mev.) and constant temperature (1.9 Mev.); Assumption B—constant binding energy (7.5 Mev.), and level density parameter, $\epsilon = 0.075$. The differences in calculated cross sections for these two cases are illustrated in Figs. 5(a) and 5(b).

4. SPALLATION CROSS SECTIONS

The calculation of the individual reaction cross sections follows closely the pattern of the author's paper on (p, xn) reactions (Jackson 1956). Let $Q(i, y, E)dE$ be the probability per inelastic interaction for the prompt emission of i neutrons and y protons, leaving behind a residual nucleus with excitation energy between E and $E+dE$. These probabilities for 400 Mev. protons incident are shown in Fig. 2 for the more likely events. The total probability for the ejection of i prompt neutrons and y prompt protons, illustrated in Fig. 1, is given by

$$(1) \quad q(i, y) = \int Q(i, y, E)dE.$$

The probability $P(j, E)$ that a nucleus of initial excitation E will evaporate exactly j neutrons is described in the Appendix. With the assumption of no charged particle evaporation, the probability per inelastic collision that i prompt neutrons, j evaporation neutrons, and y protons will be emitted is evidently

$$(2) \quad p(i, j, y) = \int Q(i, y, E)P(j, E)dE$$

and the cross section for the emission of x neutrons and y protons is

$$(3) \quad \sigma(xn, yp) = \sigma_r \sum_{i+j=x} p(i, j, y)$$

where σ_r is the total inelastic interaction cross section (approximately 0.84 times geometrical for 400-Mev. protons on heavy elements, from the Monte Carlo calculations). With the neglect of the ejection of aggregates of nucleons, $\sigma(xn, yp)$ is the cross section for formation of the nuclide of mass number $(x+y-1)$ less than, and atomic number $(y-1)$ less than, the target nuclide.

Owing to the comparatively sharp peaking of the neutron evaporation probabilities around the mean energies \bar{E}_j (see Appendix) relative to the excitation distributions of Fig. 2, it is legitimate to approximate $p(i, j, y)$, Eq. (2), by making a Taylor series expansion of $Q(i, y, E)$ around \bar{E}_j . Then Eq. (2) reads

$$(4) \quad p(i, j, y) \simeq \int P(j, E)dE [Q(i, y, \bar{E}_j) + \frac{1}{2}(\Delta E_j)^2 Q''(i, y, \bar{E}_j) + \dots].$$

The integral $\int P(j, E)dE$ can be interpreted approximately as the mean total energy (binding plus kinetic) carried off by a neutron evaporated from a nucleus of excitation \bar{E}_j . This is exact for the constant temperature model

described in the Appendix. If this energy is denoted by $(B+2T)_j$, the probability $p(i, j, y)$ can be written approximately as:

$$(5) \quad p(i, j, y) \simeq (B+2T)_j Q(i, y, \bar{E}_j),$$

the second derivative of $Q(i, y, E)$ with respect to E being ignored.

Using Eqs. (3) and (5) and the information contained in Figs. 2 and 3 the cross sections were evaluated for the two assumptions about neutron evaporation described at the end of the previous section. The results are presented in Figs. 4 and 5. The ordinate scale in both figures is millibarns, based on a total inelastic cross section at 400 Mev. of 1.8 barns. The statistical fluctuations in the Monte Carlo calculations give rise to corresponding fluctuations in the spallation cross sections. The scattered computed points and smooth curves drawn by eye through the points are both shown in Fig. 4

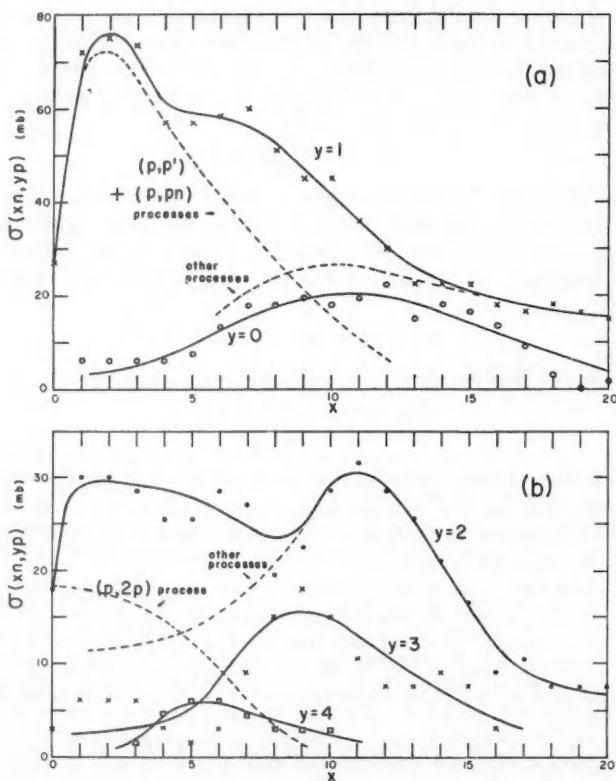


FIG. 4. Calculated spallation cross sections $\sigma(xn, yp)$ for 400-Mev. protons on a heavy element ($A \sim 200$) as functions of x for various values of y , making assumption A (see text). Note the difference in ordinate for parts (a) and (b). The points represent the numerical values obtained with the Monte Carlo calculations. The curves are the smoothed cross sections drawn by eye through the points. The ordinate scale is based on a total inelastic cross section of 1.8 barns.

to indicate the statistical accuracy involved. In Fig. 5 only the smoothed curves are shown. The cross sections in Fig. 4 are for assumption A (constant temperature), while those in Fig. 5 are for assumption B. The manifestations of the differences in the evaporation process implied by assumptions A and B are also presented in Fig. 5, where the cross sections for assumption A (dotted curves) are shown for comparison. It will be seen that the over-all appearance

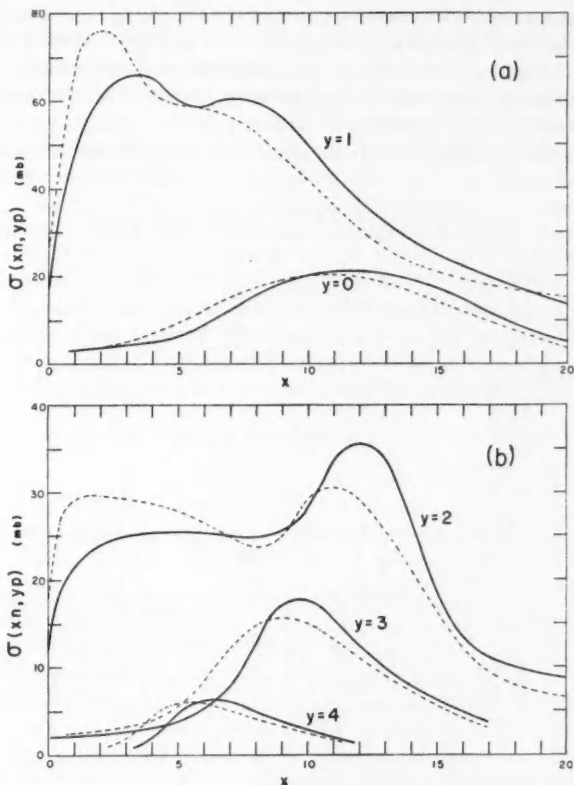


FIG. 5. Calculated spallation cross sections $\sigma(xn, yp)$ for 400-Mev. protons on a heavy element ($A \sim 200$) as functions of x for various values of y , making assumption B. The dotted curves show the corresponding results for assumption A. The ordinate scale is based on a total inelastic cross section of 1.8 barns.

of the two sets of cross sections is very similar, the only essential difference being that the cross sections for B are shifted slightly towards larger neutron number in the region of appreciable cross section. This behavior is what would be expected from Figs. 2 and 3. Fig. 2 shows that most of the excitations lie below 160 Mev., and Fig. 3 shows that at around 100 Mev. assumption B implies emission of roughly one more neutron for a given excitation than assumption A.

It should be noted from Figs. 4 and 5 that for reactions involving the emission of a small number of nucleons the only cross sections which are appreciable are those in which one or two protons are ejected. The reason for this, as discussed at the end of Section 2, is the relatively small amounts of excitation remaining after the prompt (p, p') , (p, pn) , and $(p, 2p)$ processes, which correspond mainly to single internal two-body collisions. For $y = 1$ and 2, the dotted curves in Fig. 4(a) and 4(b) show the decomposition of the cross section into contributions from these single collisions and from the larger internal cascades. Once the "single collision" part is subtracted, the residues of the $y = 1$ and $y = 2$ cross sections behave very similarly to the other cross sections, which peak broadly around 12 nucleons as the most probable number to be emitted.

The calculated cross sections of Figs. 4 and 5 are shown in somewhat different form in Fig. 6. The sum of individual cross sections for fixed mass number gives the so-called "chain yield" cross section. This is plotted in Fig. 6(a) as a function of mass number below the target. For about 10 or

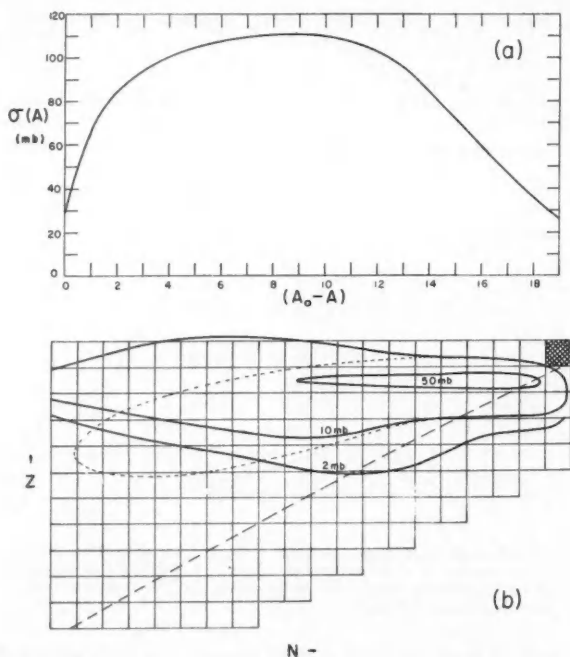


FIG. 6. (a) Calculated cross section for the production of nuclei of a given mass number by 400-Mev. protons on a heavy element ($A \sim 200$) as a function of mass number, A , below the target mass number, A_0 . The total inelastic cross section is assumed to be 1.8 barns.

(b) Contour diagram on the N - Z plane of calculated spallation cross sections for 400-Mev. protons on a heavy element ($A \sim 200$). The shaded square represents the target nucleus plus a proton. The dashed line is the line of stability, while the solid contours are based on Fig. 5. The dotted 10-millibarn contour shows the possible effect of proton evaporation.

12 mass numbers below the target the yield is roughly constant, but it then falls off rapidly to about one fifth of its maximum by 20 mass units below the target.

The cross sections are displayed as a contour diagram on the N - Z plane in Fig. 6(b). The "compound nucleus" (target plus a proton) is shown shaded. The line of stability is given by the dashed curve. The solid contours are based on the cross sections of Fig. 5. To illustrate the possible effects of neglected proton evaporation an estimated 10-millibarn contour, based on the calculations of Fujimoto and Yamaguchi (1950), is dotted in on Fig. 6(b). For less than 10 mass units below the target there is no significant effect, but at 20 mass units below there is an appreciable swinging of the contour downward towards the line of stability. Unfortunately, it is unlikely that an experimental check can ever be made on the individual yields so far from the stable line.

5. COMPARISON WITH EXPERIMENT

The calculated cross sections shown in Figs. 5 and 6 can be compared with available experimental data of Bennett (1954) on the spallation of bismuth by 400-Mev. protons, and of Nervik and Seaborg (1955) on the spallation of tantalum by 340-Mev. protons. The effect of fission can be observed by comparison with the work of Lindner and Osborne (1956) on non-fission, inelastic interactions of thorium and uranium with 340-Mev. protons.

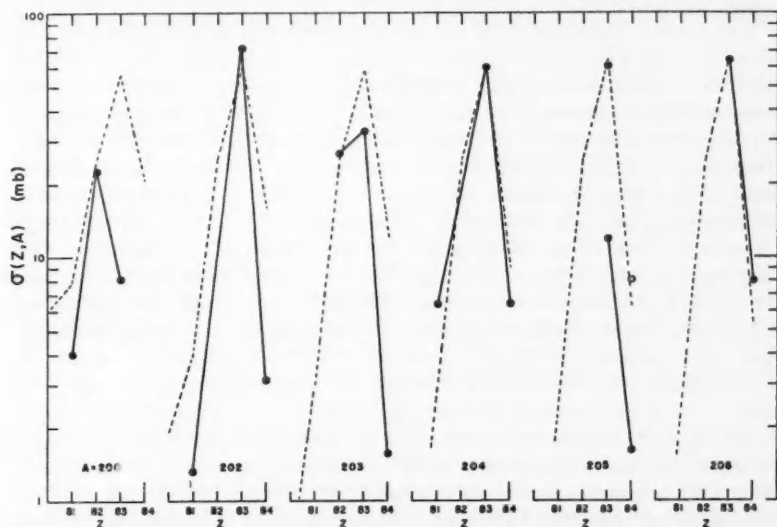


FIG. 7. Comparison of observed and calculated spallation yields for 400-Mev. protons on bismuth, shown as a function of atomic number for various fixed mass numbers. The dashed curves are the calculated results of Fig. 5. The solid points are the data of Bennett (1954). Only the shapes of the experimental yield curves are significant, not their absolute values.

Bennett's cross sections, while quoted in millibarns, are not really absolute yields, but are only relative among the different isobars of a given mass number. Yields of different mass number chains are not interrelated, no correction having been made for counter efficiency. A comparison between Bennett's data and the calculated cross sections is shown in Fig. 7, where the yields of various sets of isobars are plotted as a function of atomic number. For all mass numbers, Bennett's quoted cross sections have been multiplied by a factor of four before being plotted as the solid points. This is not an unreasonable factor on the average to compensate for counter efficiency, although it might be grossly incorrect in specific instances. For $A = 205$, the open circles are Bennett's values multiplied by 20. The dashed lines represent the calculated cross sections from Fig. 5. It will be seen that the shapes of the calculated yield curves are generally in good agreement with the experimental data, and that the over-all correction factor of four gives fair absolute agreement. The chief exceptions are for $A = 205$, where the shape agreement is excellent, but there is a factor of 20 between Bennett's values and the calculated ones; and for $A = 200$, where the experimental yield peaks at $Z = 82$ as compared to $Z = 83$ for the calculated yield. The first exception cannot be regarded as significant until something more is known of the decay scheme and radiations involved. The second disagreement may well reflect the effect of the neglected proton evaporation in the calculations, although the apparent shift in peak with atomic number is somewhat larger than expected.

Nervik and Seaborg's work on the bombardment of tantalum with 340 Mev. protons is devoted to both the spallation and fission regions, although the fission cross section is only about 4 millibarns. Aside from the somewhat lower bombarding energy, their spallation data are not very suitable for detailed comparison with the present calculations because, on the one hand, there are a number of stable nuclides in the region of presumably high yield, and on the other, an appreciable fraction of their data are cumulative chain yields only. Their Fig. 6 (Nervik and Seaborg 1955) shows the estimated cross section for formation of a given mass number as a function of mass number. For mass numbers less than about 10 mass units below the target the yield is relatively flat at around 150 millibarns; by 20 mass units below it has fallen to about 40 millibarns and it is assumed to fall rapidly beyond that. This behavior is roughly consistent with the results shown in Fig. 6(a), although the experimental estimate is 50% larger than the calculated one.

The effect of fission as a mode of decay can be observed clearly by comparing the present calculations, which ignore fission, with non-fission spallation yields from nuclei with appreciable high energy fission cross sections. Such data are recently available from the work of Lindner and Osborne (1956). These authors observed spallation yields from 340-Mev. protons on thorium and uranium. For thorium, fission occurs in roughly 45% of the interactions, while for uranium it occurs more than 70% of the time. The observed spallation cross sections for thorium are shown in Fig. 8, along

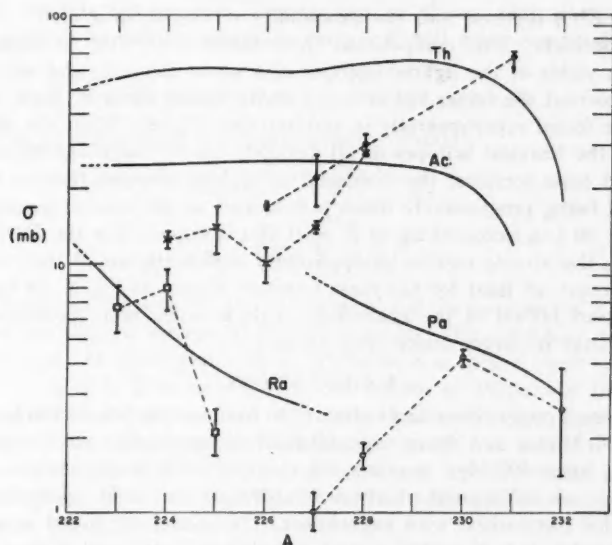


FIG. 8. Comparison of observed (Lindner and Osborne 1956) and calculated spallation yields for 340-Mev. protons on thorium. The open circles are for the Pa ($Z = 91$) isotopes, the solid circles for Th ($Z = 90$), the crosses for Ac ($Z = 89$), and the squares for Ra ($Z = 88$). The solid curves are the calculated cross sections which neglect fission as a mode of decay.

with the calculated cross sections of Fig. 5. The somewhat smaller binding energy for neutrons in thorium as compared to bismuth and lead compensates crudely for the reduction in bombarding energy from 400 Mev. to 340 Mev., so that the cross sections of Fig. 5 would be expected to give a reasonable description of these data if fission were unimportant. The significant feature of Fig. 8 is the fall-off of the yields of the Pa, Th, and Ac isotopes with decreasing mass number as compared to the calculated curves. The yield of the heaviest isotope of each element is in rough agreement with calculation, but the yield of the lighter isotopes falls off rapidly. For the radium isotopes, all the data are in qualitative accord with the calculated curve.

As has been emphasized by Lindner and Osborne, the observed behavior finds an easy explanation in terms of competition between fission and neutron evaporation. The probability of fission, apart from fine effects, depends sensitively on the parameter Z^2/A . This means that for a given mass, the nuclei of higher atomic number will be more prone to fission, and for a given element, the nuclei of smaller mass will be more fissile. On the other hand, for a given excitation, the probability of neutron evaporation will remain essentially unchanged for a group of neighboring nuclei. After the prompt processes a number of different residual nuclei are left with a wide range of different excitations. As neutrons are evaporated from these nuclei, the

values of Z^2/A increase and the probability of fission as a mode of decay rises accordingly. This competition from fission will tend to deplete the spallation yields of the lighter isotopes of a given element, and will be the more important the larger the atomic number of the element. Both of these effects are found experimentally in thorium (see Fig. 8). While the observed yields of the heaviest isotopes of all elements are in rough accord with the calculated cross sections, the yields of the lighter isotopes tend to be less, the effect being progressively more pronounced as the atomic number goes from $Z = 89$ (Ac isotopes) up to $Z = 91$ (Pa isotopes). For the Ra isotopes ($Z = 88$), the atomic number is apparently sufficiently small that fission is not important, at least for the mass numbers shown in Fig. 8. In uranium, the observed fall-off of the spallation yields is much more pronounced, as expected from its larger fission cross section.

6. CONCLUSIONS

The present paper contains an attempt to combine the Monte Carlo calculations of McManus and Sharp (unpublished) on the prompt nuclear processes occurring when 400-Mev. protons are incident on a heavy nucleus with a description of subsequent neutron evaporation to yield spallation cross sections for comparison with experiment. The model employed is one that suppresses detailed characteristics of individual nuclei, and gives an overall schematic picture. The agreement with existing experimental data can be considered adequate where fission is not an important effect. It should be made clear, however, that this agreement does not afford a very sensitive test of the various features of the model. All that can be said is that the Monte Carlo calculations, based on Serber's original ideas, seem correct in broad outline, at least, and that the dissipation of residual excitation proceeds mainly by neutron evaporation. There may be some evidence for proton evaporation where more than 10 nucleons are emitted, but apparently no need to postulate the evaporation of aggregates of nucleons (e.g. alpha particles) as a significant mechanism of de-excitation.

ACKNOWLEDGMENTS

The author wishes to acknowledge the kindness of Dr. H. McManus and Mr. W. T. Sharp in making their unpublished Monte Carlo calculations available to him. He also wishes to thank Professor J. S. Foster and Dr. R. E. Bell for their continued interest in this work.

APPENDIX

The details of a simplified model of neutron evaporation, assuming a constant nuclear temperature, as well as the average behavior of a model in which the temperature varies as the square root of the available energy, are outlined in this appendix.

Constant Temperature Model

If it is assumed that the energy spectrum of evaporated neutrons is given by $U \exp(-U/T)$, where U is the kinetic energy of the neutron and T is the

constant nuclear temperature, then it can be shown that the probability that a nucleus of initial excitation energy E will emit exactly j neutrons is:

$$(A1) \quad P(j, E) = I(\Delta_j, 2j-3) - I(\Delta_{j+1}, 2j-1)$$

where $I(z, n)$ is Pearson's incomplete gamma function

$$(A2) \quad I(z, n) = \frac{1}{n!} \int_0^z x^n e^{-x} dx$$

and

$$\Delta_j = \left(E - \sum_{i=1}^j B_i \right) / T$$

is the energy (in units of T) above threshold for the emission of j neutrons, B_i being the binding energy of the i th neutron. The expression (A1) is in error by terms of order $\exp(-B/T)$ where B is a typical neutron binding energy. For $j = 1, 2$ it agrees with the results of Weisskopf (Blatt and Weisskopf 1952). The behavior of $P(j, E)$ is illustrated in Fig. 2 of the paper by Jackson (1956) for a typical choice of parameters.

In the arguments of Section 4 it is useful to have certain integral properties of the probability function $P(j, E)$. First of all the integral of $P(j, E)$ over all energies is:

$$(A3) \quad \int P(j, E) dE = B_{j+1} + 2T,$$

which is just the average energy (binding plus kinetic) carried off by the $(j+1)$ th neutron. For simplicity of discussion in what follows it will be assumed that the successive neutron binding energies are all constant and equal to B . Nothing essential to understanding is lost by this assumption, and the various formulas are considerably simplified. The mean excitation energy \bar{E}_j for the emission of j neutrons is:

$$(A4) \quad \bar{E}_j = \frac{\int E P(j, E) dE}{\int P(j, E) dE} = j(B+2T) + \frac{(B^2-2T^2)}{2(B+2T)}.$$

As expected, this is linearly proportional to the mean energy carried off per neutron, apart from the small finite intercept at $j = 0$. The energy spread in the distribution $P(j, E)$ can be measured by the r.m.s. deviation ΔE_j from the mean energy \bar{E}_j :

$$(\Delta E_j)^2 = \int (E - \bar{E}_j)^2 P(j, E) dE / \int P(j, E) dE.$$

Performing the necessary integrations using Eqs. (A1) and (A2) gives the result:

$$(A5) \quad (\Delta E_j)^2 = \frac{1}{12} \frac{(B^4 + 8B^3T + 12B^2T^2 - 12T^4)}{(B+2T)^3} + j(2T^2).$$

Again, apart from the small constant term, this expression is just what one would naively write down from the fact that the mean square deviation for the individual spectrum, $U \exp(-U/T)$, is equal to $2T^2$.

The table below illustrates numerically the mean energies and r.m.s. deviations for $B = 7.5$ Mev., $T = 1.9$ Mev., the values used in Fig. 3. It

j	2	4	6	8	10	12	14	16	18	20
\bar{E}_j (Mev.)	25	47	70	92	115	137	160	182	205	228
ΔE_j (Mev.)	4.7	6.0	7.1	8.0	8.8	9.6	10.4	11.0	11.6	12.2

will be noted that the r.m.s. deviations are very small compared to the mean energies; the probability distributions peak relatively sharply around their mean energies.

Mean Behavior of $T^2 = \epsilon E$ Model

Elementary arguments treating the nucleons in a nucleus akin to a degenerate Fermi gas lead to the expectation that the nuclear temperature, T , should vary approximately as the square root of the excitation energy, E . Other models lead to similar power laws with slightly different exponents. The mean behavior of a model based on $T^2 = \epsilon E$, where ϵ is a "level density parameter" with dimensions of energy, can be obtained approximately by analogy with the constant temperature model just described. The level density parameter ϵ will be assumed to be essentially constant for the various nuclei involved in the neutron evaporation process. Actually, ϵ varies slowly with mass number on the average, and has rapid fluctuations depending on the odd-even character of the nucleus.

If a nucleus has a large initial excitation E , the maximum energy available for evaporation of the first neutron is $E_1 = E - B_1$, where B_1 is the first neutron binding energy. The temperature for the evaporation spectrum is therefore $T_1 = (\epsilon E_1)^{1/2}$, and the mean total energy carried off by the first neutron is $U_1 = B_1 + 2T_1$. On the average then, the maximum energy available for second neutron emission is $E_2 = E_1 - U_1 - B_2$, the average temperature is $T_2 = (\epsilon E_2)^{1/2}$, and the mean total energy carried off by the second neutron is $U_2 = B_2 + 2T_2$. The emission of successive neutrons proceeds in this way until the maximum energy available at some stage vanishes. If the mean initial excitation energy for the emission of j neutrons is desired, one must solve the simple set of j simultaneous algebraic equations:

$$(A6) \quad E_\lambda = E - \sum_{\mu=1}^{\lambda} B_\mu - 2 \sum_{\mu=1}^{\lambda-1} T_\mu(E_\mu)$$

where $\lambda = 1, 2, \dots, j$. For the last neutron emitted there is some ambiguity as to whether the energy available should be equal to zero or some finite amount. Taking the constant temperature model as a guide, one should put

$$(A7) \quad E_j = 2T_j(E_j)$$

as the last of the j equations (A6) in order to give the intuitive result,

$$\bar{E}_j = \sum_{i=1}^j (B_i + 2T_i),$$

when constant temperature is assumed. Choices other than (A7) are possible, but the particular value assumed for the energy available for the last neutron is of little consequence as far as the mean excitation energy is concerned,

except for the first few neutrons. In practice, it is simplest to start at the "bottom" and find successively the mean energy for the emission of one neutron, two neutrons, three neutrons, and so on. For various choices of parameters, the results of a computation based on Eqns. (A6) and (A7) are presented in Fig. 3, along with the mean energy for the constant temperature model, given by Eq. (A4).

REFERENCES

- BENNETT, W. E. 1954. *Phys. Rev.* **94**, 997.
BERNARDINI, G., BOOTH, E. T., and LINDENBAUM, S. J. 1952. *Phys. Rev.* **88**, 1017.
BLATT, J. M. and WEISSKOPF, V. F. 1952. *Theoretical nuclear physics* (John Wiley & Sons, Inc., New York), pp. 365-379.
FUJIMOTO, Y. and YAMAGUCHI, Y. 1950. *Progr. Theoret. Phys. (Japan)*, **5**, 787.
GOLDBERGER, M. L. 1948. *Phys. Rev.* **74**, 1269.
GROSS, E. E. 1956. University of California Radiation Laboratory Reports, UCRL 3330, 3337 (unpublished).
HECKMAN, D. 1956. Ph.D. Thesis, McGill University, Montreal, Que.
HORNING, W. and BAUMHOFF, L. 1949. *Phys. Rev.* **75**, 370.
JACKSON, J. D. 1956. *Can. J. Phys.* **34**, 767.
JUNGERMAN, J. and STEINER, H. M. 1956. *Phys. Rev.* **101**, 807.
LANG, J. M. B. and LECOUREUR, K. J. 1954. *Proc. Phys. Soc. (London)*, A, **67**, 586.
LECOUREUR, K. J. 1950. *Proc. Phys. Soc. (London)*, A, **63**, 259.
——— 1952. *Proc. Phys. Soc. (London)*, A, **65**, 718.
LINDNER, M. and OSBORNE, R. N. 1956. *Phys. Rev.* **103**, 378.
MCMANUS, H., SHARP, W. T., and GELLMANN, H. 1954. *Phys. Rev.* **93**, 924A.
MCMANUS, H. and SHARP, W. T. Unpublished.
NERVIK, W. E. and SEABORG, G. T. 1955. *Phys. Rev.* **97**, 1092.
SERBER, R. 1947. *Phys. Rev.* **72**, 1114.
WEISSKOPF, V. F. 1937. *Phys. Rev.* **52**, 295.

THE EFFECTS OF GRAIN BOUNDARIES ON THE PLASTIC DEFORMATION OF ZINC CRYSTALS¹

G. B. CRAIG AND B. CHALMERS²

ABSTRACT

The tensile plastic deformation of single-crystal and tricrystal specimens of zinc was investigated by analysis of the external change in shape of the specimens, and of the changes in X-ray diffraction patterns. It was demonstrated that the single crystals deformed by slip on the basal plane, but pyramidal as well as basal slip occurred in specimens containing grain boundaries.

INTRODUCTION

The purpose of the present investigation was to analyze the mode of deformation of zinc single crystals and to determine how the deformation process was affected by the presence of grain boundaries.

The production, deformation, and calculations of the mode of deformation of zinc single crystals presented little difficulty. The selection of a specimen which would demonstrate the effects of grain boundaries was more difficult. Ideally the study should be conducted on a crystal which is completely enclosed by neighboring crystals, but the problem of producing and measuring the change in shape of such a crystal has not been solved. Therefore, as a first approximation to an enclosed grain, a crystal with two neighbors was chosen.

Zinc was used because only one slip plane (0001) is reported at room temperature. Thus the advent of any other deformation mechanism should be readily apparent.

In order further to simplify the problem it is desirable to eliminate any deformation due to twinning, and also to minimize the internal strains set up by the anisotropy of thermal expansion of the individual zinc crystals. These requirements are satisfied if the angle between the specimen axis and the basal plane is nearly 45 degrees because:

- (a) The shear stress resolved on the basal plane is high,
- (b) Twinning occurs most readily when the stress axis is perpendicular to the *C*-axis,
- (c) The thermal strains which arise during cooling down after solidification of the crystals from the melt are minimized.

To this end, a "tricrystal" test piece consisting of three crystals running longitudinally and comprising a rectangular bar 6 in. long, $\frac{3}{4}$ in. wide, $\frac{1}{4}$ in. thick was evolved. The two outside crystals had identical orientations with the *C*-axis parallel to the top surface and inclined at an angle of 45 degrees to the specimen axis. The center grain was also oriented with the *C*-axis parallel to the top surface and at 45 degrees to the specimen axis, but this latter rotation was in the opposite sense.

¹Manuscript received September 21, 1956.

Contribution from the Department of Metallurgy, University of Toronto, Toronto, Ontario.

²Harvard University, Cambridge, Mass.

EXPERIMENTAL TECHNIQUES

Single-crystal and tricrystal specimens were produced by means of the technique described by Chalmers (1940).

Zinc was supplied by the New Jersey Zinc Co. Ltd., Palmerston, N.J., U.S.A. It had the following analysis:

Zinc	—	99.999%
Pb	—	0.00013
Cd	—	0.00005
Fe	—	0.0006
Cu	—	0.00009
As	—	0.000009

The surfaces of the specimens were polished electrolytically using a technique described by Vernon and Stroud (1938).

The standard Laue back-reflection technique was used to determine crystal orientations before and after deformation.

It was suggested by Orowan (1952) that more detailed examination of the Laue spots and also a measure of lattice disturbances over a wide area could be obtained by a modification of the Laue technique due to Berg. This consisted of using a slit (2 mm. \times 7.2 mm.) to define the line focus of the X-ray beam. The remarkable detail shown by these pictures is shown in Figs. 8 and 9.

In order to measure the change in external shape during deformation a reference network of lines was photoengraved on the top and bottom surfaces of the specimen. The "Pitman Deep Etch Process", a standard photoengraving technique, was found to be most satisfactory for this purpose. Fig. 7 shows a portion of a specimen with engraved grid.

The mechanism of deformation is deduced from the external changes in shape of the specimens. A system of grid lines parallel and perpendicular to the specimen axis (tension axis) permits an analysis of this change in shape to be made.

The measurements made, and the co-ordinate system used for identifying angles during the present investigation, are shown in Fig. 1. All measurements

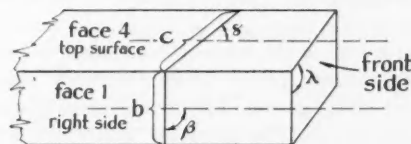


FIG. 1. Measurements used to calculate distortion in metal crystals.

except thickness were made with a travelling stage and microscope and are accurate to ± 0.01 mm. The thickness was measured with a micrometer with spherical tip attachments to provide point contact. This measurement was made to the nearest 0.0001 in. but is subject to the same inaccuracy as the other measurements because of the etched nature of the surfaces. (Etching for 10 seconds was necessary during the photoengraving process.) The lengths

" b " and " c " along the grid lines shown in Fig. 2 are calculated after taking into account the angles γ , β , and λ , e.g., distances were measured parallel and perpendicular to the specimen axis and the actual length of " c " is governed by the angle γ .

The angles γ , β , and λ were calculated from measurements of the top and bottom grid lines. The co-ordinate system used for the top surface of the specimens was maintained for the bottom surface by using a specially machined jig with the same origin for co-ordinates on the top and bottom surfaces.

The measured co-ordinates of the top and bottom grid lines produce directly the extension ($\epsilon = \text{final length}/\text{initial length}$), the dimension " c ", and the angle γ . These co-ordinates plus the thickness measurement enable the dimension " b " and angles β and λ to be calculated as shown in Fig. 2.

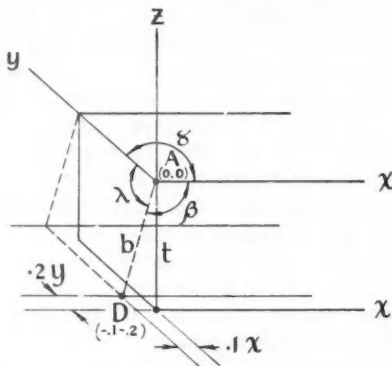


FIG. 2. Angular relationship between γ , β , λ , and the dimensions " t " and " b ". Co-ordinate distances are in millimeters, e.g. $A = (0, 0)$ origin, $D = (-0.1, -0.2)$ from origin, t —micrometer thickness.

The Taylor analysis determines the directions in the crystal which are unchanged in length during the deformation. Now if the deformation is by means of slip on a certain crystallographic plane this fact will be evident immediately, for all the directions in this plane will be unchanged in length. In fact that which is being determined is the cone of intersection between the strain ellipsoid and the undeformed sphere, hence the term "unstretched cone" is used frequently in this investigation. The cone degenerates into two planes if the simple slip process occurs. The plane on which slip actually took place can only be determined by further deforming the crystal and noting that one of these planes is crystallographically unchanged while the other varies. It is concluded that the unchanged plane is the slip plane. Further consideration leads to the conclusion that the slip direction is 90 degrees from the intersection of the two planes and is in the slip plane.

The most convenient way of picturing the analysis is by means of the stereographic projection and this method is used throughout the investigation. The front side of the specimen shown in Fig. 1 is the plane of projection and the

polar co-ordinates of the directions in the specimen which are unchanged in length during the deformation are calculated using the intersection of faces 1 and 4 as the origin for θ , and face 1 as the plane where $\Phi = 0$. Thus Φ is the angle that the projection of the undistorted line makes with face 1, and θ is the angle that the line makes with the intersection of faces 1 and 4.

In order to carry out the type of analysis planned it was essential that no bending or twinning of the crystals occurred. These conditions were fulfilled in all cases, except for one specimen in which twinning occurred.

EXPERIMENTAL RESULTS

(a) Taylor Analysis

Measurements of the changes in external shape of Number 7 single crystal are given in Table IA. The data in Table IA have been used to calculate the

TABLE I
NUMBER 7 SINGLE CRYSTAL
A. DIMENSIONS OF MEAN PARALLELEPIPED
BEFORE AND AFTER DEFORMING

	Before	After
b	5.80 mm.	5.23 mm.
c	2.53 mm.	2.53 mm.
l	2.53 mm.	2.79 mm.
$\epsilon = 1.1028$		
λ	87.8°	85.6°
β	86	93.2
γ	90	91.9

b = length of cross grid on faces 1 and 3.
 c = length of cross grid on faces 2 and 4.
 l = length of longitudinal grid on faces 2 and 4.
 ϵ = final length/initial length.
 λ = angle between faces 1 and 4.
 β = angle between specimen axis and imaginary grid joining equivalent points on faces 2 and 4.
 γ = angle between specimen axis and cross grid on face 4.

B. POLAR CO-ORDINATES OF UNSTRETCHED DIRECTIONS

n	Unstrained material			Strained material		
	Φ_1	θ_1	θ_1'	Φ_2	θ_2	θ_2'
-5	-67.2	57.1	112.2	-71.3	54.6	116.0
-2	-42.1	38.2	116.4	-46.2	35	123.9
-1	-23.9	32.3	117	-26.6	28.9	126.4
0	0	29.7	114.3	0	26.6	124.7
1	23.2	31.5	107.8	24.9	29.2	117.4
2	40.1	36	101.1	41.9	34.5	109.1
5	63.6	49.7	90.7	63.8	49.3	95.5

polar co-ordinates (Φ, θ) for the directions which are unchanged in length during deformation. These co-ordinates are recorded in Table IB and plotted

on stereographic projections in Figs. 3 and 4. The stereographic projections show that in this case the unstretched cones have degenerated into two planes.

A similar analysis was made on the center crystal of Number 8 tricrystal. The external changes in shape of this crystal are given in Table IIA. The polar

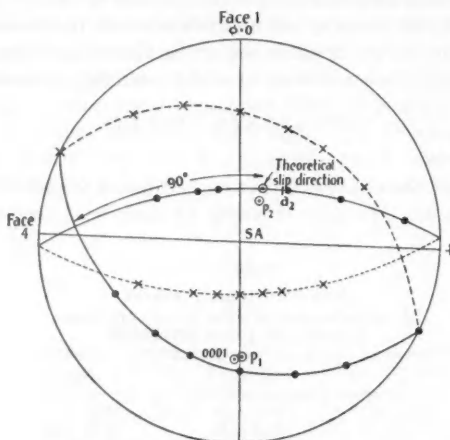


FIG. 3. Number 7 single crystal. Stereographic projection of positions in unstrained material of cone of directions which are unstretched after material has been elongated 10.3%. Theoretical slip direction 90 degrees from intersection of the two planes is marked. Pole of 0001 plane and slip direction a_2 determined from Laue back-reflection patterns are also indicated.

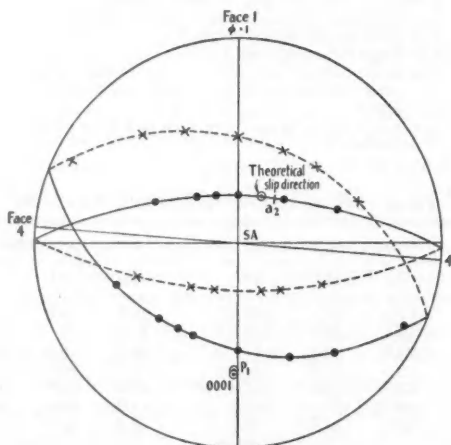


FIG. 4. Number 7 single crystal. Stereographic projection of positions in strained material of cone of directions which are unstretched after material has been elongated 10.3%. Theoretical slip direction is marked. Pole of 0001 plane and slip direction a_2 determined from back-reflection Laue patterns are also plotted.

TABLE II
NUMBER 8 TRICRYSTAL—CENTER CRYSTAL
A. DIMENSIONS OF MEAN PARALLELEPIPED
BEFORE AND AFTER DEFORMING

	Before	After
b	6.32 mm.	6.23 mm.
c	2.53 mm.	2.29 mm.
l	2.52 mm.	2.81 mm.
$\epsilon = 1.115$		
λ	87.5°	89.5°
β	100.9	100.5
γ	89.6	84

B. POLAR CO-ORDINATES OF UNSTRETCHED DIRECTIONS

n	Unstrained material			Strained material		
	Φ_1	θ_1	θ_1'	Φ_2	θ_2	θ_2'
-2	-39.6	57.6	109.5	-36.5	55.1	113.6
-1	-22.2	71.3	107.3	-20.3	69.3	109.5
0	0	78.8	116.3	0	75.6	117.7
1	21.5	72.3	131.5	20.1	66.6	133.8
2	37.7	67.8	138.6	36.2	60.5	141.4
4	56.2	65	143.8	55.4	56	147.3

co-ordinates of the unstretched directions are recorded in Table IIB, and the unstretched cones are plotted in Figs. 5 and 6. It is at once evident that the unstretched directions no longer lie on two planes.

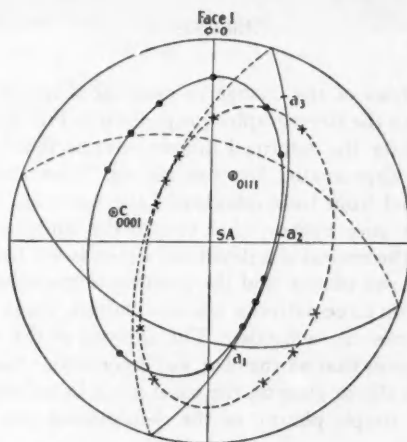


FIG. 5. Number 8 tricrystal. Stereographic projection of positions in the unstrained material of cone of directions which are unstretched after material has been elongated 11%. Position of the basal and pyramidal planes as determined by back-reflection Laue patterns is also plotted.

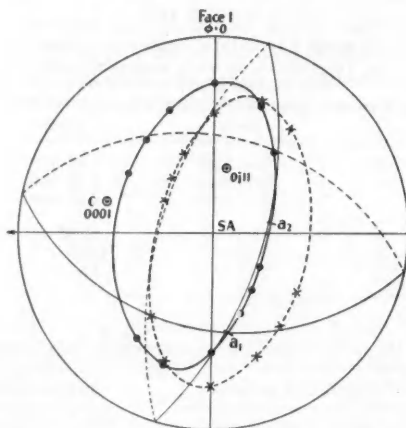


FIG. 6. Number 8 tricrystal. Stereographic projection of positions in the strained material of cone of directions which are unstretched after material has been elongated 11%. Position of basal and pyramidal planes as determined from Laue patterns is shown.

(b) *X-Ray Diffraction*

X-ray diffraction patterns representative of those obtained on deformed single crystals and the center crystal of deformed tricrystals are shown in Figs. 8 and 9. The Laue back-reflection patterns from the center crystal of Number 8 tricrystal show a most pronounced form of streaking after deformation. The Berg patterns from the center crystal are also greatly transformed as shown in Fig. 9.

DISCUSSION

Single Crystals

The Taylor analysis of the change in external shape of Number 7 single crystal, as plotted on the stereographic projections in Fig. 3 for the undeformed sample, and Fig. 4 for the deformed sample, reveals that in this case the unstretched cone has degenerated into two planes. When the pole of the basal plane, as determined from back-reflection Laue patterns, is plotted on these projections it is at once evident that one of the undeformed planes is the (0001) plane. The theoretical slip direction, which is 90° from the intersection of the two undeformed planes, and the position of the close packed direction (a_2), determined from Laue patterns, are also plotted. These directions are seen to be within 6 degrees of each other. The analysis of the external change in shape, therefore, shows that all the observed deformation can be accounted for by means of simple slip or glide on the basal plane in a close packed direction. This confirms the simple picture of the deformation process arrived at by earlier investigators.

The Laue X-ray patterns also support this conclusion, i.e., that the deformation proceeds by means of simple glide on the basal plane, in two ways: firstly, the basal plane rotates towards the specimen axis in the close packed direction dictated by the maximum resolved shear stress law; secondly, the

PLATE I

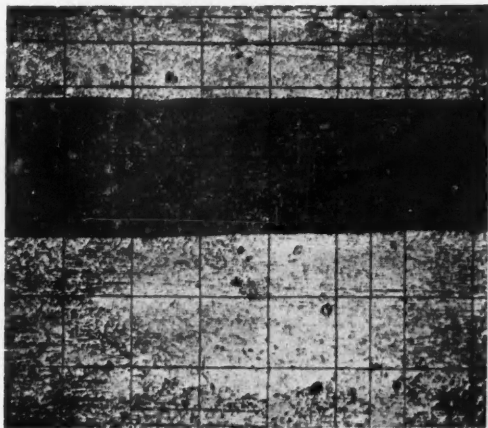


FIG. 7. Grid engraved on zinc tricrystal specimen. G. I. Taylor analysis (Taylor and Elam 1922-1923).

PLATE II

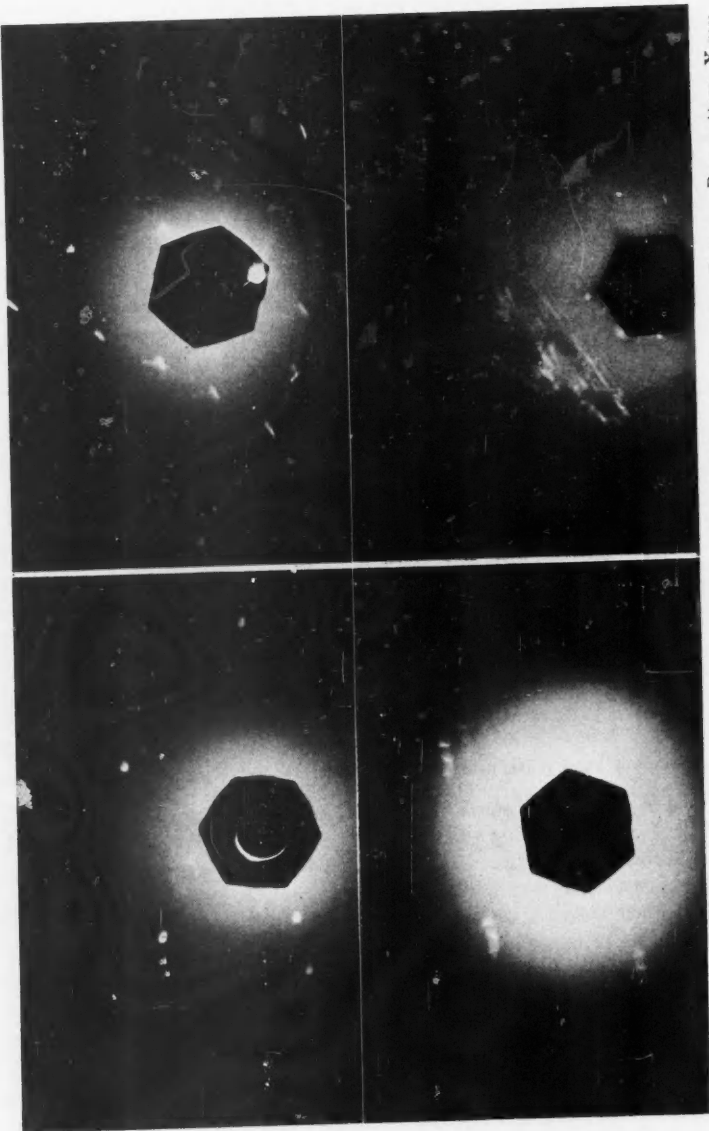


FIG. 8. Top—Laue pattern. Bottom—Berg pattern. X-ray back-reflection patterns from Number 7 single crystal after deformation.

FIG. 9. Top—Laue pattern. Bottom—Berg pattern. X-ray back-reflection patterns from the center crystal of Number 8 tritricrystal after deformation.

Laue spots themselves are sharp after deformation, indicating little or no disturbance of the regular crystal symmetry. Fig. 8 shows that deformation has not altered the sharpness of the diffraction spots. The undistorted nature of the Berg pattern shown in Fig. 8 is also evidence that simple slip has occurred.

Tricrystals

The observations on the mode of deformation of the center crystal of Number 8 tricrystal will now be considered. If we plot the position of the basal plane, as determined by Laue patterns, on the stereographic projections, Figs. 5 and 6, which show the unstretched directions in this crystal, it is seen that there is some relation between the major axes of the cones and that of the basal plane. It is not at once evident what this relation is or why it exists. Since the basal plane intersects the cone at a direction of close packing, i.e., a_1 , we are led to consider the possibility of a second slip plane which intersects the basal plane in this line. A consideration of lowest energy dislocations (Chalmers and Martius 1952) shows that the next operative slip plane should be a type I pyramidal plane ($0\bar{1}11$). All these pyramidal planes intersect the basal plane along the closest packed directions (a_1, a_2, a_3). That pyramidal plane which has the maximum resolved shear stress acting on it should operate.

The ($0\bar{1}11$) plane has the maximum resolved shear stress and, therefore, should operate if pyramidal slip occurs. This pyramidal plane is plotted in Figs. 5 and 6 and we see that the cone, the basal plane, and this pyramidal plane all intersect near the a_1 direction. This strongly suggests that the observed deformation is due to slip on the basal plane plus slip on the pyramidal plane, since the analysis of the external change in shape shows that this direction, i.e., the line of intersection, is unchanged in length during the deformation.

X-Ray Evidence for Pyramidal Slip Plus Basal Slip

The zone streaking which appeared on the Laue back-reflection patterns from the deformed crystals supports the view that pyramidal plus basal slip

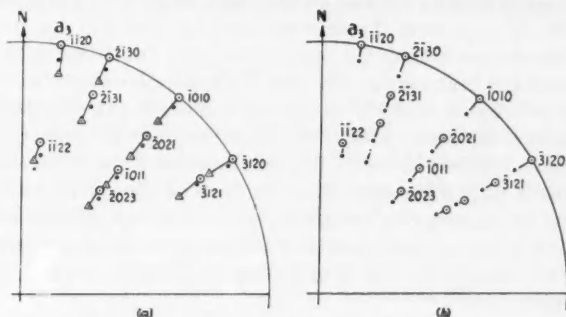


FIG. 10. (a) Stereographic projection showing initial position of Laue spots (dots). Calculated position of Laue spots due to basal slip (O circles). Calculated position of Laue spots due to pyramidal slip (Δ triangles).

(b) Stereographic projection of the streaking observed in Laue back-reflection patterns from the center crystal of the deformed tricrystal.

occurred. The streaks were plotted on a standard stereographic projection, a quarter section of which is shown in Fig. 10(b). Now if we consider the rotations of the lattice planes which take place, first for basal slip and then for pyramidal slip (Fig. 10(a)), we see that the lines joining this orientation range correspond to our streaking X-ray pattern. In a single crystal the whole lattice rotates uniformly from initial to final position, whereas in this case portions of the lattice are rotated to a greater or lesser extent in the slip direction. This is, of course, a special case of deformation bands and perhaps will lead to a better understanding of the nature of these bands.

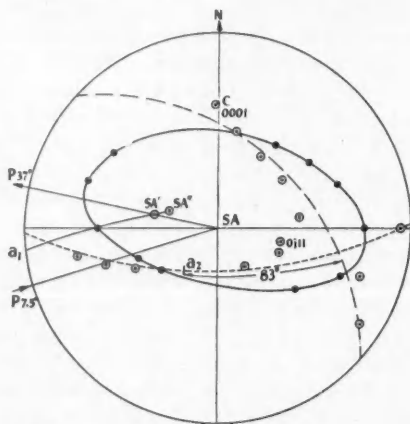


FIG. 11. Stereographic projection showing how the "unstretched cone" degenerates into two planes when the rotations of the lattice due to pyramidal slip are reversed. First rotation ($P\ 37^\circ$) makes (0111) plane the basic circle. Second rotation ($P\ 7.5^\circ$) reverses the rotation due to pyramidal slip. C-axis and basal plane (dashes) are plotted from X-ray data.

On the assumption that pyramidal slip is operative, the component of the lattice rotation arising as a result of this slip system can be calculated to be 7.5° (Fig. 10). If we reverse the deformation (theoretically) due to pyramidal slip we arrive at a position of the unstretched cone which is due to basal slip. This operation has been carried out, and the results are shown in Fig. 11. We see that the cone has reverted to two planes and our X-ray data show that one of these planes is the basal plane. The theoretical glide direction is also shown and we see that it differs by only 7 degrees from one of the directions of closest atomic packing (a_2) in the slip plane. In view of the errors inherent in the experimental techniques this is regarded as satisfactory agreement.

Only slip lines due to basal glide were visible on the surfaces of the deformed crystals. One explanation for this is that the etched surface masked the pyramidal glide bands.

There is, however, direct X-ray evidence in both the Laue and Berg patterns that disturbances of the lattice in directions other than those accountable for by basal plane glide took place. The streaking in the Laue patterns, and the pronounced break-up of the Berg patterns, are so markedly different from those

obtained on Number 7 single crystal which deformed by pure slip that there is not the slightest doubt that some other mechanism is operative.

The work of Rohm and Kochendorfer (1950) shows that homogeneous shear deformations up to 20-25% in long aluminum crystals produce no macroscopic slip bands and no asterism in Laue back-reflection X-ray patterns.

It is, therefore, considered that the absence of visible slip bands due to pyramidal slip does not contradict the argument for deformation by this mechanism.

The analysis reported was carried out on a very simple crystal configuration and it is certain that in normal polycrystals many further complications arise. Two cases of interest in this respect were encountered in the course of the present investigation.

First was a tricrystal similar in orientation to Number 8 tricrystal. It had, however, one more complicating factor as far as the deformation process is concerned. This was the wavy or irregular nature of the two grain boundaries. This so altered the stress distribution that twin crystals formed in the center crystal. These twin crystals made a Taylor type analysis of the external change in shape impossible and also spoiled the X-ray patterns as far as measuring the rotation of the specimen axis was concerned.

The presence of large angle striation* boundaries (2-10 degrees) in a single crystal also altered the mode of deformation. A complete analysis of this case was not made but it appears likely that the operation of a second slip system could account for the observed changes in the deformation process.

CONCLUSIONS

1. It is concluded that the presence of grain boundaries in zinc crystals modifies the simple basal slip mechanism which is observed when striation-free single crystals are deformed. The modification in the case investigated was the operation of an additional pyramidal slip plane. This result could not be predicted from tests carried out on single crystals.

2. The observed deformation of a striation-free single crystal (Number 7) can all be accounted for by means of slip on the basal plane in the close packed direction.

ACKNOWLEDGMENTS

The authors wish to express their indebtedness to the National Research Council, Ottawa, and the School of Engineering Research of the University of Toronto, for financial assistance, and to the New Jersey Zinc Co., Palmerston, N.J., for the high purity zinc. Also to Dr. Ursula Martius, for helpful discussions throughout the course of the investigation.

REFERENCES

- CHALMERS, B. 1940. *Proc. Roy. Soc. A*, **175**, 100.
CHALMERS, B. and MARTIUS, U. 1952. *Proc. Roy. Soc. A*, **213**, 175.
OROWAN, E. 1952. Personal communication.
ROHM, F. and KOCHENDORFER, A. 1950. *Z. Metallkunde*, **41**, 265.
TAYLOR, G. I. and ELAM, C. F. 1922-23. *Proc. Roy. Soc. A*, **102**, 643.
VERNON, W. H. J. and STROUD, E. G. 1938. *Nature*, **142**, 477, 1161.

*These boundaries are lineage structure found in crystals grown from the melt.

NUMERICAL ANALYSIS OF A UNITARY PARTICLE MODEL¹

F. A. KAEMPFFER AND EDITH M. KENNEDY

ABSTRACT

A classical unitary field model describing a family of electrically uncharged heavy particles is analyzed numerically. A reasonable mass spectrum is obtained. Limitations of the model are stated.

1. INTRODUCTION

Ever since Mie (1912) published his famous program, unitary theories of the so-called elementary particles have remained in what might be called a state of animated suspension. New attempts in the spirit of Mie keep appearing in the literature, but although they raise high hopes by establishing the feasibility of a unitary theory, none of them has yet succeeded in predicting the outcome of a single experiment.

The aim of the investigation reported in this paper was not to enlarge on the general feasibility of unitary particle theory, but rather to study the numerical feasibility of a known model, which appears attractive from a general point of view, and, if possible, to develop a feeling for the order of magnitude of the parameters characterizing this model.

In particular, the family of heavy particles, consisting of nucleons and hyperons, was taken as the reality to which the model under consideration should correspond. The reason for this particular choice is that all unitary models to be discussed below describe a "particle" in terms of self-maintained solutions of certain nonlinear differential equations, which allow for the existence of a "ground state" together with "excited states", a situation resembling most closely the relation between the various members of the heavy particle family.

It will be found that one can obtain reasonable values for the mass spectrum. The description of the decays of the various particles and the prediction of their lifetimes, however, is beyond the reach of present unitary theories.

2. EXISTING UNITARY THEORIES

Existing unitary theories may be separated naturally into three groups:

(1) Purely classical field theories, in which the cohesion of particles is provided by either

(1a) coupling of the field to itself, or

(1b) coupling of two fields, each acting as the glue which holds the other together.

Models resulting from this approach have been studied by Rosen (1939), Finkelstein (1949), and others.

¹Manuscript received August 13, 1956.

Contribution from the Department of Physics, The University of British Columbia, Vancouver 8, B.C.

(2) Quantum field theories, with coupling of the field to itself. This approach has been followed by Heisenberg (1954) and others.

(3) Field theories in which a classical "source" is coupled to a quantized "glue". The feasibility of this intermediate type of model was first pointed out by Heber (1955).

The interpretation of models resulting from the approach (2) meets with great difficulties, as has been shown by Kita (1956), and so far no model of type (3) is known which will correspond to a particle with positive mass. Therefore the work reported in this paper was confined to a model of type (1).

3. SUMMARY OF FORMALISM

The field equations governing a classical unitary theory may be derived, as usual, from a variational principle requiring that the action integral

$$(3.1) \quad I = \int \mathcal{L} d^4x$$

be an extremum, where $\mathcal{L} = \mathcal{L}(\psi_i, \partial\psi_i/\partial x_\mu, \dots)$ is the Lagrangian density. The conservation laws for momentum, energy, and electric charge follow from invariance properties of the Lagrangian (see e.g. Wentzel 1943) and take the form

$$(3.2) \quad \partial T_{\mu\nu}/\partial x_\mu = 0, \quad \partial s_\mu/\partial x_\mu = 0,$$

where energy momentum density tensor $T_{\mu\nu}$ and charge current density vector s_μ are defined by

$$(3.3) \quad T_{\mu\nu} = -\frac{\partial \mathcal{L}}{\partial(\partial\psi_i/\partial x_\mu)} \frac{\partial\psi_i}{\partial x_\nu} + \mathcal{L}\delta_{\mu\nu},$$

$$s_\mu = ie\left(\frac{\partial \mathcal{L}}{\partial(\partial\psi_i/\partial x_\mu)} \psi_i - \frac{\partial \mathcal{L}}{\partial(\partial\psi_i^*/\partial x_\mu)} \psi_i^*\right).$$

Now any solution of the field equations following from (3.1), which is free from singularities, is interpreted as a particle of mass

$$(3.4) \quad m = -\frac{1}{c^2} \int T_{44} d^3x$$

and charge

$$(3.5) \quad e = -\frac{i}{c} \int s_4 d^3x.$$

It is evident from the definition of the charge current density vector that a theory with real fields ψ_i only describes an electrically uncharged field and therefore neutral particles, and that charged particles may be obtained only if at least one of the field variables is complex and time dependent.

4. THE SPECIFIC MODEL

For the numerical investigation a specific model was chosen, characterized by the Lagrangian density

$$(4.1) \quad \mathcal{L} = -\frac{\partial \psi}{\partial x_\mu} \frac{\partial \psi^*}{\partial x_\mu} - \kappa^2 \psi \psi^* - \frac{\partial \phi}{\partial x_\mu} \frac{\partial \phi}{\partial x_\mu} + g \psi \psi^* \phi^2, \quad g > 0.$$

The corresponding field equations are

$$(4.2) \quad \square \psi - \kappa^2 \psi = -g \psi \phi^2,$$

$$(4.3) \quad \square \phi = -g \psi \psi^* \phi.$$

By analogy with orthodox quantum field theory one may think of these as describing a "bare" nucleon field ψ of "bare" mass $m = \kappa \hbar/c$ coupled to a massless meson field ϕ . The main reason for this choice is its simplicity and the fact that particles of positive mass result from it. It will also be shown later that assignment of a "bare" mass μ to the meson field ϕ does not alter appreciably the features of this model, provided $\mu/m \ll 1$.

To make the nonlinear simultaneous system of equations (4.2) and (4.3) accessible to numerical treatment only static spherically symmetric solutions of the type

$$(4.4) \quad \psi = \psi(r), \quad \phi = \phi(r), \quad \psi \text{ real},$$

are considered. By the substitutions

$$(4.5) \quad x = \kappa r, \quad u = \sqrt{g} r \psi, \quad v = \sqrt{g} r \phi$$

the field equations reduce to

$$(4.6) \quad u'' = u \left(1 - \frac{v^2}{x^2} \right),$$

$$(4.7) \quad v'' = -v \left(\frac{u^2}{x^2} \right),$$

which should yield particle-like solutions if they are subjected to the boundary conditions (see Rosen 1939)

$$(4.8) \quad \left. \begin{matrix} u = 0 \\ v = 0 \end{matrix} \right\} \text{ at } x = 0, \quad \left. \begin{matrix} u/x \rightarrow 0 \\ v/x \rightarrow 0 \end{matrix} \right\} \text{ as } x \rightarrow \infty.$$

By inspection of the differential equations (4.6) and (4.7) it is seen that

$$(4.9) \quad \begin{aligned} u'' &< 0 \text{ if } v/x > 1, & u'' &> 0 \text{ if } v/x < 1, \\ v'' &< 0 \text{ for all } x > 0. \end{aligned}$$

It is therefore to be expected that the differential equations and boundary conditions will in general allow solutions with u having no nodes, one node, two nodes, etc. If each such solution is interpreted as a particle, one has a model which allows, in principle, the calculation of a mass spectrum of various members of an electrically neutral particle family described by these equations, using definition (3.4) with

$$(4.10) \quad T_{44} = -\{(\kappa^2 - g\phi^2)\psi^2 + (\nabla\psi)^2 + (\nabla\phi)^2\}$$

in this case.

5. APPROXIMATION PROCEDURE

Since an exact solution of the equations (4.6) and (4.7) seems out of reach, the following approximation procedure was adopted. Let, in crude approximation,

$$(5.1) \quad v = \begin{cases} v_1 = ax & \text{for } x \leq x_0, \\ v_2 = ax_0 & \text{for } x > x_0, \end{cases}$$

where a and x_0 are constant parameters to be determined later. Then equation (4.6) becomes

$$(5.2) \quad u'' = \begin{cases} u(1-a^2) & \text{for } x \leq x_0, \\ u[1-(ax_0/x)^2] & \text{for } x > x_0. \end{cases}$$

For $a < 1$ one has from (5.2) $u'' > 0$ for all x , and for $a = 1$ one has $u'' = 0$ for $x \leq x_0$ and $u'' > 0$ for $x > x_0$. In either case u/x does not vanish as $x \rightarrow \infty$, in contradiction to the boundary condition. Therefore one requires

$$(5.3) \quad a > 1.$$

Equations (5.2) now yield, together with the boundary conditions,

$$(5.4) \quad u = \begin{cases} B \sin(\sqrt{a^2-1} x) & \text{for } x \leq x_0, \\ C \exp(-x) & \text{for } x > x_0. \end{cases}$$

This solution is approximated again by writing

$$(5.5) \quad u = \begin{cases} u_1 = B \sin(\sqrt{a^2-1} x) & \text{for } x \leq x_0, \\ u_2 = C \exp(-x) & \text{for } x > x_0, \end{cases}$$

with B and C constants, and requiring that u and u' be continuous at $x = x_0$. This latter requirement yields

$$(5.6) \quad B = \frac{C \exp(-x_0)}{\sin(\sqrt{a^2-1} x_0)}, \quad x_0 = \frac{\tan^{-1}(-\sqrt{a^2-1})}{\sqrt{a^2-1}},$$

where one must have

$$(5.7) \quad \begin{aligned} \pi/2 &< \sqrt{a^2-1} x_0 < \pi && \text{for the nodeless solution,} \\ 3\pi/2 &< \sqrt{a^2-1} x_0 < 2\pi && \text{for the one-node solution,} \\ 5\pi/2 &< \sqrt{a^2-1} x_0 < 3\pi && \text{for the two-node solution, etc.} \end{aligned}$$

From (5.6) one can eliminate B and a , using (5.7) for the respective solutions. The model is therefore characterized by the four parameters C , x_0 , g , κ . For the numerical calculation it was found convenient to express C in terms of the normalization constant n , defined for dimensional reasons by

$$(5.8) \quad \int \psi^2 d^3x = \frac{n}{\kappa g},$$

so that n is a pure number and \mathcal{L} is an energy density. The parameters fixing the model are thus n , x_0 , g , κ . Substituting then the solutions into (3.4), using (4.10), and performing an integration by parts, one obtains

$$(5.9) \quad H = mc^2 = \int g \phi^2 \psi^2 d^3x = \frac{n\kappa}{g} \left(\frac{Y_1 + Y_2}{Y_3} \right)$$

where

$$\begin{aligned}
 Y_1 &= \frac{a^2}{\sqrt{a^2-1}} \frac{1}{\sin^2(\sqrt{a^2-1} x_0)} \\
 &\quad \times \{ \sqrt{a^2-1} x_0 - \cos(\sqrt{a^2-1} x_0) \sin(\sqrt{a^2-1} x_0) \}, \\
 (5.10) \quad Y_2 &= 2a^2 x_0 - 4(ax_0)^2 \exp(2x_0) \int_{2x_0}^{\infty} \frac{\exp(-u)}{u} du, \\
 Y_3 &= 1 + \frac{1}{\sin^2(\sqrt{a^2-1} x_0)} \\
 &\quad \times \{ \sqrt{a^2-1} x_0 - \cos(\sqrt{a^2-1} x_0) \sin(\sqrt{a^2-1} x_0) \},
 \end{aligned}$$

with a to be determined numerically from (5.6) and (5.7) for the nodeless, one-node, two-node, etc. solution respectively.

6. NUMERICAL RESULTS

The dimensionless quantity $Hg/n\kappa$ was calculated numerically for a range of values of the parameter x_0 for each of the three cases corresponding to no node, one node, and two nodes in ψ respectively. Solutions with more than two nodes in ψ were not considered, although such solutions do, of course, exist. The results of this calculation are tabulated in Table I and plotted in Fig. 1.

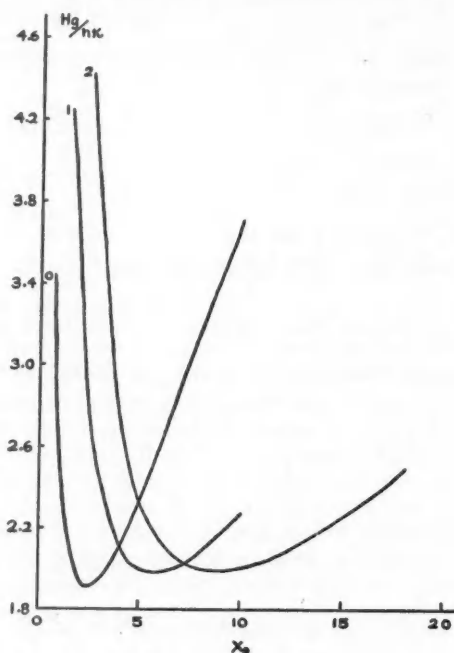


FIG. 1. The variation of $Hg/n\kappa$ with x_0 . At the beginning of each curve is shown the number of nodes in the corresponding ψ -field.

TABLE I

VALUES OF $Hg/n\kappa$ AND CORRESPONDING VALUES OF x_0 FOR THE NODELESS, ONE-NODE, AND TWO-NODE SOLUTIONS

Nodeless solution		One-node solution		Two-node solution	
x_0	$Hg/n\kappa$	x_0	$Hg/n\kappa$	x_0	$Hg/n\kappa$
0.70	3.377	1.50	4.249	2.50	4.409
1.20	2.336	2.75	2.546	4.00	2.708
2.00	1.950	4.50	2.033	6.00	2.153
2.40	1.9186	5.00	1.9942	8.00	2.001
2.45	1.9148	5.50	1.9777	8.50	1.9911
2.50	1.9185	5.75	1.9759	9.00	1.9884
2.60	1.921	6.00	1.9778	9.50	1.9921
3.00	1.950	6.50	1.9906	11.00	2.030
4.50	2.211	7.00	2.013	18.00	2.479
7.50	2.987	10.00	2.270		
10.00	3.713				

The graph of $Hg/n\kappa$ versus x_0 shows that there is one value of x_0 in each case for which $Hg/n\kappa$, and hence the energy, H , is a minimum. The existence of these minima is the most remarkable feature of this model. The authors argue that if this model has any relation to reality, one should consider the particular solutions which yield the minimum energy in the three cases as the ones representing three possible neutral particles in their normal states and use the corresponding values of $r = x_0/\kappa$ as a measure of the size of these particles. The mass ratios are independent of n , κ , and g within the limits of the approximations used and are found to be

$$(6.1) \quad m_0 : m_1 : m_2 = 1 : 1.032 : 1.038.$$

The ratios of the radii are also independent of n , κ , and g in the same sense and are found to be

$$(6.2) \quad r_0 : r_1 : r_2 = 1 : 2.34 : 3.67.$$

The values of x_0 are those found by approximating $Hg/n\kappa$ by a parabola in the vicinity of the respective minima.

By comparison the mass spectrum of the known neutral members of the heavy particle family is described by the ratios

$$(6.3) \quad m_N : m_A : m_X = 1 : 1.18 : 1.26.$$

Expressed in terms of n , κ , g the rest mass m_0 and the radius r_0 of the smallest particle described by the model are

$$(6.4) \quad m_0 = 2.13 \times 10^{-21} n\kappa/g \text{ gram}, \quad r_0 = 2.45\kappa^{-1} \text{ cm.}$$

By equating these expressions with the values found experimentally for the nucleon, namely $m_N = 1.67 \times 10^{-24}$ gram and $r_0 = 0.8 \times 10^{-13}$ cm., one obtains the further relations

$$(6.5) \quad \kappa = 3.06 \times 10^{13} \text{ cm}^{-1}$$

and

$$(6.6) \quad n/g = 2.56 \times 10^{-17} \text{ c.g.s.}$$

It is interesting to note that the value (6.5) for κ corresponds to assigning the "bare" nucleon field ψ a rest mass

$$(6.7) \quad m = 1185 m_{\text{electron}}$$

The theory does not yield n and g separately by comparison with experimental values. In view of the simplicity of the model and the crudeness of the approximations used it is felt that the theoretical values (6.1), (6.2), and (6.5) can be considered as reasonable.

One may try to improve the theoretical mass spectrum (6.1) by assigning a "bare" mass not only to the ψ -field but to the ϕ -field as well. This has been investigated and it was found that the general method developed in Section 5 will still work provided the "bare" mass μ of the ϕ -field is small compared with the "bare" mass m of the ψ -field. In particular, by choosing the ratio μ/m to be $1/6$, assuming thus that the "bare" mass ratio reflects approximately the observable mass ratio of the corresponding "dressed" particles, it was found that the resulting modification of the first half of the mass spectrum (6.1) is

$$(6.8) \quad m_0' : m_1' = 1 : 1.034.$$

It appears thus that such modifications will not yield any significant new information and this matter was, therefore, not pursued any further. The assumption that "bare" mass ratios reflect the observable mass ratios of "dressed" particles is highly dubious in any case.

It is obviously beyond the capacity of the specific model treated in this paper to describe instability and predict the lifetime of certain particles. Quantization of electric charge also cannot be grasped within the framework of such a purely classical model. In fact, if $\psi(r)$ is a solution of the field equations, then $\psi \exp(i\omega t)$ is also a solution for any value of ω , and it is easily verified that the minima of the curves $Hg/n\kappa$ versus x_0 occur for the same values of x_0 as in the case $\omega = 0$. By definition (3.5) solutions with $\omega \neq 0$ describe an electric charge

$$(6.9) \quad e = \epsilon \omega n / c^2 \alpha g, \quad \alpha^2 = \kappa^2 - \omega^2 / c^2$$

carried by the particle, where ϵ is a scale factor. Clearly, e remains completely undetermined in the classical theory. One may entertain the hope, however, particularly in view of Heber's (1955) interesting results, that the minima of the energy, occurring for certain values of the spatial extension of the particles, are a feature of the theory which will survive incorporation of quantum postulates in this type of model.

ACKNOWLEDGMENT

The financial assistance of the National Research Council in the form of a Research Associateship (F.A.K.) and a Bursary (E.M.K.) is gratefully acknowledged.

REFERENCES

- FINKELSTEIN, R. J. 1949. *Phys. Rev.* **75**, 1079.
 HEBER, G. 1955. *Ann. Physik*, **16**, 43.
 HEISENBERG, W. 1954. *Z. Naturforsch.* **9a**, 292.
 KITA, H. 1956. *Progr. Theoret. Phys. (Japan)*, **15**, 83.
 MIE, G. 1912. *Ann. Physik*, **37**, 511; **39**, 1.
 ROSEN, N. 1939. *Phys. Rev.* **55**, 94.
 WENTZEL, G. 1943. *Quantentheorie der Wellenfelder* (Verlag Franz Deuticke, Wien).

MULTILAYER PROBLEMS IN THE SPHERICAL HARMONICS METHOD¹

B. DAVISON

ABSTRACT

In applying the spherical harmonics method to multilayer problems it is necessary to invert certain matrices. It is shown, for the cases of plane and spherical symmetry, that these inverse matrices can easily be written down explicitly, so that there is no need for numerical matrix inversion.

1. INTRODUCTION

In the present note we are concerned with neutron transport problems in one-velocity theory for multilayer systems with plane or spherical symmetry. One of the more powerful methods for dealing with neutron transport theory is the spherical harmonics method. For the case of a single medium its theory is well known (Mark 1944, 1945; Davison 1956), but the technique of its application to multilayer problems has not yet received sufficient attention. An important and, unless properly handled, the most laborious part of the calculations in applying this method to such systems is to express the "arbitrary" constants (constants of integration) for each consecutive layer in terms of those for the layer from which one starts the calculation. If the constants of integration for one layer are known, those for the next layer can, of course, always be obtained by solving a system of $(N+1)$ simultaneous algebraic equations, where N , assumed odd, is the order of approximation. It turns out, however, that solving this system of $(N+1)$ equations numerically is unnecessary, since their solution is always given by a simple explicit expression. In other words there exists a simple explicit expression for the inverse of the "fundamental matrix". This fact is already known for problems with plane symmetry (Davison 1956). The purpose of the present note is to show this for the case of spherically symmetric assemblies.

For the reader's convenience we first summarize, in Section 2, the main relevant formulae of the spherical harmonics method and recapitulate, in Section 3, the derivation of the inverse of the fundamental matrix for the plane case. The derivation of the inverse of the fundamental matrix for the spherical case is given in Section 4. Finally in Section 5 we illustrate the application of the formulae by considering the critical size problem.

For the sake of simplicity we restrict ourselves in what follows by the following assumptions:

- (A) Scattering is isotropic in the laboratory system of coordinates.
- (B) Gaps and layers of strongly absorbing material are treated in the same way as any other layer.
- (C) There are no sources.

¹Manuscript received September 10, 1956.

Contribution from the Computation Centre, McLennan Laboratory, University of Toronto, Toronto, Ontario.

- (D) The number of secondaries per collision is not equal to unity in any of the layers.

The modifications needed if any of these assumptions is violated are easily found. In so far as (C) and (D) are concerned, the modifications do not in any way weaken the results derived below. In particular if (D) is violated, the number of secondaries per collision, c , in any layer being unity, one has simply to carry out the analysis for $c \neq 1$ and pass to the limit with c tending to unity in the result.

2. THE BASIC FORMULAE OF THE SPHERICAL HARMONICS METHOD

In the P_N -approximation spherical harmonics method, in both the plane and the spherical case, the angular distribution can be expressed as

$$(2.1) \quad \psi(\mathbf{r}, \mu) = \frac{1}{4\pi} \sum_{n=0}^N (2n+1) \psi_n(\mathbf{r}) P_n(\mu),$$

$$(2.2) \quad \psi_n(\mathbf{r}) = \sum_{j=-\frac{1}{2}(N+1)}^{\frac{1}{2}(N+1)} \{M(\mathbf{r}/l, c)\}_n^j A_j$$

where, in the plane case, \mathbf{r} is to be replaced by the Cartesian coordinate x , μ is the cosine of the angle between the x -axis and the direction of neutron travel, and

$$(2.3) \quad \{M(\mathbf{r}/l, c)\}_n^j = \{M_{01}(x/l, c)\}_n^j = G_n(\nu_j, c) \exp(\nu_j x/l),$$

while, in the spherical case, \mathbf{r} is to be replaced by the distance r from the center of symmetry, μ is the cosine of the angle between the radius vector and the direction of neutron travel, and

$$(2.4) \quad \{M(\mathbf{r}/l, c)\}_n^j = \{M_{00}(r/l, c)\}_n^j = G_n(\nu_j, c) \sqrt{-2\nu_j/\pi r} K_{n+\frac{1}{2}}(-\nu_j r/l).$$

Throughout the above formulae the order of approximation N is assumed odd, $P_n(\mu)$ are Legendre polynomials, c is the number of secondaries per collision, l is the total mean free path, the A_j are constants of integration, and the functions $G_n(\nu, c)$ are defined by the recurrence relationships

$$(2.5) \quad (n+1) G_{n+1}(\nu, c) + \frac{2n+1-c\delta_{0n}}{\nu} G_n(\nu, c) + n G_{n-1}(\nu, c) = 0$$

(δ_{0n} being the Kronecker symbol) together with

$$(2.6) \quad G_0(\nu, c) = 1.$$

The ν_j are the roots of the equation

$$(2.7) \quad G_{N+1}(\nu_j, c) = 0.$$

These roots come in pairs: if $\nu = \nu_j$ is a root of (2.7), so is $\nu = -\nu_j$, and for $c \neq 1$ they are all different. They will be assumed to be numbered in accordance with the conventions

$$(2.8) \quad \nu_{-j} = -\nu_j, \quad \nu_{j+1}^2 > \nu_j^2$$

together with

$$(2.9) \quad \text{sign } \nu_j = \text{sign } j \text{ for } \nu_j^2 > 0.$$

Finally $K_t(z)$ is the modified Bessel function of the second kind; the Macdonald definition of these,

$$(2.10) \quad K_t(z) = \frac{1}{2}\pi \{I_{-t}(z) - I_t(z)\} \operatorname{cosec} t\pi,$$

being used. We shall have to use later the following properties of these functions (Whittaker and Watson 1950):

$$(2.11) \quad K_{t+1}(z) = 2tK_t(z)/z + K_{t-1}(z),$$

$$(2.12) \quad K_{-1}(z) = K_1(z) = \sqrt{\pi/2z} \exp(-z),$$

and

$$(2.13) \quad K_t(z) - \exp(\pi it)K_t(-z) = \pi i \exp(\pi it)I_t(z).$$

It also follows from the definitions of $G_n(\nu, c)$ that

$$(2.14) \quad G_n(-\nu, c) = (-1)^n G_n(\nu, c).$$

The A_j are to be chosen so that, as we pass from each layer into the next,

$$(2.15) \quad \psi_n(\mathbf{r}) \text{ is continuous } (n = 0, 1, \dots, N)$$

where $\psi_n(\mathbf{r})$ is interpreted as $\psi_{n, \text{pl}}(x)$ in the plane case and as $\psi_{n, \text{sph}}(r)$ in the spherical case.

When considering several layers at once we shall write c_k, l_k, ν_{jk} , and A_{jk} for the values of c, l, ν_j , and A_j in the k th layer and shall denote by $\mathbf{r}_k(x_k \text{ or } r_k)$ the value of $\mathbf{r}(x \text{ or } r)$ at the interface between the k th and the $(k+1)$ th layer. Combining (2.2) and (2.15) we readily see that where the A_{jk+1} are known, the values of A_{jk} are given as the solution of the system of equations

$$(2.16) \quad \sum_{j=\pm 1}^{\pm \frac{1}{2}(N+1)} \{M(\mathbf{r}_k/l_k, c_k)\}_n^j A_{jk} = \sum_{i=\pm 1}^{\pm \frac{1}{2}(N+1)} \{M(\mathbf{r}_k/l_{k+1}, c_{k+1})\}_n^i A_{i, k+1}$$

and the solution in question can be obtained at once, provided for our l and c we have constructed $\{M^{-1}(\mathbf{r}/l, c)\}_j^n$ such that

$$(2.17) \quad \sum_{n=0}^N \{M^{-1}(\mathbf{r}/l, c)\}_j^n \{M(\mathbf{r}/l, c)\}_n^i = \delta_{ij}.$$

This question will occupy us in the next two sections.

3. PLANE CASE

We start by considering the quantity

$$(3.1) \quad S_m = (m+1)[G_{m+1}(\nu_{ik+1}, c_{k+1})G_m(\nu_{jk}, c_k) - G_{m+1}(\nu_{jk}, c_k)G_m(\nu_{ik+1}, c_{k+1})].$$

Using the recurrence relationships (2.5) to eliminate the G_{m+1} we easily obtain, provided $m > 1$,

$$S_m = (1/\nu_{jk} - 1/\nu_{ik+1})(2m+1)G_m(\nu_{jk}, c_k)G_m(\nu_{ik+1}, c_{k+1}) + S_{m-1},$$

and repeated application of this result gives

$$S_m = (1/\nu_{jk} - 1/\nu_{ik+1}) \sum_{n=1}^m (2n+1) G_n(\nu_{jk}, c_k) G_n(\nu_{ik+1}, c_{k+1}) + S_0.$$

Putting $m = N$ in this, noting that by (2.7) $S_N = 0$, and substituting for S_0 from (3.1), with G_0 and G_1 given by (2.6) and (2.5), gives

$$(3.2) \quad \sum_{n=0}^N (2n+1-c_k\delta_{0n}) G_n(\nu_{jk}, c_k) G_n(\nu_{ik+1}, c_{k+1}) = \nu_{jk}(c_k - c_{k+1})/(\nu_{ik+1} - \nu_{jk}).$$

Recalling that under the assumption (D) all ν_{jk} for a given k are different, passing to the limit with c_{k+1} tending to c_k , and noting that ν_{ik+1} will then tend to ν_{ik} , we arrive at (on suppressing the subscript k)

$$(3.3) \quad \sum_{n=0}^N (2n+1-c\delta_{0n}) G_n(\nu_j, c) G_n(\nu_i, c) = -\nu_i \delta_{ij}/(d\nu_i/dc).$$

Comparing this identity with (2.3) and (2.7) we see at once that

$$(3.4) \quad \{M_{D1}^{-1}(x/l, c)\}_j^n = -(d\nu_j/dc)(2n+1-c\delta_{0n}) G_n(\nu_j, c) \exp(-\nu_j x/l)/\nu_j$$

so that the solution of (2.16) for the plane case is given by

$$A_{jk} = \sum_{i=-1}^{\pm \frac{1}{2}(N+1)} A_{ik+1} \sum_{n=0}^N \{M_{D1}^{-1}(x_k/l_k, c_k)\}_j^n \{M_{D1}(x_k/l_{k+1}, c_{k+1})\}_i^n$$

or, on using (3.2) to simplify the inner sum, by

$$(3.5) \quad A_{jk} = (c_k - c_{k+1})(d\nu_{jk}/dc_k) \exp(-\nu_{jk}x_k/l_k) \\ \times \sum_{i=-1}^{\pm \frac{1}{2}(N+1)} A_{ik+1} \exp(\nu_{ik+1}x_k/l)/(\nu_{jk} - \nu_{ik+1}).$$

We may note that (3.4) can be rewritten, on using (2.5) to eliminate the explicit appearance of $1/\nu_j$, as

$$(3.6) \quad \{M_{D1}^{-1}(x/l, c)\}_j^n = \{(n+1)G_{n+1}(\nu_j, c) + nG_{n-1}(\nu_j, c)\} \exp(-\nu_j x/l)(d\nu_j/dc).$$

4. THE SPHERICAL CASE

4.1 Proof of an Identity

Analogy with (3.6) suggests that in the spherical case $\{M_{sph}^{-1}(r/l, c)\}_j^n$ may be proportional, apart from some simple factors, to

$$[(n+1)G_{n+1}(\nu_j, c)K_{n+3/2}(\nu_j r/l) + nG_{n-1}(\nu_j, c)K_{n-1/2}(\nu_j r/l)](d\nu_j/dc).$$

In order to establish this result we shall consider an auxiliary quantity

$$(4.1) \quad T_0 = (2y/\pi) \sqrt{-\nu_{jk}\nu_{ik+1}} \sum_{n=1}^N (\tilde{G}_n \tilde{K}_{n+1} G_{n-1} K_{n-1} + G_n K_{n+1} \tilde{G}_{n-1} \tilde{K}_{n-1}) n$$

where we have put for brevity

$$(4.2) \quad G_n = G_n(\nu_{jk}, c_k), \quad \tilde{G}_n = G_n(\nu_{ik+1}, c_{k+1}), \\ K_{n+\frac{1}{2}} = K_{n+\frac{1}{2}}(-y\nu_{jk}), \quad \tilde{K}_{n+\frac{1}{2}} = K_{n+\frac{1}{2}}(y\nu_{ik+1}), \\ y = r_k/l_k.$$

We introduce also the further auxiliary quantities T_m ($m \geq 1$) defined as follows: T_m is obtained by replacing, in T_{m-1} , $K_{N-m+3/2}$ and $\tilde{K}_{N-m+3/2}$ by $K_{N-m-1/2}$ and $\tilde{K}_{N-m-1/2}$ respectively, while leaving all other factors in each term exactly as they were in T_{m-1} .

Let us assess now the actual numerical difference between T_m and T_{m-1} . Notice that $K_{N+1/2}$ and $\tilde{K}_{N+1/2}$ each appear only once in T_0 , namely in the term

with $n = N$; $K_{N-\frac{1}{2}}$ and $\bar{K}_{N-\frac{1}{2}}$ each appear twice in T_1 , namely in the terms with $n = N-1$ and $n = N$; $K_{N-\frac{3}{2}}$ and $\bar{K}_{N-\frac{3}{2}}$ each appear three times in T_2 , namely in the terms with $n = N-2$, $n = N-1$, and $n = N$; and so on. Notice also that, in T_0 , $K_{N+\frac{1}{2}}$, apart from other factors, is multiplied by $\bar{K}_{N-\frac{1}{2}}$, while $\bar{K}_{N+\frac{1}{2}}$ is multiplied by $K_{N-\frac{1}{2}}$; in T_1 , apart from other factors, $K_{N-\frac{1}{2}}$ is multiplied on each occasion by $\bar{K}_{N-\frac{3}{2}}$ while $\bar{K}_{N-\frac{1}{2}}$ is multiplied on each occasion by $K_{N-\frac{3}{2}}$, and so on. Thus we have

$$(4.3.1) \quad T_1 - T_0 = (\bar{K}_{N-\frac{3}{2}} - \bar{K}_{N+\frac{1}{2}}) K_{N-\frac{1}{2}} N G_{N-1} \bar{G}_N + \text{"adjoint terms"},$$

$$(4.3.2) \quad T_2 - T_1 = (\bar{K}_{N-\frac{5}{2}} - \bar{K}_{N-\frac{1}{2}}) K_{N-\frac{3}{2}} [N G_N + (N-1) G_{N-2}] \bar{G}_{N-1} + \text{"adjoint terms"},$$

$$(4.3.3) \quad T_3 - T_2 = (\bar{K}_{N-\frac{7}{2}} - \bar{K}_{N-\frac{3}{2}}) K_{N-\frac{5}{2}} \{N G_{N-1} \bar{G}_N + [(N-1) G_{N-1} + (N-2) G_{N-3}] \bar{G}_{N-2}\} + \text{"adjoint terms"},$$

and so on, where "adjoint terms" is understood on each occasion to mean the expression similar to that written out explicitly, but with the barred and non-barred quantities interchanged.

Recalling the abbreviations (4.2) and using the recurrence relationship (2.11) and (2.5) together with (2.7) one can readily see that the term written out explicitly in (4.3.1) is equal to

$$(2N-1) \bar{K}_{N-\frac{1}{2}} K_{N-\frac{1}{2}} (2N+1 - c_k \delta_{0N}) G_N \bar{G}_N / y \nu_{ik+1} \nu_{jk}$$

while the other term (the "adjoint term") gives

$$-(2N-1) K_{N-\frac{1}{2}} \bar{K}_{N-\frac{1}{2}} (2N+1 - c_{k+1} \delta_{0N}) \bar{G}_N G_N / y \nu_{jk} \nu_{ik+1}$$

so that

$$T_1 - T_0 = (2N-1) K_{N-\frac{1}{2}} \bar{K}_{N-\frac{1}{2}} (c_{k+1} - c_k) G_N \bar{G}_N \delta_{0N} / y \nu_{jk} \nu_{ik+1}.$$

Transforming in a similar manner the formulae (4.3.2), (4.3.3), etc. we obtain

$$T_2 - T_1 = (2N-3) K_{N-\frac{3}{2}} \bar{K}_{N-\frac{3}{2}} (c_{k+1} - c_k) G_{N-1} \bar{G}_{N-1} \delta_{0N-1} / y \nu_{jk} \nu_{ik+1},$$

$$T_3 - T_2 = (2N-5) K_{N-\frac{5}{2}} \bar{K}_{N-\frac{5}{2}} (c_{k+1} - c_k) (G_N \bar{G}_N \delta_{0N} + G_{N-2} \bar{G}_{N-2} \delta_{0N-2}) / y \nu_{jk} \nu_{ik+1},$$

$$T_4 - T_3 = (2N-7) K_{N-\frac{7}{2}} \bar{K}_{N-\frac{7}{2}} (c_{k+1} - c_k) (G_{N-1} \bar{G}_{N-1} \delta_{0N-1} + G_{N-3} \bar{G}_{N-3} \delta_{0N-3}) / y \nu_{jk} \nu_{ik+1},$$

and so on.

Examining these formulae one can readily see that $(T_{m+1} - T_m)$ vanishes for all $m < N$ and hence

$$(4.4) \quad T_0 = T_1 = \dots = T_N.$$

On the other hand it is evident from the construction of T_m that, of various $K_{n+\frac{1}{2}}$ and $\bar{K}_{n+\frac{1}{2}}$, T_N can involve only $K_{\frac{1}{2}}$, $K_{-\frac{1}{2}}$, $\bar{K}_{\frac{1}{2}}$, and $\bar{K}_{-\frac{1}{2}}$, so that, in view of (2.12),

$$\begin{aligned} T_N &= (2y/\pi) \sqrt{-\nu_{jk} \nu_{ik+1}} K_{\frac{1}{2}} \bar{K}_{\frac{1}{2}} \sum_{n=1}^N n (\bar{G}_n G_{n-1} + G_n \bar{G}_{n-1}) \\ &= \exp[y(\nu_{jk} - \nu_{ik+1})] \sum_{n=0}^N \bar{G}_n \{ (n+1) G_{n+1} + n G_{n-1} \}. \end{aligned}$$

Combining this with (4.4), recalling (4.2), and using (2.5) and (3.2), we can rewrite the last result as

$$(4.5) \quad T_0 = \exp[y(\nu_{jk} - \nu_{ik+1})](c_{k+1} - c_k)/(\nu_{ik+1} - \nu_{jk}),$$

or substituting for T_0 , etc., from (4.1) and (4.2), and slightly rearranging the resulting expression, we have

$$(4.6) \quad \sum_{n=0}^N G_n(\nu_{jk}, c_k) K_{n+\frac{1}{2}}(-r_k \nu_{jk}/l_k) \{ (n+1) G_{n+1}(\nu_{ik+1}, c_{k+1}) K_{n+\frac{3}{2}}(r_k \nu_{ik+1}/l_{k+1}) \\ + n G_{n-1}(\nu_{ik+1}, c_{k+1}) K_{n-\frac{1}{2}}(r_k \nu_{ik+1}/l_{k+1}) \} (2r_k/\pi) \sqrt{(-\nu_{jk} \nu_{ik+1}/l_k l_{k+1})} \\ = \exp\{r_k(\nu_{jk}/l_k - \nu_{ik+1}/l_{k+1})\} (c_{k+1} - c_k)/(\nu_{ik+1} - \nu_{jk}) \\ + \text{terms vanishing for } l_{k+1} = l_k.$$

4.2 The Final Inversion Formula

Passing in (4.6) to the limit with l_{k+1} and c_{k+1} tending to l_k and c_k respectively, suppressing the subscript k , and multiplying through by $d\nu_i/dc$ we get

$$(4.7) \quad (2r/\pi l) (d\nu_i/dc) \sqrt{-\nu_j \nu_i} \sum_{n=0}^N G_n(\nu_j, c) K_{n+\frac{1}{2}}(-\nu_j r/l) \\ \times \{ (n+1) G_{n+1}(\nu_i, c) K_{n+\frac{3}{2}}(\nu_i r/l) + n G_{n-1}(\nu_i, c) K_{n-\frac{1}{2}}(\nu_i r/l) \} = \delta_{ij},$$

while comparing this with (2.4) and (2.17) we see that

$$(4.8) \quad \{M_{\text{sph}}^{-1}(r/l, c)\}_j^n = (r/l)^2 (d\nu_j/dc) \sqrt{2l\nu_j/\pi r} \{ (n+1) G_{n+1}(\nu_j, c) K_{n+\frac{3}{2}}(\nu_j r/l) \\ + n G_{n-1}(\nu_j, c) K_{n-\frac{1}{2}}(\nu_j r/l) \}$$

and the solution of (2.16) for the spherical case is then given by

$$(4.9) \quad A_{jk} = (2r_k/\pi l_k) \sqrt{l_{k+1} \nu_{jk}/l_k} (d\nu_{jk}/dc_k) \sum_{i=\pm 1}^{\pm(N+1)} A_{ik+1} \sqrt{-\nu_{ik+1}} \\ \times \sum_{n=1}^N n \{ G_n(\nu_{jk}, c_k) K_{n+\frac{1}{2}}(\nu_{jk} r_k/l_k) G_{n-1}(\nu_{ik+1}, c_{k+1}) K_{n-\frac{1}{2}}(-\nu_{ik+1} r_k/l_{k+1}) \\ + G_{n-1}(\nu_{jk}, c_k) K_{n-\frac{1}{2}}(\nu_{jk} r_k/l_k) G_n(\nu_{ik+1}, c_{k+1}) K_{n+\frac{1}{2}}(-\nu_{ik+1} r_k/l_{k+1}) \}.$$

4.3 Miscellaneous Remarks

If l_{k+1} is different from l_k , no appreciable simplifications arise in (4.9). But if $l_{k+1} = l_k$, i.e. if the k th and the $(k+1)$ th media differ only in the number of secondaries per collision, their total mean free paths being the same, (4.6) shows that (4.9) reduces to

$$(4.10) \quad A_{jk} = (c_k - c_{k+1}) (d\nu_{jk}/dc_k) \exp(-\nu_{jk} r_k/l_k) \\ \times \sum_{i=\pm 1}^{\pm(N+1)} A_{ik+1} \exp(\nu_{ik+1} r_k/l_k)/(\nu_{jk} - \nu_{ik+1})$$

(spherical case with $l_{k+1} = l_k$) which is identical with the corresponding formula, (3.5), for the plane case.

Two remarks may be added in connection with this last result. Suppose the mean free path is the same throughout a spherically symmetrical system.

Then comparison of (4.10) with (3.5) shows that the A_{jk} (all j and k) for this system will be equal to those for the appropriately chosen plane case. Also comparing (2.3), (2.4), and (2.12) we see that

$$r\{M_{\text{sph}}(r/l, c)\}_0^j = \{M_{\text{pl}}(r/l, c)\}_0^j.$$

Then, by (2.2), we have

$$r\psi_{0,\text{sph}}(r) = \psi_{0,\text{pl}}(r)$$

provided the mean free path is the same throughout the system.

This result for the exact solution has been known for some time (Davison 1956). We have now shown that it also holds in any odd-order approximation in the spherical harmonics method. The other remark arising in connection with (4.10) is as follows. Let $M_{\text{pl}}(x/l, c)$, $M_{\text{pl}}^{-1}(x/l, c)$, $M_{\text{sph}}(r/l, c)$, and $M_{\text{sph}}^{-1}(r/l, c)$ be the matrices whose elements are given by $\{M_{\text{pl}}(x/l, c)\}_n^j$, $\{M_{\text{pl}}^{-1}(x/l, c)\}_j^n$, etc. Then the result of comparison of (4.10) with (3.5) can be expressed as

$$(4.11) \quad M_{\text{sph}}^{-1}(r_k/l_k, c_k) M_{\text{sph}}(r_k/l_k, c_{k+1}) = M_{\text{pl}}^{-1}(r_k/l_k, c_k) M_{\text{pl}}(r_k/l_k, c_{k+1})$$

for $l_k = l_{k+1}$

and this suggests that $M_{\text{sph}}(r/l, c)$ should be of the form

$$(4.12) \quad M_{\text{sph}}(r/l, c) = W(r/l) M_{\text{pl}}(r/l, c)$$

where $W(r/l)$ is a certain matrix whose elements depend on r/l only. The formula (4.12) can be proved directly but the proof is rather lengthy and we shall omit it.

5. CRITICAL SIZE PROBLEMS

To illustrate the application of the above formulae we derive below the determinantal equation for the critical radius of a sphere in a multilayer reflector. We start, for the sake of simplicity, with a single-layer reflector contiguous to the core and extending to infinity, and shall distinguish the quantities appertaining to the core and the reflector by the subscripts 1 and 2 respectively. Since the reflector extends to infinity, we should obviously take $c_2 \leq 1$ and then, with the assumption (D) and the convention (2.9), the condition that there should be no supply of neutrons from infinity can be expressed as

$$(5.1.1) \quad A_{j2} = 0 \text{ for } j > 0.$$

At the same time, using (2.2) and (2.4), one can readily see that the condition of regularity at $r = 0$ implies

$$(5.2) \quad A_{j1} + A_{-j1} = 0, \quad j = 1, 2, \dots, \frac{1}{2}(N+1).$$

Expressing here A_{j1} and A_{-j1} in terms of $\psi_{n,\text{sph}}(r)$ ($n = 0, 1, \dots, N$) by means of (4.8) and recalling (2.8), (2.14), and (2.13) we easily obtain

$$(5.3) \quad \sum_{n=0}^N \psi_{n,\text{sph}}(r) \{ (n+1)G_{n+1}(\nu_{i1}, c_1) I_{n+3/2}(r\nu_{i1}/l_1) \\ + nG_{n-1}(\nu_{i1}, c_1) I_{n-1/2}(r\nu_{i1}/l_1) \} = 0$$

(r in the core, $i = 1, 2, \dots, \frac{1}{2}(N+1)$).

Applying this at the interface between the core and the reflector, i.e. at $r = r_1$, say, where r_1 is the critical radius of the sphere, recalling (2.15), and using (2.2) and (2.4) for the reflector, together with (5.1.1), we easily obtain

$$\sum_{j < 0} A_{j2} \sqrt{-l_2 \nu_{j2}/r_1} \sum_{n=0}^N G_n(\nu_{j2}, c_2) K_{n+\frac{1}{2}}(-\nu_{j2} r_1/l_2) \\ \times \{ (n+1) G_{n+1}(\nu_{11}, c_1) I_{n+\frac{3}{2}}(r_1 \nu_{11}/l_1) + n G_{n-1}(\nu_{11}, c_1) I_{n-\frac{1}{2}}(r_1 \nu_{11}/l_1) \} = 0$$

or, which is the same,

$$\sum_{j > 0} A_{-j2} \sqrt{l_2 \nu_{j2}/r_1} \sum_{n=1}^N (-)^n n \{ G_n(\nu_{j2}, c_2) G_{n-1}(\nu_{11}, c_1) K_{n+\frac{1}{2}}(r_1 \nu_{j2}/l_2) I_{n-\frac{1}{2}}(r_1 \nu_{11}/l_1) \\ - G_{n-1}(\nu_{j2}, c_2) G_n(\nu_{11}, c_1) K_{n-\frac{1}{2}}(r_1 \nu_{j2}/l_2) I_{n+\frac{1}{2}}(r_1 \nu_{11}/l_1) \} = 0.$$

Eliminating between those equations the constants A_{-j2} we obtain the determinantal equation

$$(5.4) \quad \begin{vmatrix} X_{11} & X_{12} & \dots & X_{1\frac{1}{2}(N+1)} \\ X_{21} & X_{22} & \dots & X_{2\frac{1}{2}(N+1)} \\ \vdots & \vdots & \ddots & \vdots \\ X_{\frac{1}{2}(N+1)1} & X_{\frac{1}{2}(N+1)2} & \dots & X_{\frac{1}{2}(N+1)\frac{1}{2}(N+1)} \end{vmatrix} = 0$$

where

$$(5.5.1) \quad X_{ij} = \sum_{n=1}^N (-1)^n n \{ G_n(\nu_{j2}, c_2) G_{n-1}(\nu_{11}, c_1) K_{n+\frac{1}{2}}(r_1 \nu_{j2}/l_2) I_{n-\frac{1}{2}}(r_1 \nu_{11}/l_1) \\ - G_{n-1}(\nu_{j2}, c_2) G_n(\nu_{11}, c_1) K_{n-\frac{1}{2}}(r_1 \nu_{j2}/l_2) I_{n+\frac{1}{2}}(r_1 \nu_{11}/l_1) \}.$$

Suppose now we have a two-layer reflector, with the inner reflector contiguous to the core and the outer reflector, and the outer reflector extending to infinity. We shall distinguish the quantities appertaining to the core, the inner reflector, and the outer reflector by the subscripts 1, 2, and 3 respectively, so that (5.1.1) is now replaced by

$$(5.1.2) \quad A_{j3} = 0 \text{ for } j > 0.$$

We proceed exactly as above, except that, before substituting into (5.3), we should express $A_{j'2}$ in terms of A_{j3} by means of (4.10). In this manner we arrive at the determinantal equation of exactly the same form, (5.4), as before, except that the X_{ij} are now given by

$$(5.5.2) \quad X_{ij} = \sum_{j'=\pm 1}^{\pm \frac{1}{2}(N+1)} \left[\frac{d}{dc} (\nu_{j'}^2) \right]_{c=c_2} \\ \times \sum_{n'=1}^N n' \{ G_{n'}(\nu_{j3}, c_3) G_{n'-1}(\nu_{j'2}, c_2) K_{n'+\frac{1}{2}}(r_2 \nu_{j3}/l_2) K_{n'-\frac{1}{2}}(-r_2 \nu_{j'2}/l_2) \\ + G_{n'-1}(\nu_{j3}, c_3) G_{n'}(\nu_{j'2}, c_2) K_{n'-\frac{1}{2}}(r_2 \nu_{j3}/l_2) K_{n'+\frac{1}{2}}(-r_2 \nu_{j'2}/l_2) \} \\ \times \sum_{n=1}^N (-1)^n n \{ G_n(\nu_{j'2}, c_2) G_{n-1}(\nu_{11}, c_1) K_{n+\frac{1}{2}}(r_1 \nu_{j'2}/l_2) I_{n+\frac{1}{2}}(r_1 \nu_{11}/l_1) \\ - G_{n-1}(\nu_{j'2}, c_2) G_n(\nu_{11}, c_1) K_{n-\frac{1}{2}}(r_1 \nu_{j'2}/l_2) I_{n-\frac{1}{2}}(r_1 \nu_{11}/l_1) \}$$

and similarly for any larger number of layers. If any two adjacent layers differ only by the value of c , the values of l being equal, the formula (5.5.3) can be easily simplified using (4.6).

We have been assuming that the outermost layer of the reflector extends to infinity, but this is no restriction since any finite system can be always regarded as embedded in an infinite purely absorbing medium. The assumption (D) can always be eliminated, as pointed out in the Introduction, while the assumption (C) will be automatically satisfied in critical size problems. Thus, provided the assumptions (A) and (B) are satisfied,² the ultimate determinantal equation for the critical radius is given by a determinant of the order $\frac{1}{2}(N+1)$ (rather than of the order $(N+1)$ which one might have expected at first sight) irrespective of the number of the layers. It may also be noted that the quantities (dv_r/dc) will have to be known only for the intermediate layers, but not for the core, nor for the outermost layer extending to infinity.

REFERENCES

- DAVISON, B. 1956. Neutron transport theory (Oxford University Press, London).
MARK, C. 1944. The spherical harmonics method, I, Chalk River Report CRT-340.
— 1945. The spherical harmonics method, II, Chalk River Report CRT-338.
WHITTAKER, E. T. and WATSON, G. N. 1950. A course of modern analysis (Cambridge University Press, Cambridge).

²It should be pointed out with respect to the assumption (B) that though in principle we can always satisfy it, in practice this may be undesirable, since treating gaps and strongly absorbing layers on the same footing as any other layer may in certain cases have an adverse effect upon the convergence of the spherical harmonics method (Davison 1956, pp. 153-156 and 135-137).

THE EMISSION SPECTRUM OF AIF IN THE VACUUM ULTRAVIOLET¹

S. M. NAUDÉ AND T. J. HUGO

ABSTRACT

Two vacuum ultraviolet band systems of aluminum monofluoride, the $B^1\Sigma^+-X^1\Sigma^+$ and $C^1\Sigma^+-X^1\Sigma^+$ systems, are described. The rotational analyses of a few bands in each system are given and the rotational and vibrational constants of the $X^1\Sigma^+$ and $B^1\Sigma^+$ electronic states are determined. Accurate T_e -values for the $A^1\Pi$, $B^1\Sigma^+$, $C^1\Sigma^+$, and $D^1\Delta$ states are given.

A. INTRODUCTION

Recent studies (Rowlinson and Barrow 1953; Dodsworth and Barrow 1955; Naudé and Hugo 1953, 1954; Barrow and Rowlinson 1954) of the spectrum of the aluminum monofluoride molecule have shown the existence of a number of singlet and triplet electronic states. These studies, both in emission and absorption, covered the wavelength region from 1250 Å to 8800 Å, but, in spite of the fact that a number of band systems involving transitions to or from the ground state were observed, no rotational analysis of the ground state has as yet been made. This may be ascribed to the fact that the only band system involving the ground state which lies in a region easily accessible to high dispersion instruments is the $A^1\Pi-X^1\Sigma^+$ system at 43950 cm⁻¹. The vibrational structure of this system is, however, of such a nature that even under high dispersion the rotational structure is not resolved because of the strong overlapping of successive bands in the sequences. The other systems involving the ground state all lie in the vacuum ultraviolet where only low dispersion data were available.

The opportunity was generously offered to one of us to obtain high dispersion spectrograms of the region below 2000 Å on the 3-meter vacuum spectrograph of the National Research Council of Canada in Ottawa. In its fourth order this instrument resolved the fine structure of some of the bands of the $B^1\Sigma^+-X^1\Sigma^+$ and $C^1\Sigma^+-X^1\Sigma^+$ systems sufficiently well to permit rotational analyses.

B. EXPERIMENTAL

The AIF spectrum was excited according to the method previously described (Naudé and Hugo 1953) and photographed on the 3-meter vacuum spectrograph described by Brix and Herzberg (1954). The reciprocal dispersion was 0.63 Å/mm. Overlapping orders were eliminated by the use of a LiF prism in front of the spectrograph slit (Brix and Herzberg 1954). Wavelength standards were furnished by second order iron lines. The wavelengths of the iron lines were converted to vacuum wave numbers by means of Kayser's "Tabelle der Schwingungszahlen" as corrected by Edlén (1953).

¹Manuscript received October 19, 1956.

Contribution from the National Physical Research Laboratory, Council for Scientific and Industrial Research, Pretoria, Union of South Africa.

C. THE $B^1\Sigma^+-X^1\Sigma^+$ SYSTEM

This system was first observed by Barrow and Rowlinson (1954) in their study of the absorption spectrum of AlF in the Schumann region. It forms the strongest absorption feature and Barrow and Rowlinson were able to observe five sequences, viz. the 2-0, 1-0, 0-0, 0-1, and 0-2 sequences.

The system is emitted with high intensity from the hollow cathode discharge. The over-all intensity is comparable to that of the $C^1\Sigma^+-X^1\Sigma^+$ system which is possibly the strongest emission feature in the Schumann region. In the emission spectrum six sequences of single-headed bands degraded to shorter wavelengths were observed. The band heads with their estimated intensities are listed in Table I.

TABLE I
BAND HEADS AND ORIGINS OF THE $B^1\Sigma^+-X^1\Sigma^+$ SYSTEM OF AlF.

Band $v'-v''$	Intensity	Band head in cm^{-1}	Band origin in cm^{-1}		
			Observed	Calculated from band head	Calculated from Equation (1)
0-3	1	51925.5		51933.1	51932.9
1-4	2	52012.7		52020.2	52020.2
2-5	1	094.6		101.9	101.4
3-6	0	170.5		177.7	176.6
0-2	5	697.9	52706.7 _s	706.6	706.7
1-3	4	775.8	784.5 _s	784.3	784.5
2-4	3	848.6		857.0	856.4
3-5	2	915.2		923.4	922.1
4-6	1	976.0		984.0	981.4
0-1	5	53479.8	53489.9 _s	53490.0	53489.9
1-2	3	547.2		557.1	558.3
2-3	2	611.6		621.3	620.7
3-4	0	669.5		679.0	677.1
0-0	4	54270.5	54282.4 _s	54282.6	54282.4
1-1	2	329.5		341.4	341.4
2-2	1	383.1		394.7	394.5
1-0	4	55118.9		55132.0	55134.0
2-1	2	162.9		177.3	177.6
3-2	1	201.2		215.2	215.2
4-3	1	233.7		247.4	246.2
5-4	1	258.6		272.0	270.6
2-0	2	951.0		969.7	970.2
3-1	2	979.6		997.8	998.3
4-2	2	56001.8		56019.6	56020.0
5-3	1	014.6		031.9	034.9

With the available resolution only the 0-0, 0-1, 0-2, and 1-3 bands could be analyzed, because the other bands are either too weak or too strongly overlapped to permit a rotational analysis. The origins of all the bands were, however, determined from the observed band heads and either the observed or calculated B_v -values using the equation

$$\nu_{\text{head}} - \nu_0 = -(B_v' + B_v'')^2 / 4(B_v' - B_v'').$$

The values for the band origins determined in this way are also listed in Table I together with the values determined directly for the analyzed bands. These values can be represented by the equation

$$(1) \quad \nu_0 = 54250.8_1 + 866.6_0(v' + \frac{1}{2}) - 7.4_6(v' + \frac{1}{2})^2 \\ - 0.04_5(v' + \frac{1}{2})^3 - 801.9_6(v'' + \frac{1}{2}) + 4.7_0(v'' + \frac{1}{2})^2.$$

The ν_0 values calculated from this equation are included in Table I for comparison.

The wave numbers of the 0-0, 0-1, 0-2, and 1-3 bands are given in Table II.

TABLE II
WAVE NUMBERS OF THE LINES IN THE $B^1\Sigma^+ - X^1\Sigma^+$ SYSTEM OF AIF

J	0-0 Band $\lambda_{head} = 1842.6 \text{ \AA}$		0-1 Band $\lambda_{head} = 1809.9 \text{ \AA}$		0-2 Band $\lambda_{head} = 1897.6 \text{ \AA}$		1-3 Band $\lambda_{head} = 1894.8 \text{ \AA}$	
	R(J)	P(J)	R(J)	P(J)	R(J)	P(J)	R(J)	P(J)
0	54284.06*		53490.83*					
1	285.26*	54281.75*	492.02*	53488.55*	52708.88*	52705.24*		
2	286.56*	280.68*	493.29*	487.54*	710.16*	704.27*		
3	287.98	279.65*	494.68*	486.57*	711.61*	703.36*		
4	288.85	278.71*	496.12*	485.68*	713.06*	702.55*		
5	290.13	277.77*	497.55*	484.86*	714.59*	701.72*	52702.46*	
6	291.67	276.92*	499.12*	484.10*	716.16*	701.17*	794.13*	
7	293.20	276.03*	500.73*	483.37*	717.84*		795.63	
8	294.77	275.31*	502.42*	482.69*	719.60*		797.37	
9	296.44	274.46*	504.13*		721.43		799.18	
10	298.10		505.90*		723.33		801.07	
11	299.85		507.77*		725.30		802.92	
12	301.67		509.71*		727.31		804.96	
13	303.50		511.69*		729.41		807.02	
14	305.38		513.74*		731.60		809.16	
15	307.37		515.87*		733.86		811.38	
16	309.38		518.04*		736.18		813.75*	
17	311.42		520.23*		738.58		816.04	
18	313.55		522.56*		741.06		818.47*	
19	315.73		524.93*		743.62		820.96	
20	317.92		527.35*		746.23		823.55	
21	320.19		529.82*		748.91*		826.19*	
22	322.57		532.42*		751.69*		828.94	
23	324.96		535.01*		754.53*		831.69	
24	327.34		537.70*		757.42*	701.17*	834.54	52778.64*
25	—		540.69*		760.41*	701.72*	837.48	779.33*
26	—		543.49*		763.44*	702.55*	840.40	780.00*
27	334.99		546.44*	482.69*	766.55*	703.36*	843.55	780.86*
28	337.62		—	483.37*	769.72*	704.27*	846.67	781.75
29	340.20		—	484.10*	772.98*	705.24*	—	782.67*
30	343.13		555.41*	484.86*	—	706.31*	853.10*	783.63*
31	345.97		558.60*	485.68*	780.00*	707.42*	856.52*	784.82
32	348.71		—	486.57*	783.17*	708.61*	859.98	785.99
33	351.68	274.40*	565.17*	487.54*	786.80*	709.93*	863.45*	787.18*
34	354.58*	275.31*	567.95*	488.55*	790.50*	711.28*	867.02	788.53
35	357.70*	276.03*	571.29*	489.68*	794.41*	712.74*	870.68	789.88
36	360.62*	276.92*	574.72*	490.83*	797.98*	714.23*	874.38	791.34
37	363.98*	277.77*	578.14*	492.02*	801.75*	715.81*	878.30*	792.90*
38	367.00	278.71*	581.77	493.29*	805.70*	717.47*	882.00*	794.41*
39	370.12	279.65*	585.36*	494.68*	809.83*	719.19*	885.98*	796.15
40	373.50	280.68*	589.07*	496.12*	813.75*	721.00	889.92	797.98*
41	376.91	281.75*	592.79*	497.55*	818.05*	722.89	894.08*	799.70
42	380.19*	282.88*	596.55*	499.12*	822.27*	724.85	898.11*	801.75*
43	—	284.06*	600.31*	500.73*	826.48*	726.87	902.28	803.52
44	387.15*	285.26*	604.23	502.42*	830.94	728.96	906.54	805.70*
45	390.65*	286.56*	608.24*	504.13*	835.32*	731.14	910.88*	807.71
46	394.48*	287.98	—	505.90*	839.83	733.42	915.24*	809.83*
47	398.08*	289.39	616.55	507.77*	844.43*	735.75	919.75*	812.16
48	401.68	290.82	620.73*	509.71*	—	738.15	924.21*	814.43
49	405.50	292.28	624.84*	511.69*	853.80*	740.60	929.00	816.87
50	—	293.84	629.24*	513.74*	858.57*	743.16	933.69*	819.36
51	413.09	295.46	633.59	515.87*	863.45*	745.79	—	821.89*
52	416.99	297.17	637.90*	518.04*	868.45*	748.46*	—	824.51
53	421.16*	298.87	642.40	520.23*	873.47*	751.20	—	827.20
54	425.05*	290.60	647.11	522.56*	878.30*	754.13*	—	829.97
55	429.13	302.50	651.41*	524.93*	883.77*	756.99*	—	832.77
56	433.25*	304.41	656.34	527.35*	888.86	760.06*	—	835.57*
57	437.37	306.30	661.09	529.82*	894.08*	763.14*	—	838.65
58	441.69	308.30	665.94*	532.42*	899.56	766.25*	—	841.70
59	445.97	310.41	670.79*	535.01*	904.95	769.51*	—	844.73*
60	450.30	312.52	—	537.70*	910.55*	772.98*	—	848.06
61	454.05	314.63						
62	459.10	316.87						
63	463.57	319.23						
64		321.54						
65		323.90						
66		326.39						
67		328.81						

*Lines marked with an asterisk could not be measured accurately.

The B_v and ν_0 values for these bands were determined graphically from the equation

$$R(J-1) + P(J) = 2\nu_0 + 2(B_v' - B_v'')J^2 - 2(D_v' - D_v'')J^2(J^2 + 1).$$

It was found that, within the present accuracy, the term in $(D_v' - D_v'')$ could be neglected for all four bands, i.e. $D_v' = D_v'' = 9.7 \times 10^{-7}$ (Naudé and Hugo 1954). In the case of the 0-0, 0-1, and 0-2 bands the accurate B_0' value obtained from the 0-0 band of the $F^1\Pi - B^1\Sigma^+$ system was used to determine B_v'' . In the case of the 1-3 band the B'' value was obtained from the 1-3 $C^1\Sigma^+ - X^1\Sigma^+$ band where the B_1' value is known accurately from the $C^1\Sigma^+ - A^1\Pi$ system. The B_v values for the $X^1\Sigma^+$ and $B^1\Sigma^+$ states as obtained from the $B^1\Sigma^+ - X^1\Sigma^+$ and $C^1\Sigma^+ - X^1\Sigma^+$ systems are given in Table III. The listed B_0 value for $X^1\Sigma^+$

TABLE III
OBSERVED AND CALCULATED B_v -VALUES OF THE $X^1\Sigma^+$ AND $B^1\Sigma^+$ STATES OF AIF

v	$X^1\Sigma^+$ state		$B^1\Sigma^+$ state	
	B_v in cm^{-1} (observed)	B_v in cm^{-1} (calculated)	B_v in cm^{-1} (observed)	B_v in cm^{-1} (calculated)
0	$0.549_0 \pm 0.0001$	0.549_{87}	$0.575_{90} \pm 0.00005$	0.575_{98}
1	$0.544_2 \pm 0.0009$	0.545_{03}	$0.571_{27} \pm 0.0001$	0.571_{27}
2	$0.540_3 \pm 0.0001$	0.540_{20}		
3	$0.535_4 \pm 0.0001$	0.535_{37}		
4	$0.530_5 \pm 0.0001$	0.530_{54}		

is the average value from the two band systems. The B_v values of the $X^1\Sigma^+$ and $B^1\Sigma^+$ states can be represented respectively by the equations

$$B_v = 0.552_{28} - 0.0048_3(v + \frac{1}{2})$$

and

$$B_v = 0.578_{34} - 0.004_{71}(v + \frac{1}{2}).$$

The values calculated from these equations are also shown in Table III.

D. THE $C^1\Sigma^+ - X^1\Sigma^+$ SYSTEM

This system was first observed in absorption by Barrow and Rowlinson (1954). In absorption the system is very weak but quite strong in emission

TABLE IV
BAND HEADS AND ORIGINS OF THE $C^1\Sigma^+ - X^1\Sigma^+$ SYSTEM OF AIF

Band $v'-v''$	Intensity	Band head in cm^{-1}	Band origin in cm^{-1}		
			Observed	Calculated from band head	Calculated from Equation (2)
1-4	2	55563.8	55569.6 ₀	55569.7	55570.5
2-5	0	726.3		732.1	733.2
0-2	3	56173.2		56179.9	56180.0
1-3	3	327.6	56334.0 ₂	334.1	334.3
2-4	2	481.3		487.7	487.6
0-1	5	955.4		962.9	963.1
1-2	4	57100.5		57107.8	57108.1
2-3	2	244.7		251.9	252.0
0-0	5	746.9	57755.6 ₄	755.4	755.6
1-1	2	882.8		891.1	891.1
1-0	3	58674.0		58683.6	58683.7
2-1	2	799.3		808.7	808.8
3-2	0	923.5		932.6	932.9

from the hollow cathode discharge. The observed emission spectrum consists of the 1-0, 0-0, 0-1, 0-2, and 0-3 sequences. The bands are single-headed and degraded to shorter wavelengths. The band heads with their estimated intensities are listed in Table IV. The 0-3 band is masked by the stronger bands of the 1-0 sequence of the $B^1\Sigma^+ - X^1\Sigma^+$ system.

The 0-0, 1-3, and 1-4 bands were analyzed and the wave numbers of the lines are given in Table V. The rotational constants and origins of these bands were determined from the $R(J-1) + P(J)$ data by using the accurate B_v' values of the $C^1\Sigma^+ - A^1\Pi$ system (Naudé and Hugo 1953). The term in

TABLE V
WAVE NUMBERS OF THE LINES IN THE $C^1\Sigma^+ - X^1\Sigma^+$ SYSTEM OF AIF

<i>J</i>	0-0 Band $\lambda_{\text{head}} = 1731.7 \text{ \AA}$		1-3 Band $\lambda_{\text{head}} = 1795.3 \text{ \AA}$		1-4 Band $\lambda_{\text{head}} = 1799.7 \text{ \AA}$	
	<i>R</i> (<i>J</i>)	<i>P</i> (<i>J</i>)	<i>R</i> (<i>J</i>)	<i>P</i> (<i>J</i>)	<i>R</i> (<i>J</i>)	<i>P</i> (<i>J</i>)
0	57750.82*				55570.74*	
1	758.07*	57754.52*			572.00*	55568.56*
2	759.40*	753.48*			573.37*	567.58*
3	760.82*	752.49*	56339.33*		574.86*	566.65*
4	762.28*	751.69*	340.96		576.49*	565.95*
5	763.88*	750.86*	342.54		578.18*	565.39*
6	765.47*		344.27		580.00*	564.81*
7	767.19*		346.12		581.86*	
8	769.01*		348.14		583.92*	
9	770.91*		350.10		586.01*	
10	772.83*		352.24		588.22*	
11	774.84*		354.51		590.45*	
12	776.94*		356.76		593.04*	
13	778.92*		359.17		595.62*	
14	781.18*		361.64		598.20*	
15	783.46*		364.26		600.90*	564.81*
16	785.82*		366.97*		603.86*	565.39*
17	788.28*		369.77		606.77*	565.95*
18	790.82*		372.70	56329.59*	609.88*	566.65*
19	793.42		375.63	330.17*	613.04*	567.58*
20	796.07		378.70	330.97	616.31*	568.50*
21	798.79		381.83	331.82	619.75*	569.55
22	801.68		385.10*	332.82*	623.23	570.74*
23	804.56		388.50*	333.82	626.80	572.00*
24	807.61		391.78*	334.93	630.45*	573.37*
25	810.08	750.86*	395.38*	336.18	634.19*	574.86*
26	813.76	751.69*	399.04*	337.48	638.14*	576.49*
27	816.97	752.49*	402.83	338.91	642.03*	578.18*
28	820.24	753.48*	406.09	340.48	646.20*	580.00*
29	823.64	754.52*	410.62	342.04	650.45	581.86*
30	827.07	755.60	414.66	343.75	654.78	583.92*
31	830.59	756.82*	418.90	345.65	659.28	586.01*
32	834.16	758.07*	423.10	347.55	663.81	588.22*
33	837.81	759.40*	427.46	349.51	668.38	590.45*
34	841.57	760.82*	431.89	351.66	673.15	593.04*
35	845.39	762.28*	436.41*	353.89	677.96	595.62*
36	849.33	763.88*	441.08*	356.20	682.96	598.20*
37	853.26	765.47*	445.68*	358.62	688.02	600.90*
38	857.30	767.19*	450.46	361.16	693.13	603.86*
39	861.49	769.01*	455.39	363.76	698.49	606.77*
40	865.67	770.91*	460.32	366.45	703.85	609.88*
41	869.94	772.83*	465.44	369.18	709.43	613.04*
42	874.32	774.84*	470.66	372.07	714.94	616.31*
43	878.73	776.94*	475.90	375.07	720.66	619.75*
44	—	779.26*		378.22		
45	887.79	781.48*		381.34		
46	892.47	783.78*				
47	897.24	786.20*				
48	902.09	788.77*				
49	907.05	791.39*				
50	911.99	794.08				
51	916.97	797.77				
52	922.16	799.65				
53	927.34	802.57				
54	932.65	805.58				
55	937.97	808.65				
56	943.47	811.80				
57		815.08				
58		818.37				

*Lines marked with an asterisk could not be measured accurately.

$(D_v' - D_v'')$ could be neglected again for all the bands. This gives $D_v' = D_v'' = 9.6 \times 10^{-7}$ (Naudé and Hugo 1953). The B_v'' and B_v' values are given in Table III and the ν_0 values in Table IV. As for the $B^1\Sigma^+ - X^1\Sigma^+$ system the ν_0 values of all the observed bands determined from the band head data and B_v values are compared in Table IV with the values calculated from the equation representing the band origins, viz.

$$(2) \quad \nu_0 = 57687.5_4 + 938.3_9(v' + \frac{1}{2}) - 5.18(v' + \frac{1}{2})^2 - 801.9_6(v'' + \frac{1}{2}) + 4.7_0(v'' + \frac{1}{2})^2.$$

E. DISCUSSION

The rotational and vibrational constants of the $X^1\Sigma^+$ and $B^1\Sigma^+$ electronic states obtained in this study are summarized in Table VI.

TABLE VI
VIBRATIONAL AND ROTATIONAL CONSTANTS OF THE
 $X^1\Sigma^+$ AND $B^1\Sigma^+$ STATES OF AIF

Constant	$X^1\Sigma^+$	$B^1\Sigma^+$
B_v (cm ⁻¹)	$0.552_{28} \pm 0.0001$	$0.578_{84} \pm 0.0002$
α_v (cm ⁻¹)	$0.004_{83} \pm 0.0001$	$0.004_{71} \pm 0.0001$
D (cm ⁻¹)	9.7×10^{-7}	9.6×10^{-7}
I_v (g-cm. ²)	$50.66_8 \times 10^{-40}$	$48.38_8 \times 10^{-40}$
r_v (cm.)	$1.654_7 \times 10^{-8}$	$1.617_0 \times 10^{-8}$
ν_{00} (cm ⁻¹)	—	54282.4_6
T_v (cm ⁻¹)	0	54250.8_1
ω_v (cm ⁻¹)	801.9_6	866.6_0
$\omega_v x_v$ (cm ⁻¹)	4.7_0	7.4_5
$\omega_v y_v$ (cm ⁻¹)	—	0.04_5

It is interesting to compare the wave number interval between $\nu_{00}C^1\Sigma^+$ and $\nu_{00}B^1\Sigma^+$ as obtained from the vacuum ultraviolet bands with that obtained from the visible and infrared systems $F^1\Pi - A^1\Pi$, $C^1\Sigma - A^1\Pi$, and $F^1\Pi - B^1\Sigma$, for this should give an indication of the absolute accuracy of measurement attained in the vacuum ultraviolet. These two determinations give respectively the values 3473.1_9 cm⁻¹ and 3473.2_4 cm⁻¹. In the determination of the last value the Edlén corrections to the Kayser table were taken into account. From these values it seems probable that an absolute accuracy of 0.1 cm⁻¹ is attained in the vacuum ultraviolet. The relative accuracy is appreciably higher.

From the data presented here and those previously published (Naudé and Hugo 1953, 1954) accurate T_v values can be assigned to the $A^1\Pi$, $B^1\Sigma$, $C^1\Sigma$, and $D^1\Delta$ electronic states. These values are respectively: 43947.9_9 , 54282.4_6 , 57687.5_4 , 61227.0_0 .

ACKNOWLEDGMENTS

The authors would like to thank Dr. Gerhard Herzberg, Director of the Division of Pure Physics, National Research Council of Canada, for the use of the vacuum spectrograph and Mr. J. Shoosmith and Dr. P. K. Carroll for their help in the experimental work.

One of us (T.J.H.) is indebted to the National Research Council for a Post-doctorate Fellowship which made this work possible.

This paper is published with the permission of the South African Council for Scientific and Industrial Research.

REFERENCES

- BARROW, R. F. and ROWLINSON, H. C. 1954. Proc. Roy. Soc. (London), A, **224**, 134.
BRIX, P. and HERZBERG, G. 1954. Can. J. Phys. **32**, 110.
DODSWORTH, P. G. and BARROW, R. F. 1955. Proc. Phys. Soc. A, **68**, 824.
EDLÉN, B. 1953. J. Opt. Soc. Amer. **43**, 339.
NAUDÉ, S. M. and HUGO, T. J. 1953. Can. J. Phys. **31**, 1106.
——— 1954. Can. J. Phys. **32**, 246.
ROWLINSON, H. C. and BARROW, R. F. 1953. Proc. Phys. Soc. A, **66**, 437.

THE SPECTRUM OF SILICON HYDRIDE¹

A. E. DOUGLAS

ABSTRACT

The 0-0, 1-0, 2-1, and 2-2 bands of the $^2\Delta-^2\Pi$ band system of SiH have been photographed under high dispersion and analyzed. The vibrational and rotational constants have been determined and the dissociation energy has been found to be 3.19 ± 0.25 ev. A list of SiH lines which may occur as interstellar absorption lines is given.

INTRODUCTION

A band system due to a $^2\Delta-^2\Pi$ transition of silicon hydride has been known for many years and has been photographed under high resolution by Jackson (1930) and by Rochester (1936). The analysis of the 0-0 band has been given by Jackson and somewhat modified by Mulliken (1931). Rochester has given a detailed analysis of the 1-1 band of SiH and the 0-0 and 1-1 band of SiD. Recently during an investigation of the Si₂ molecule (Douglas 1955), it was found that SiH bands were emitted strongly from the same discharge tube. Spectra from this source which were photographed at a dispersion of 0.35 Å/mm. showed the 0-0, 1-1, 2-2, 1-0, and 2-1 bands of the $^2\Delta-^2\Pi$ band system. No other band systems which could be attributed to SiH were found. Because the SiH molecule is one of considerable astrophysical and chemical interest, it was considered desirable to measure and analyze these new bands of SiH. This paper gives the measured wave numbers of the lines and the molecular constants derived from them.

RESULTS

The 0-0, 1-0, 2-1, and 2-2 bands have been measured and analyzed. This analysis shows that the analysis of the 0-0 band given by Jackson is essentially correct but, because of lack of resolution on his plates, a number of lines of low J value were incorrectly assigned. The measurements and the analysis of the 1-1 band given by Rochester were found to be quite satisfactory and this band was not remeasured. The wave numbers of the lines are given in Table I.

The analysis of the bands was quite straightforward and all of the necessary equations have been given by Rochester. The constants which have been determined are given in Table II. For the $^2\Pi$ state the small term γ in the spin splitting has been neglected. For the $^2\Delta$ state, the constants A and γ were found to be 3.83 and 0.9 cm⁻¹ respectively; values which are very close to those given by Rochester. The experimentally observed Λ doubling cannot be represented accurately by the approximate equations of Mulliken and Christy (1931) and no improvement can be made on the Λ splitting constants p and q given by Rochester.

¹Manuscript received September 27, 1956.

Contribution from the Division of Pure Physics, National Research Council, Ottawa, Canada.

Issued as N.R.C. No. 4168.

TABLE I
WAVE NUMBERS OF THE LINES OF THE SiH BANDS

<i>J</i>	<i>P₁(J)</i>	<i>Q₁(J)</i>	<i>R₁(J)</i>	<i>P₂(J)</i>	<i>Q₂(J)</i>	<i>R₂(J)</i>	<i>P₃(J)</i>	<i>Q₃(J)</i>	<i>R₃(J)</i>	<i>P₄(J)</i>	<i>Q₄(J)</i>	<i>R₄(J)</i>
†			24252.99			24161.49			24122.47			24283.02
1‡		24218.36	253.18 261.22			181.20		24063.45			24247.04	292.02
2‡		218.10 212.65	261.48 270.19			199.66		072.13	126.59		24212.32	292.22 315.83
3‡	24169.49	212.32 207.59	270.51 279.65	24038.04	24126.77*	217.00	24002.43	060.28	130.00*		208.56	297.39 316.10 339.83
4‡	169.16 149.67	202.95 202.95	280.01 289.47	057.00	130.00*	217.12 233.37	002.31 23975.32	047.78	132.73		208.22 204.32	297.25 340.15 364.03
5‡	130.50	202.57 198.61	289.85 299.47	044.76	131.95 133.71*	233.59 248.86	975.11 947.43	047.56	134.67		203.95 200.14	364.40 388.37
6‡	111.69 111.31 093.15	198.23 194.41	299.85 309.58	†	†	†	†	†	134.47 135.85	199.68*	287.33 297.13	388.76 413.10 437.06
7‡	092.82 074.79	194.07 190.29	309.91 319.65	†	133.71*	263.99 277.40	919.27 891.31	†	135.57 136.46	195.72 192.07	297.50 307.35	437.39 461.19
8‡	074.51 056.52	190.01 186.14	319.92 329.60	004.02 23990.00	133.71*	278.00 290.50	890.71 862.51	006.24	135.85		307.69 317.51	461.46 486.08
9‡	056.31	185.94	329.81	989.23	132.91	291.28	861.73	23992.15	135.85		187.80 183.90	485.27
10‡	†	181.85	339.40	974.89	132.50	302.81	833.37	977.00	134.47		327.69	508.65*
11‡	†	177.49	348.80	973.93	131.51	303.78	832.39	976.04	133.71*		337.31*	531.67
12‡	001.71	172.98	357.75	959.31	130.62	314.37	803.87	961.40	132.60		346.71	
13‡	001.56 23983.26	172.83 168.15	357.87 366.21	958.14 926.77	129.48 125.07	315.54 325.11	802.70 774.08	960.23 945.35	131.51		355.72*	
14‡	982.68 964.04	167.86 162.98	366.50 374.12	941.88 908.78	126.77* 123.44	326.50 336.67	772.67 742.34	943.96 911.88				
15‡	964.18 945.77	162.52 157.39	374.39 382.28	907.89 892.28	119.46 116.80	344.08	711.72	909.99 894.42				
16‡	945.15 926.66	156.74 151.28	381.40	890.12 874.31	114.74		892.28					
17‡	925.81	150.45 144.60		871.85 855.66								
				852.92								

TABLE I (continued)
WAVE NUMBERS OF THE LINES OF THE SiH BANDS (continued)

TABLE 1 (concluded)
WAVE NUMBERS OF THE LINES OF THE SiH BANDS (concluded)

<i>J</i>	<i>P₁(J)</i>	<i>Q₁(J)</i>	<i>R₁(J)</i>	<i>P₂(J)</i>	<i>Q₂(J)</i>	<i>R₂(J)</i>	<i>P₃(J)</i>	<i>Q₃(J)</i>	<i>R₃(J)</i>	<i>P₄(J)</i>	<i>Q₄(J)</i>	<i>R₄(J)</i>
2-2 Band												
1			23504.85									23500.37
11		23472.10	505.01			23407.22					23500.51	539.42
2		471.88	509.46		23370.43*	421.60					500.69	539.60
21		463.55	513.64*					23336.05			506.44	557.40
31		463.23	513.91		370.43*	433.73					508.74	557.64
31		454.46	517.09					322.53			511.16	574.47
41	23404.05									23451.94	511.47	574.79
41	403.73	454.10	517.44	23304.95	308.23	443.92			23370.43*		514.93*	590.65
51	381.05	444.65	519.73*	288.49	364.14	451.94			367.37	451.08	515.31	590.99
51	381.30	444.31	520.07*	288.30	363.96	452.10			290.62	442.53	517.82	
61	358.52	434.00*	521.48*	270.18	358.14	457.98			272.11	359.93	519.73*	
61	358.14*	433.73*	521.80*	269.90	357.84	458.27			271.83	359.66	431.72	
71	334.53	422.35	522.08	250.14	350.26	462.07*			251.94	352.00	420.54	
71	334.21	422.03	522.40	249.72	349.85	462.46						
81	309.52	409.58	521.48*	228.32	340.35	464.09			251.54	351.58	420.17	
81	309.25	409.29	521.89*	227.79	340.01	464.70*			230.08	342.28	407.81	
91	283.45	395.58	519.73*	204.84	328.95	464.09			229.53	341.72	407.50	
91	283.26	395.39		204.13	328.25	464.70*						
101	256.13	380.19		179.56	315.41	462.07*						
101				178.69	314.55	462.46						
111	227.60	363.40			299.92							
111					298.88							
121	187.94											
131												

*Overlapped line. †Observed but not measured.

TABLE II
 ROTATIONAL AND VIBRATIONAL CONSTANTS OF SiH (CM⁻¹)

	0-0 Band	1-0 Band	2-1 Band	2-2 Band
B''	7.391	7.390	7.177	6.961
D''	3.95×10^{-4}	3.94×10^{-4}	4.1×10^{-4}	3.8×10^{-4}
B'	7.287	6.858	6.347	6.347
D'	5.23×10^{-4}	6.01×10^{-4}	7.3×10^{-4}	7.26×10^{-4}
ν_0	24193.05	25853.70	25345.20	23445.40
A''	143.35	143.35	143.81	144.28

$$\omega_e'' = 2042.47, \omega_e x_e'' = 35.67, \omega_e' = 1858.13, \omega_e x_e' = 98.73, B_e'' = 7.498 - 0.214(v + \frac{1}{2}), \\ B_e' = 7.470 - 0.347(v + \frac{1}{2}) - 0.041(v + \frac{1}{2})^2, T_e = 24393.15, r_e'' = 1.521, r_e' = 1.523.$$

DISCUSSION

For SiH and related molecules, the correlation of the $^2\Pi$ and $^2\Delta$ states with the states of the separated atoms has been given by Mulliken (1932). The $^2\Pi$ state of the molecule, which is the ground state, dissociates into the ground states of the atoms. The $^2\Delta$ state of SiH dissociates into the ground state of hydrogen and the 1D state of silicon. Thus, if the energy necessary to dissociate the $^2\Delta$ state of SiH can be determined, then this value can be combined with the excitation of the 1D state of Si and the ν_{00} value of the $^2\Delta$ - $^2\Pi$ band system to give the dissociation energy of SiH.

It is evident from the constants given in Table II that the $^2\Delta$ state is a shallow one. An extrapolation of the two observed vibrational quanta to the dissociation limit gives a value of 7840 cm⁻¹ for the depth of the $^2\Delta$ potential curve. The error in this number may be quite large, perhaps as great as ± 2000 cm⁻¹. The dissociation energy of the $^2\Pi$ ground state of SiH, corresponding to this value for the $^2\Delta$ state, is 25740 ± 2000 cm⁻¹. Thus the relatively crude estimate of the depth of the $^2\Delta$ state leads to quite a good estimate of the dissociation energy of SiH. The dissociation energy of SiH is very nearly the same as that of the similar molecule CH.

The SiH molecule probably occurs in interstellar space and it is possible that interstellar absorption lines of SiH may be found. The wavelengths of the possible absorption lines are given in Table III. Of the lines listed in this table, the $R_{21}(\frac{1}{2})$ line at 4119.482 Å should be much the strongest since it is the only

 TABLE III
 POSSIBLE INTERSTELLAR ABSORPTION LINES OF SiH

Transition	ν (cm ⁻¹)	λ (Å)
$R_{21}(\frac{1}{2}), 0-0$	24268.02	4119.482
$Q_{21}(\frac{1}{2}), 0-0$	247.04	4123.052
	247.23	4123.022
$R_{11}(\frac{1}{2}), 0-0$	252.99	4122.040
	253.18	4122.008
$R_{21}(\frac{3}{2}), 0-0$	292.02	4115.417
	292.22	4115.384
$R_{21}(\frac{1}{2}), 1-0$	25928.20	3855.711

line of the 0-0 band arising from the lowest rotational level and the 0-0 band is much stronger than the 1-0 band. This line occurs on the published spectra of both Jackson and Rochester. Jackson has given an incorrect assignment to the line and Rochester has not assigned it. It is interesting to note that for the corresponding electronic transition of CH it is not the first R_{21} line but the first R_1 line which arises from the lowest rotational level of the $^2\Pi$ state. This difference is quite in accord with theory (see Herzberg 1950, page 234) since, for SiH, the coupling of the $^2\Pi$ state is case (a) while for CH it is case (b).

A short search for other band systems of SiH failed to show any. The 0-0 band of the $^2\Delta-^2\Pi$ system is very strong and it appears that, with the source used here, any other bands which do occur are less than one-hundredth as intense as the 0-0 band.

I wish to thank Dr. G. Herzberg for his interest in this work and Miss L. Howe for carrying out much of the measurement and computation.

REFERENCES

- DOUGLAS, A. E. 1955. Can. J. Phys. **33**, 801.
HERZBERG, G. 1950. Molecular spectra and molecular structure, Vol. I, Spectra of diatomic molecules, 2nd ed. (D. Van Nostrand Co., Inc., New York).
JACKSON, C. V. 1930. Proc. Roy. Soc. A, **126**, 373.
MULLIKEN, R. S. 1931. Phys. Rev. **37**, 733.
——— 1932. Revs. Mod. Phys. **4**, 1.
MULLIKEN, R. S. and CHRISTY, A. 1931. Phys. Rev. **38**, 87.
ROCHESTER, G. D. 1936. Z. Physik, **101**, 769.

THE FREEZING POINTS OF HIGH PURITY METALS AS PRECISION TEMPERATURE STANDARDS

I. PRECISION MEASUREMENTS WITH STANDARD RESISTANCE THERMOMETERS¹

E. H. McLAREN

ABSTRACT

The techniques and difficulties encountered in measuring temperatures to the highest precision with platinum resistance thermometers are discussed. It is shown that the relative drift of the resistance coils in the Mueller resistance bridge used for these measurements is less than a part per million per year. The intrinsic resistance of a platinum thermometer is comparatively unstable, and results showing some effects of cold work and heat treatment on several thermometers are given.

As each precision temperature determination involves the resistance of the thermometer at the triple point of water, extensive measurements have been carried out to obtain information on: (a) the reproducibility of temperature in particular cells, (b) the variation in temperature among cells, and (c) the long term stability of cell temperatures.

The limiting uncertainties in temperature measurements due to variation in the bridge, the thermometers, and the triple point cells are each of the order of 10^{-4} °C.

INTRODUCTION

From -183°C . to 630°C . the International Temperature Scale is defined in terms of standard resistance thermometers that have been calibrated at the oxygen, ice, steam, and sulphur points; excellent reviews on temperature measurement in this range have been given by Mueller (1941), Stimson (1955), and Hall (1955). At the upper end of the range the limit of accuracy in temperature determinations is set by the degree of reproducibility of the sulphur boiling point; unfortunately the high degree of pressure dependence (10^{-4} °C. per micron Hg) and the considerable period, of the order of a day (Stimson 1955), that is required to establish temperature equilibrium adversely affect this reproducibility, which is considered to be of the order of 5×10^{-3} °C. (Hall 1955).

The freezing points of highly purified samples of various metals are free from these particular disadvantages; in this laboratory experiments on tin, cadmium, and zinc have shown pressure dependences of less than 10^{-4} °C. per cm. Hg and, with appropriate techniques, freezes with a duration of one to two hours that are readily reproducible to the order of 2×10^{-4} °C. These results suggest that the zinc point (419.5°C .) could usefully replace the sulphur point (444.600°C .) on the International Temperature Scale and they also provide a means of testing, to this order of accuracy, the validity of the interpolation formulae used for platinum resistance thermometers. Details of these experiments will be presented in Part II of this paper.

Temperature measurements to the order of 10^{-4} °C. are not only dependent on the stability and homogeneity of the measured environment, however, but

¹Manuscript received September 24, 1956.

Contribution from the Division of Applied Physics, National Research Council, Ottawa. Issued as N.R.C. No. 4176.

demand very great care in the selection and use of the measuring equipment. Part I of this paper describes the techniques that have been employed and the limitations that have been determined at this laboratory in the use of resistance bridges, platinum resistance thermometers, and water triple point cells.

RESISTANCE MEASUREMENTS

Equipment

The resistance measurements reported here were made on a Leeds and Northrup G-2 Mueller Bridge (Mueller 1916; Mueller 1941; Stimson 1955) thermostatted to plus or minus one hundredth of a degree at 35° C. and having an extra 10^{-8} ohm decade (LeLacheur 1952); a worm drive is used on the slide wire connecting the two ratio coils to give fine control on the bridge ratio adjustment. Extension leads to the thermometer junction boxes are No. 12 B and S gauge copper conductors terminating at copper binding posts and laid in half inch B X conduit. The detector is a Leeds and Northrup type HS galvanometer mounted on a Julius suspension in a draft-free compartment and having a nominal sensitivity of $0.017 \mu\text{v./mm.}$ at the 5.5 meter optical path distance employed. The equipment is located in an air-conditioned room which is semidarkened for taking measurements.

Stability

1. Bridge zero

For high precision measurements it is necessary to determine the correction to true zero resistance for the bridge. In Leeds and Northrup Mueller bridges the Wheatstone type network is trimmed so that a small positive excess of resistance remains in the X arm when the thermometer is shorted out; this off-zero resistance is measured and subsequently subtracted from every resistance determination. The measurement is made by galvanometer deflections using a branch current of 5 ma. and the uncertainty in the measured correction is less than one microhm. Values of the bridge zero correction over a two month period are shown in Fig. 1, the fluctuations being associated with

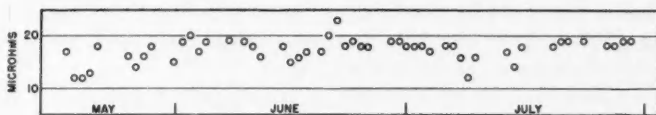


FIG. 1. A series of bridge zero corrections during a 10 week period.

slight changes in the resistance of connecting conductors and components that are outside the thermostatted section of the bridge. An error of 10 microhms in bridge zero will introduce an error of about 0.0002°C. in the temperature measured at the zinc point with a 25 ohm standard resistance thermometer.

2. Bridge Ratio

The bridge ratio, i.e. the ratio of the resistances of the two fixed 1000 ohm arms of the bridge, is closely monitored immediately after any precision resistance determination and the readings are corrected to unity ratio with an

uncertainty of less than one microhm. The ratio coils are mounted outside the thermostatted enclosure in the bridge and the greatest departures from unity occur when room temperatures vary abnormally. Occasionally the ratio may drift as much as four parts in ten million in a day, which, without correction, would correspond to an error of nearly 0.0002°C. in a calculated zinc temperature.

3. Bridge Resistors

The stability of the resistors in the bridge is of utmost importance in resistance determinations, and considerable time and effort must be spent in checking coil resistances when the greatest possible accuracy is being sought.

Fig. 2 shows the results over a period of two months of monitoring a Leeds and Northrup 10 ohm standard resistor, thermostatted to $\pm 0.01^\circ \text{deg.}$ against

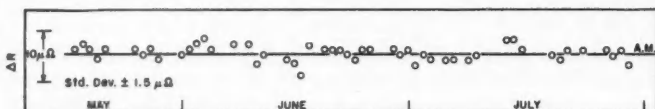


FIG. 2. The results of a series of difference measurements on a standard 10Ω resistor and the first resistor in the 10Ω decade of the bridge over a period of 10 weeks.

the 10 ohm coil in the first decade of the bridge. Each measurement was made with a branch current of 5 ma. in a single sequence of NRRN commutations. The standard deviation about the average resistance for the period is ± 1.5 microhms and is accounted for by the uncertainties attendant on balancing the bridge in the four commutations and determining the bridge zero and bridge ratio corrections. Resistance is estimated to the nearest microhm in each of these operations.

Systematic internal calibrations of the coils in the bridge have been carried out during the past two years, the 10-ohm coils about every month and the lower resistance coils at longer intervals. Results obtained from the comparison of individual 10-ohm coils against the sum of the 10 one-ohm coils in the bridge are given in Fig. 3. These results are given in terms of the bridge unit of resistance which is arbitrarily defined as one-tenth of the sum of the resistances of the 10 one-ohm coils in the bridge.

Fig. 3 shows that the relative drift of the resistors is less than a part per million per year except for the abrupt discontinuity that appeared in June 1955. This discontinuity occurred during a general power failure of several hours' duration which resulted in the section of the bridge which is normally thermostatted at 35°C. falling to room temperature. It is possible that the resulting change in relative resistance of the 10-ohm coils, varying between 0.8 and 2.4 parts per million, is due to work hardening of the manganin as the coil forms contracted. Provision has since been made for battery operated standby power to heat the enclosure. The conclusion drawn from these results is that the coils in the Leeds and Northrup bridge, when well aged and continuously thermostatted, have a stability comparable with that of the highest quality standard resistors.

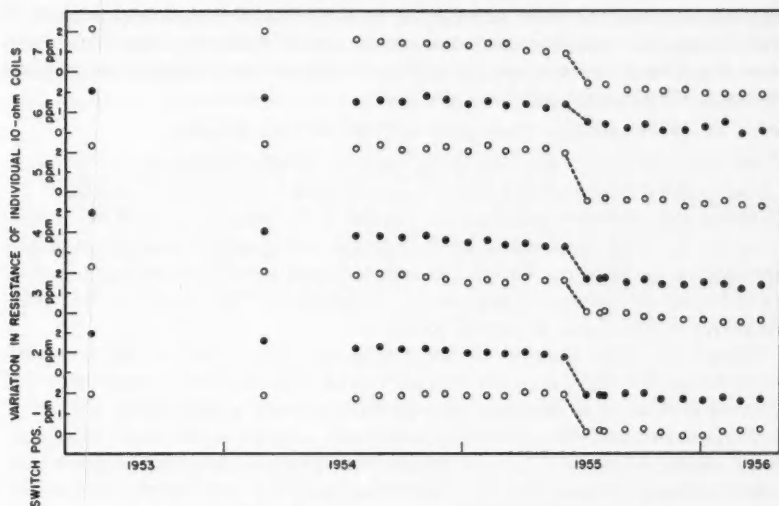


FIG. 3. Variation in resistance of individual coils in the 10 Ω decade against the sum of the 10 coils in the 1 Ω decade over a period of three years.

The importance of careful bridge calibration is evident from the following considerations: Temperature is determined from the ratio of the resistance of the thermometer at the temperature under investigation to its resistance at the ice point. Each of these resistances on the platinum thermometer will be balanced by the sum of perhaps 25 coils in the bridge and as the calibration of each coil in the bridge has an uncertainty of about ± 1 microhm the probable error in the determination of the resistance of the thermometer is of the order of ± 5 microhms. These combined uncertainties in calibrated resistance values result in a probable error of about $\pm 0.0001^\circ \text{C.}$ in a temperature measurement at the zinc point with a 25.5 ohm standard thermometer.

STABILITY OF R_{TP}

The equation relating the resistance of a platinum wire to the International Temperature Scale in the range 0°C. to 630°C. has the form

$$R_t = R_0(1 + At + Bt^2) \quad \text{or} \quad R_t = (R_{TP} - \Delta R)[1 + At + Bt^2]$$

where $\Delta R = R_{TP} - R_0$, A and B are temperature coefficients of the particular sample of platinum, R_t is the resistance of the wire at temperature t , and R_{TP} and R_0 are the resistances at the triple point of water and the ice point respectively. For work of the highest accuracy the resistance R_0 on a standard resistance thermometer is computed from the value of the resistance at the triple point of water, the ice point by definition being 0.01 deg. below the triple point. As R_{TP} enters into every temperature calculation the stability of the intrinsic resistance of a thermometer and the reproducibility of the temperature attained in water triple point cells directly affect all temperature

determinations. Definitive information on the constancy of the coefficients A and B is not yet available but an investigation to determine how R_{TP} varies with handling procedure and an intercomparison of the temperature realized in several triple point cells has been made.

(a) *Cold Work and Heat Treatment on Standard Thermometers*

As the electrical resistivity of a metal is a structure-sensitive property (Broom 1954) the specifications of the so-called "strain-free" standard resistance thermometer includes the terms "well-annealed" (C.I.P.M. 1948). This requirement ensures the relief of strain introduced in the drawing and fabrication procedures, but unfortunately there remains the possibility of introducing additional resistance by accidentally cold working the thermometer in the course of its day-to-day use.

Experience with 12 standard thermometers clearly indicates that even with very careful handling it is not possible to eliminate changes in resistance due to work hardening of the platinum. A gentle tap on the sheath near the coil of a Meyers thermometer (Stimson 1955) may add as much as 20 microhms (equivalent to 0.0002°C.) to its original resistance of about 25.5 ohms at the triple point of water. Subsequent annealing at 450°C. will remove part of the added resistance, the amount removed being dependent on the type of defects introduced into the wire; recovery from vacancy formation occurs more readily than recovery from defects produced by higher types of deformation (Broom 1954). Annealing at temperatures much higher than 450°C. is impractical for thermometers on mica crosses in pyrex sheaths.

The effect of this work hardening was studied on two standard thermometers: S144 made by Meyers and having a single layer bifilar coil about one inch long and TM-1 constructed at the National Research Council in the coiled helix form (Meyers 1932) with a coil length of about two inches. Each thermometer was first annealed at 450°C. until its resistance at the triple point of water went through a minimum, after which the cold work was applied by lightly striking the tips of the thermometers 40 times against the edge of a wooden table; they were then reannealed at 450°C. Fig. 4 shows how R_{TP} varied during the operation. Annealing removed 74% of the added resistance from thermometer S144 and only 13% from thermometer TM-1.

In an investigation to determine the effect of cold working on the temperature coefficients of platinum wire, three annealed thermometers were used to determine the R_{Zn}/R_{TP} ratios on four zinc freezes. One of the thermometers,

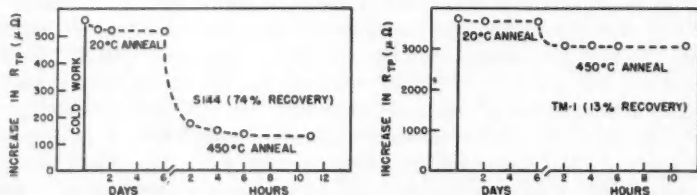


FIG. 4. Effect on R_{TP} of cold working and annealing two resistance thermometers.

S144, was then work hardened at room temperature until 14,000 microhms had been added to R_{TP} ; about 6000 microhms of this increase in resistance were removed by reannealing at 450° C. The R_{Zn}/R_{TP} ratios were again determined with the three thermometers on four zinc freezes. Table I shows that the ratio

TABLE I

	Before cold working S144		After cold working S144		ΔR_{TP} , p.p.m.	$\Delta(R_{Zn}/R_{TP})$, p.p.m.
	R_{TP} (b.u.)	R_{Zn}/R_{TP}	R_{TP} (b.u.)	R_{Zn}/R_{TP}		
S144	25.49243	2.567938	25.50081	2.567902	+329	-14
S156	25.48280	2.568059	25.48280	2.568059	0	0
S163	25.48099	2.567710	25.48099	2.567710	0	0

for the strained thermometer was lowered by 14 p.p.m. while the ratios for the untreated thermometers remained constant, the estimated uncertainty in a R_{Zn}/R_{TP} ratio measurement being less than 1 p.p.m. It appears from this experiment that cold working a thermometer permanently alters its temperature coefficients, if subsequent annealing is restricted to a temperature of 450° C.* In an effort to increase the temperature coefficients of thermometer S144 an electric current was used to heat the wire to 650° C. for one hour. This lowered the ratio R_{Zn}/R_{TP} by an additional 16 p.p.m., presumably owing to active contamination of the hot platinum by the mica cross.

Continual use of a thermometer at elevated temperatures also contributes to the steady increase of the annealed resistance at a given temperature. Fig. 5 shows the variation of the resistance at the zinc point, R_{Zn} , for a Meyers thermometer that was immersed continuously for 8 days at about 420° C.

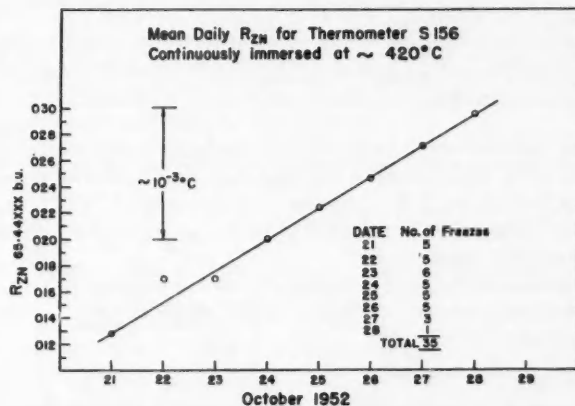


FIG. 5. Increase in resistance at R_{Zn} for a Meyers thermometer during heating.

*Corrucini (1951) demonstrated much greater lowering of temperature coefficients of annealed platinum wires by rapid quench hardening; reannealing at temperatures between 400° C. and 300° C., he was able to regain the original coefficients within the precision of his measurements, i.e. to within the order of 100 p.p.m.

R_{TP} increased proportionately, at the rate of 10 to 20 microhms per day, so that no measurable changes in the ratio R_{Zn}/R_{TP} occurred during this period. With the temperature coefficients of the wire apparently remaining constant the increase in the resistance during heat treatment is presumably caused by extension or volatilization of the platinum wire (Corrucini 1951).

Fig. 6 shows the variation of the reference resistance R_{TP} for a thermometer that has been used for several thousands of measurements at the freezing points of zinc, cadmium, and tin. Table II lists some resistance temperature

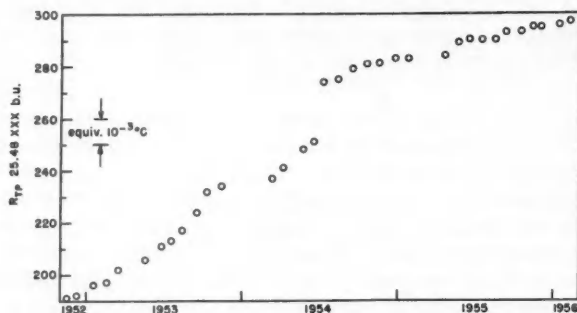


FIG. 6. Variation in the annealed resistance at R_{TP} for a thermometer used constantly in the range 0° to 450° C. over a period of three years.

TABLE II

	Sept. 1953	Feb. 1956	Relative change, p.p.m.
R_{TP}	25.48220 b.u.	25.48298 b.u.	+31
R_{Zn}	65.43966 b.u.	65.44181 b.u.	+33
$R_{Zn} - R_{TP}$	39.95746 b.u.	39.95883 b.u.	+34
R_{Zn}/R_{TP}	2.568054	2.568060	+ 2.3

relations that were determined for this thermometer in September, 1953, and in February, 1956. The change in the ratio R_{Zn}/R_{TP} implies an increase in the temperature coefficients of the platinum wire, presumably due to the long term heating. This increase of 2 p.p.m. corresponds to an increase of about 0.002° C. in a calculated zinc temperature.

Further studies on the long term stability of the temperature coefficients of platinum thermometers and of factors which may account for the observed changes are underway.

(b) Water Triple Point Cells

During November and December, 1954, a series of temperature measurements in several triple point cells prepared by Dr. R. S. Turgel, formerly of this laboratory, was designed to determine the variations in temperature between cells and any temperature dependence on the age of the ice mantles. Before making measurements all the thermometers used were annealed at

about 450° C. until recovery from previous cold work was completed and R_{TP} had begun to rise slowly; thereafter these thermometers were handled gently and were kept in the temperature range 0° C. to 23° C. The values of R_{TP} were measured with 1 ma. and 2 ma. currents through the thermometer and extrapolated to the zero current resistance.

Frequently it is found that the value of R_{TP} obtained on the day the ice mantle is prepared is lower by as much as 10 microhms than the average of the week. For this reason it is common practice here to allow a full day for the interface to attain temperature equilibrium before a cell is used in precision temperature determinations.

Fig. 7 shows the results* of monitoring R_{TP} with a single thermometer on a

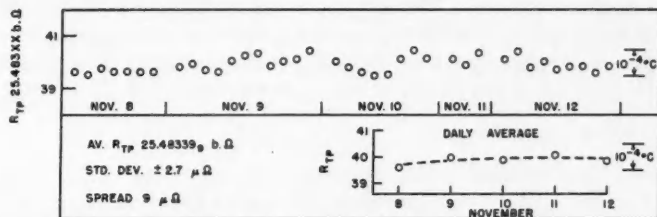


FIG. 7. Monitoring R_{TP} with a single thermometer on a single water triple point cell over a period of five days.

single cell for five days, the ice mantle being prepared on the first day. The standard deviation about the mean R_{TP} was 2.7 microhms with a maximum spread of 9 microhms. This is the smallest variation over this length of time that has been obtained in this laboratory, but it must be emphasized that the thermometer was used under conditions that normally are impractical, i.e. with a minimum of handling and in the absence of high temperature environments; the standard deviation about the mean R_{TP} of a thermometer that is being frequently handled and used at a variety of temperatures is of the order of two or three times this value.

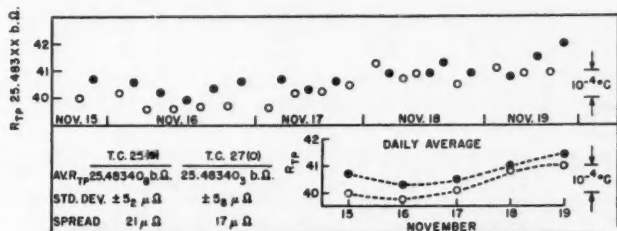


FIG. 8. Monitoring R_{TP} with a single thermometer on two water triple point cells over a period of five days.

*In Figs. 7, 8, and 9 and Tables III and IV the values of R_{TP} are given in arbitrary bridge ohms; i.e. the bridge reading is corrected to true zero and unity ratio but not to bridge units of resistance as defined above. This latter correction is unnecessary in view of the small differences in temperature between triple point cells.

Fig. 8 shows the results of monitoring two cells with the same thermometer for a similar period. Both the standard deviation and the spread from the mean R_{TP} for each cell are measurably larger than those shown in Fig. 7. The graph of the daily averages of R_{TP} clearly indicates a difference in temperature realized in the two cells.

An intercomparison of several triple point cells was carried out along the following lines. Each week ice mantles were prepared on four cells and were allowed one day to attain stability. Two series of measurements were made concurrently during the next four days, one of these being single daily determinations of R_{TP} on each cell with the same thermometer, S156, and the second consisting of three determinations of R_{TP} with each of four combinations of a thermometer and a cell, different combinations being measured each day: the use of four thermometers tends to average out errors arising from increases in R_{TP} due to accidental cold working of the thermometers during handling. Tables III to VI give the results of the intercomparisons, T.C. 27 being used

TABLE III
SINGLE THERMOMETER INTERCOMPARISON (1954)
 R_{TP} on thermometer S156 in bridge ohms

	T.C. 27	T.C. 25	T.C. 32	T.C. 33	Daily av. for group	Deviation of daily average from weekly average
Nov. 23	25.483406	25.483415	25.483404	25.483415	25.483410	-2 $\mu\Omega$
24	409	413	416	415	413	+1
25	407	414	412	416	412	0
26	407	425	414	413	415	+3
Weekly average	25.483407	25.483417	25.483412	25.483415	25.483412	
Rel. to T.C. 27	0 $\mu\Omega$	+10 $\mu\Omega$	+5 $\mu\Omega$	+8 $\mu\Omega$		
	T.C. 27	T.C. 22	T.C. 21	T.C. 24		
Nov. 30	25.483408	25.483409	25.483406	25.483414	25.483409	-1 $\mu\Omega$
Dec. 1	405	413	408	411	409	-1
2	410	412	410	412	411	+1
3	411	411	412	414	412	+2
Weekly average	25.483408	25.483411	25.483409	25.483413	25.483410	
Rel. to T.C. 27	0 $\mu\Omega$	+3 $\mu\Omega$	+1 $\mu\Omega$	+5 $\mu\Omega$		
	T.C. 27	T.C. 31	T.C. 29	T.C. 25		
Dec. 7	25.483413	25.483404	25.483415	25.483418	25.483412	-1 $\mu\Omega$
8	415	394	417	421	412	-1
9	416	404	419	420	415	+2
10	423	388	416	423	412	-1
Weekly average	25.483417	25.483398	25.483417	25.483420	25.483413	
Rel. to T.C. 27	0 $\mu\Omega$	-19 $\mu\Omega$	0 $\mu\Omega$	+3 $\mu\Omega$		

TABLE IV
FOUR-THERMOMETER INTERCOMPARISON (1954)
 R_{TP} in bridge ohms

	Cell	S156	Cell	S155	Cell	S165	Cell	S214
Nov. 23	27	25.483406	33	25.478053	32	25.481604	25	25.485514
24	25	413	27	050	33	609	32	511
25	32	412	25	056	27	606	33	511
26	33	413	32	059	25	611	27	510
Weekly average		25.483411		25.478054		25.481608		25.485512
Nov. 30	27	25.483408	22	25.478054	21	25.481607	24	25.485512
Dec. 1	22	413	21	052	24	611	27	505
2	21	410	24	056	27	607	22	514
3	24	414	27	052	22	610	21	509
Weekly average		25.483411		25.478054		25.481609		25.485510

	Cell	S163*	Cell	S155	Cell	S165	Cell	S214
Dec. 7	27	25.479536	31	25.478046	29	25.481603	25	25.485515
8	25	550	27	053	31	594	29	509
9	29	540	25	062	27	609	31	483
10	31	511	29	057	25	616	27	511
Weekly average		25.479534		25.478054		25.481606		25.485504

*Thermometer S163 substituted for S156, which was temporarily unserviceable at the beginning of this week.

TABLE V
DEVIATION OF R_{TP} IN $\mu\Omega$ FOR INDIVIDUAL CELLS FROM
THE WEEKLY GROUP AVERAGE (1954)

	S156	S155	S165	S214	Sum four thermometers	Average deviation thermometer	Cell R_{TP} rel. to T.C. 27
T.C. 27	-5 $\mu\Omega$	-4 $\mu\Omega$	-2 $\mu\Omega$	-2 $\mu\Omega$	-13 $\mu\Omega$	-3 $\mu\Omega$	0 $\mu\Omega$
25	+2	+2	+3	+2	+9	+2	+5
32	+1	+5	-4	-1	+1	0	+3
33	+2	-1	+1	-1	+1	0	+3
T.C. 27	-3 $\mu\Omega$	-2 $\mu\Omega$	-2 $\mu\Omega$	-5 $\mu\Omega$	-12 $\mu\Omega$	-3 $\mu\Omega$	0 $\mu\Omega$
22	+2	0	+1	+4	+7	+2	+5
21	-1	-2	-2	-1	-6	-2	+1
24	+3	+2	+2	+2	+9	+2	+5

	S163*	S155	S165	S214			
T.C. 27	+2 $\mu\Omega$	-1 $\mu\Omega$	+3 $\mu\Omega$	+7 $\mu\Omega$	+11 $\mu\Omega$	+3 $\mu\Omega$	0 $\mu\Omega$
31	-23	-8	-12	-21	-64	-16	-19
29	+6	+3	-3	+5	+11	+3	0
25	+16	+8	+10	+11	+45	+11	+8

*Thermometer S163 substituted for S156, which was temporarily unserviceable at the beginning of this week.

TABLE VI
DEVIATION OF R_{TP} IN $\mu\Omega$ OF THE DAILY GROUP AVERAGE
FROM THE WEEKLY GROUP AVERAGE (1954)

	S156	S155	S165	S214	Sum four thermometers	Deviation of daily average from weekly average (sum/4)
Nov. 23	-5 $\mu\Omega$	-1 $\mu\Omega$	-4 $\mu\Omega$	+2 $\mu\Omega$	-8 $\mu\Omega$	-2 $\mu\Omega$
24	+2	-4	+1	-1	-2	0
25	+1	+2	-2	-1	0	0
26	+2	+5	+3	-2	+8	+2
Nov. 30	-3 $\mu\Omega$	0 $\mu\Omega$	-2 $\mu\Omega$	+2 $\mu\Omega$	-3 $\mu\Omega$	-1 $\mu\Omega$
Dec. 1	+2	-2	+2	-5	-3	-1
2	-1	+2	-2	+4	+3	+1
3	+3	-2	+1	-1	+1	0

	S163*	S155	S165	S214		
Dec. 7	+2 $\mu\Omega$	-8 $\mu\Omega$	-3 $\mu\Omega$	+11 $\mu\Omega$	+2 $\mu\Omega$	0 $\mu\Omega$
8	+16	-1	-12	+5	+8	+2
9	+6	+8	+3	-21	-4	-1
10	-23	+3	+10	+7	-3	-1

*Thermometer S163 substituted for S156, which was temporarily unserviceable at the beginning of this week.

as a reference cell. An additional intercomparison between R_{TP} values of National Research Council triple cell 25 and a cell loaned to us by the J. and J. Instrument Co., Silver Spring, Md., was carried out in March, 1955, with thermometer S156 and the results are presented in Fig. 9.

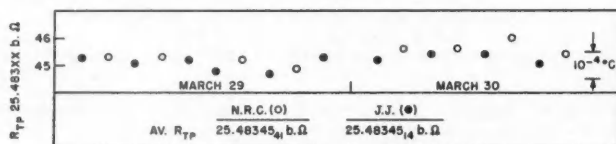


FIG. 9. Intercomparison of R_{TP} values for a J. and J. cell and an N.R.C. cell.

Table VII(a) summarizes the intercomparison of National Research Council triple point cells by relating all cells to T.C. 27 in terms of the measured average differences in R_{TP} in microhms. The weighted mean differences were calculated because the four-thermometer measurements include twice as many determinations of R_{TP} on each cell as the single-thermometer ones. The excellent agreement between the results of the two series of measurements justifies the conclusion that there are differences in R_{TP} between cells of less than 10 microhms that are real and measurable.

For a 25.5 ohm standard resistance thermometer at the triple point of water, a change in resistance of 10 microhms is equivalent to about 0.0001°C . so that the average temperatures of eight of the National Research Council cells were well inside 0.0001°C . The remaining cell, yielding a temperature about 0.0002°C . lower, was discarded as being substandard.

TABLE VII
SUMMARY (1954)
(a) ΔR_{TP} of cells relative to T.C. 27

Cell	Single thermometer comparison	Four thermometer comparison	Weighted mean difference
27	0 $\mu\Omega$	0 $\mu\Omega$	0 $\mu\Omega$
21	+ 1	+ 1	+ 1
22	+ 3	+ 5	+ 4
24	+ 5	+ 5	+ 5
25	+ 6	+ 6	+ 6
29	0	0	0
31	-19	-19	-19
32	+ 5	+ 3	+ 4
33	+ 8	+ 3	+ 5

(b) ΔR_{TP} with age of ice mantle

Deviation of daily average from weekly average					
	Week	2nd day	3rd day	4th day	5th day
Single thermometer	1	-2 $\mu\Omega$	+1 $\mu\Omega$	0 $\mu\Omega$	+3 $\mu\Omega$
	2	-1	-1	+1	+2
	3	-1	-1	+2	-1
Average deviation		-1	0	+1	+1
Four thermometers	1	-2	0	0	+2
	2	-1	-1	+1	0
	3	0	+2	-1	-1
Average deviation		-1	0	0	0

In order to obtain information on the long term stability of the cells a second intercomparison was made during April and May, 1956. Table VIII shows the results of the two intercomparisons. No measurable change in the relative differences was observed for six cells, two cells indicated changes only slightly greater than the uncertainty of measurement, which is considered to be of the

TABLE VIII
 R_{TP} OF CELLS RELATIVE TO T.C. 27
The limiting uncertainty in a difference measurement
is of the order of 3 $\mu\Omega$

Cell	Nov. Dec./54	Apr. May/56	Change in R_{TP}
27	0 $\mu\Omega$	0 $\mu\Omega$	—
21	+ 1	+ 2	—
22	+ 4	+ 1	- 3 $\mu\Omega$
24	+ 5	+ 4	—
25	+ 6	- 9	-15
29	0	+ 1	—
31	-19	-15	+ 4
32	+ 4	+ 5	—
33	+ 5	+ 3	—

order of three microhms, and the remaining cell showed a temperature drop of 0.00015°C . This decrease in triple point temperature was caused by air entering the cell, possibly through a very fine crack in the pyrex envelope.

In these experiments there was no indication of a correlation between the differences in equilibrium temperatures among the eight National Research Council cells and the hydrostatic head of water on the interface. As an additional check on this matter temperatures against depths of immersion of a thermometer were measured in a cell with an ice mantle 14 in. long. Although some evidence was obtained suggesting a trend of decreasing temperatures at greater depths, of the same order of magnitude as the standard pressure effect on the freezing temperature of water, the reproducibility was poor; it is possible that convection currents in the thermometer well result in variations from the expected temperature gradient.

Table VII(b) shows an analysis of the 1954 data with a view to detecting any changes of cell temperature with the age of the ice mantles from the second to the fifth day. The variations found are well inside the uncertainty of the measurements.

CONCLUSION

These experiments suggest that the practical limit in precision temperature determinations is of the order of $10^{-4^{\circ}}\text{C}$. ($10^{-4^{\circ}}\text{C} \equiv 10\ \mu\Omega$ for 25.5 ohm platinum thermometers) using present-day equipment. The uncertainty due to the detection and calibration of resistances of the platinum thermometer is somewhat less than 10 microhms and variations in temperature among triple point cells appears to be of the order of $10^{-4^{\circ}}\text{C}$. Normal handling of well-annealed platinum resistance thermometers may introduce errors of this order of magnitude due to accidental straining of the wire during the course of a measurement.

These similar limitations placed on temperature measurement by the bridge, triple point cells, and the platinum thermometers, resulting from a well-balanced experimental technique, combine to form a formidable barrier to any substantial increase in precision.

REFERENCES

- BROOM, T. 1954. *Advances in Physics*, **3**, 26.
COMITÉ INTERNATIONAL DES POIDS ET MESURES. 1948. *Procès-Verbaux des Séances*, **21**, T37.
CORRUCINI, R. J. 1951. *J. Research NBS*, **47**, 94.
HALL, J. A. 1955. *Temperature, its measurement and control in science and industry*, Vol. 2 (Reinhold Publishing Corporation, New York), p. 115.
LELACHEUR, R. M. 1952. *Rev. Sci. Instr.* **23**, 383.
MEYERS, C. H. 1932. *J. Research NBS*, **9**, 807.
MUELLER, E. F. 1916. *Bur. Standards Bull.* **13**, 547.
———. 1941. *Temperature, its measurement and control in science and industry* (Reinhold Publishing Corporation, New York), p. 162.
STIMSON, H. F. 1955. *Temperature, its measurement and control in science and industry*, Vol. 2 (Reinhold Publishing Corporation, New York), p. 141.

PROPERTIES OF GALLIUM INDIUM ANTIMONIDE¹

J. S. BLAKEMORE²

ABSTRACT

Electrical conductivity and Hall effect are measured for *p*-type specimens of polycrystalline GaSb.InSb with impurity concentration about 10^{17} cm.⁻³. Analysis of these data suggests that $\mu_n/\mu_p = 11$, and that the intrinsic gap varies linearly with temperature from 0.265 ev. at 0° K. Measurement of the photoconductive limit at various temperatures shows that the gap widens on heating, though the electrical data seem difficult to reconcile with the large gradient of $+1.1 \times 10^{-3}$ ev./° C. indicated by the optical data.

1. INTRODUCTION

The study of semiconducting intermetallic compounds is a matter which has received appreciable attention only in the last few years, yet already a considerable amount of systematic data has been brought to light (e.g. Welker 1954; Frederikse and Blunt 1955). Much of this work has been concerned with compounds formed between elements of the third and fifth groups of the periodic table, such as InSb.

One aspect of semiconductor investigation concerns the properties of alloys in various proportions between two related semiconductors. Thus the properties of germanium-silicon alloys (Levitas *et al.* 1954) are found to vary continuously according to the proportion of silicon in the alloy, whilst Nussbaum (1954) has found a similar gradation of properties in Te-Se alloys. When we come to alloys between two semiconducting compounds, Busch and Winkler (1953) have found that the intrinsic gap in alloys of the type $Mg_2Ge_ySn_{(1-y)}$ varies for different values of *y* between the gap values for Mg_2Ge and Mg_2Sn . Welker (1955) finds that the gap width in ternary alloys between GaP and GaAs also varies regularly between the values for the binary phases which form the limits of composition.*

In this paper, results are presented on one composition of the ternary phase between InSb and GaSb, that represented by the equimolecular composition GaSb.InSb. Goryunova and Fedorova (1955) have found that a wide range of solid solution exists between these binaries. These authors found that X-ray powder pictures showed bands rather than sharp lines, indicative of a range of interatomic spacings. This suggests that in GaSb.InSb we have a disordered alloy rather than an ordered compound with the chalcopyrite structure. This hypothesis is supported by the nature of the solidus curve for this ternary system (Koster and Thoma 1955).

¹Manuscript received September 4, 1956.

Contribution from the Physics Department, University of British Columbia, Vancouver, B.C.

²Now at Minneapolis-Honeywell Research Center, Hopkins, Minn., U.S.A.

*These ternary alloys permit a continuous range of composition and are quite distinct from the ternaries discussed by Goodman and Douglas (1954), of the type ABX_2 where A comes from the first group of the periodic table, B from the third, and X from the sixth. The latter compounds will achieve the electronic balance for semiconducting behavior only when A and B are present in equal atomic proportions.

By analogy with the results of Welker (1955) quoted above we might expect GaSb.InSb to exhibit an intrinsic gap somewhere between the limits of 0.23 ev. (InSb) and 0.77 ev. (GaSb) at absolute zero with a negative temperature coefficient of some -4×10^{-4} ev./° C. (e.g. Roberts and Quarrington 1955).

It is of interest to know how mobilities and effective masses in GaSb.InSb will compare with those in the parent binaries. The valence band properties in GaSb and InSb are not very different, the mobility at room temperature being about 700 cm.²/volt.second for pure samples of either, whilst the effective mass ratio (m_p/m_0) differs only by a factor of two between the compounds. The conduction bands in the two binaries, however, show marked differences. That in GaSb is "normal", with an effective mass ratio of some 0.2, whilst the corresponding electron mobility is moderate. But electron mobilities in InSb are extremely large, corresponding with a very small electron mass ratio of some 0.015 (Frederikse and Blunt 1955). The consequent small density of states renders degeneracy likely for *n*-type samples (Burstein 1954) with consequent complexity in interpretation of measurements. It is clearly of interest to know how the behavior of the conduction band in GaSb.InSb compares with the differing attributes of this band in GaSb and InSb.

2. EXPERIMENTAL PROCEDURES AND RESULTS

(1) *Material Used*

The specimens used all came from a single ingot kindly made available by Standard Telecommunication Laboratories Ltd., of Enfield, England. The electrical properties showed the material to be *p*-type, with an effective acceptor concentration slightly over 10^{17} cm.⁻³. This crystal was produced by the horizontal zone melting method, and was polycrystalline with an average grain size of about 0.5 mm. There were a number of cracks near the outer surface of the ingot, and it was mechanically rather fragile, presumably owing to the polycrystalline character. Cleaved or polished surfaces were fairly bright with a slight bluish tint, and the coloration was enhanced on etching with agents such as CP4.

(2) *Electrical Properties*

Specimens were cut as rectangular slabs for measurement of electrical conductivity and Hall coefficient by standard d-c. techniques. Contacts were applied by soldering with lead-tin solder or indium, and at high temperatures pressure contacts were used. Observations of conductivity were made over the temperature range 77° K. to 750° K., whilst the Hall effect measurements were made up to 600° K. The Hall coefficient was constant in the extrinsic range, indicating that the extrinsic activation energy is very small. The electrical conductivity varied slowly below room temperature, reflecting a small temperature dependence of hole mobility. Results for one specimen in the temperature region of maximum interest are shown in Fig. 1.

(3) *Optical Absorption*

Several slices of material were reduced in thickness by grinding and the surfaces then polished. Owing to the fragility of thin sections, only one survived, which had been reduced only as far as 0.5 mm. The optical transmission

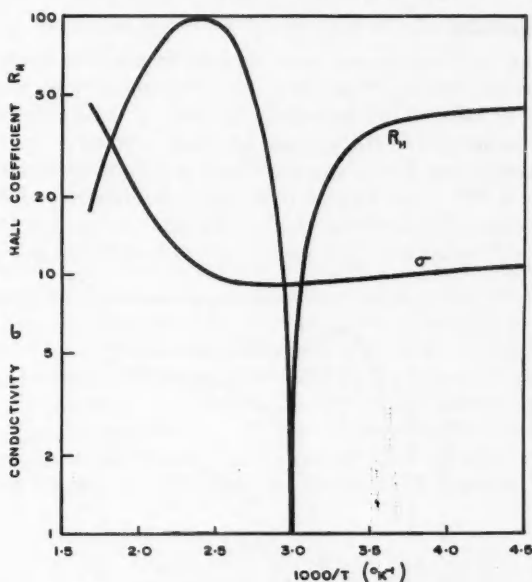


FIG. 1. Electrical conductivity σ ($\text{ohm}^{-1} \text{cm}^{-1}$) and Hall coefficient R_H ($\text{cm}^2/\text{coulomb}$) as a function of reciprocal temperature for specimen 108, in which $(N_a - N_d) = 1.7 \times 10^{17} \text{cm}^{-3}$.

was measured at 295° K. using conventional techniques with a Perkin Elmer model 83 monochromator and vacuum thermocouple. Assuming a refractive index of approximately four, the reflection coefficient should be 0.36, and this figure is used to convert values of transmission factor into the corresponding ones of absorption coefficient, shown in Fig. 2 as a function of wavelength. It will be noted that the absorption edge is very diffuse, and that the minimum absorption coefficient is still quite high.

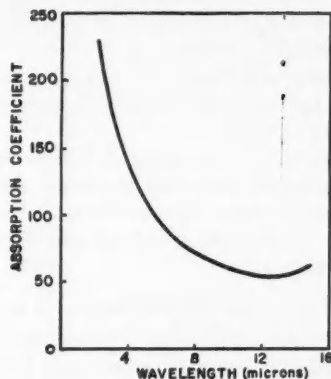


FIG. 2. Optical absorption coefficient α (cm^{-1}) as a function of wavelength for a slice 0.5 mm. thick.

(4) Photoconductivity

The experimental arrangement used for photoconductive observations has been described previously (Blakemore 1956). Specimens were prepared with four contacts. In view of the very low resistance of these cells, a high ratio step-up transformer preceded the tuned amplifier system.

The photoconductive signal was the same for a light beam interrupted at 90 c.p.s. and at 870 c.p.s., indicating an electron lifetime of less than 10^{-4} seconds. The spectral dependence of photoconduction, expressed as the fractional increase of conductivity per incident photon, is shown in Fig. 3 for one

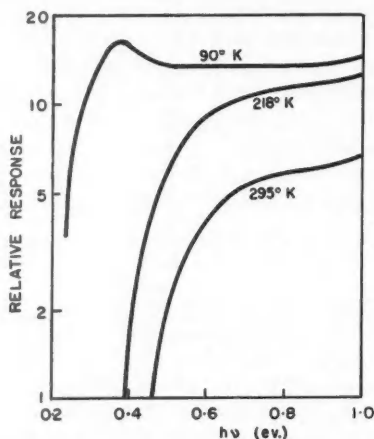


FIG. 3. Intrinsic photoconductive response plotted on an equal-photon basis, as a function of photon energy for three temperatures (specimen 125, in which $(N_a - N_d) = 2.3 \times 10^{17} \text{ cm}^{-3}$).

specimen measured at three temperatures. This is fully representative of the data collected on other cells. The units for the ordinate of this figure are the same for the three curves: unity on this is equivalent to an electron lifetime of 10^{-9} seconds for unit quantum efficiency.

This figure reveals at once a striking and unexpected fact: that the intrinsic response extends further into the infrared at low temperatures, i.e. the intrinsic energy gap increases with temperature.

The position of the "edge" is quite sharp at 0.36 eV. for 90° K. with all the cells studied. At the higher temperatures the edge is more diffuse. By considering the points of intersection of lines drawn from the high energy and low energy portions of these curves, optical gaps of about 0.51 eV. at 218° K. and 0.59 eV. at 295° K. are deduced.

3. DISCUSSION

The interpretation of electrical conductivity and Hall coefficient to obtain values of the electron and hole concentrations n and p , and the corresponding mobilities μ_n and $\mu_p = \mu_n/b$, has been described by Pearson and Bardeen

(1949) and by Beckenridge *et al.* (1954). It need only be briefly indicated here. The equations at our disposal are

$$(1) \quad R_H = \frac{3\pi}{8e} \times \frac{p-nb^2}{(p+nb)^3},$$

$$(2) \quad \sigma = e\mu_p(p+nb),$$

and at all temperatures

$$(3) \quad (p-n) = (N_a - N_d),$$

where N_a and N_d are the densities of acceptor and donor impurity centers, assumed completely ionized. In a stable material $(N_a - N_d)$ will be unchanged by heating, but in GaSb, InSb we find that samples heated above 500° K. show signs of a decrease in this quantity which is only partly reversed on cooling. In consequence, results computed above 500° K. are not taken into account in considering the temperature variation of the intrinsic carrier concentration.

From the limiting value of R_H at low temperatures it emerges that for specimen 108 (as illustrated in Fig. 1) the effective acceptor concentration $(N_a - N_d) = 1.7 \times 10^{17} \text{ cm}^{-3}$. Comparing this with the negative maximum of R_H , which is

$$(4) \quad R_{\max} = -\frac{3\pi}{8e} \times \frac{(b-1)^2}{4b(N_a - N_d)},$$

it is found that in this material the mobility ratio $b = \mu_n/\mu_p = 11$. These two quantities enable us to find the values of n and p corresponding with the value of the Hall coefficient at any temperature.

Simultaneous knowledge of the electrical conductivity σ then permits evaluation of the hole mobility μ_p , as shown in Fig. 4. The steeply sloping portion for high temperatures, where the form of variation is approximately $\mu_p \propto T^{-2.7}$, results from lattice scattering, whilst the more nearly constant

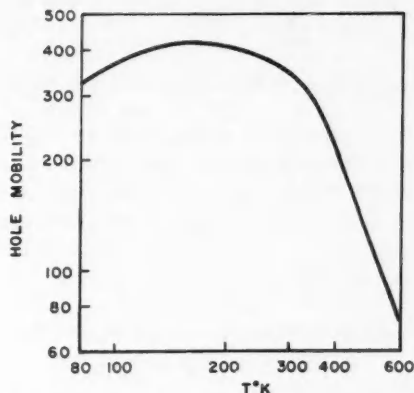


FIG. 4. Free hole mobility μ_p ($\text{cm}^2/\text{volt}\cdot\text{second}$) as a function of temperature for specimen 108.

mobility at lower temperatures is presumably the result of impurity and dislocation scattering.

Let us now return to consideration of carrier concentrations. For specimen 108, values of n and p are deduced from the Hall coefficient for temperatures above about 280° K. (At lower temperatures R_H lies too close to the exhaustion value to permit accurate evaluation of n .) Above this temperature one can thus compute the intrinsic concentration $n_i = (np)^{1/2}$, which is also given by

$$(5) \quad \begin{aligned} n_i &= 2(2\pi m_0 kT/h^2)^{3/2} M^{3/2} \exp(-E/2kT) \\ &= 4.83 \times 10^{15} (MT)^{3/2} \exp(-E/2kT) \text{ cm.}^{-3} \end{aligned}$$

where the composite mass factor $M = (m_n m_p / m_0^2)^{1/2}$, and E is the intrinsic gap width.

The corresponding data for n_i on this specimen are shown in Fig. 5, where $n_i/T^{3/2}$ is given as a function of $1000/T$. Over the temperature range up to

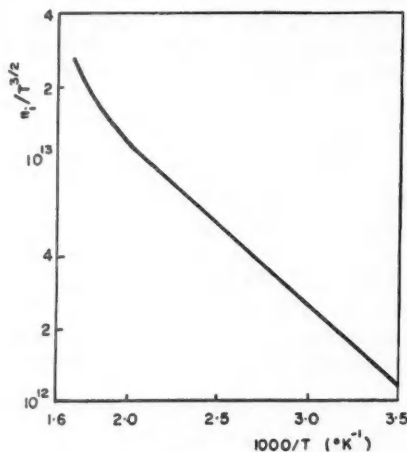


FIG. 5. Variation of $n_i/T^{3/2}$ against $1000/T$ for specimen 108. For n_i in units of cm.^{-3} .

500° K. the behavior is represented quite closely by a straight line on this semilogarithmic plot, which suggests that the variation of intrinsic gap with temperature is essentially linear. The data of Fig. 5 can be expressed as

$$(6) \quad n_i = 2.5 \times 10^{14} T^{3/2} \exp(-0.265/2kT) \text{ cm.}^{-3}$$

and if we assume that

$$(7) \quad E = E_0 + \beta T,$$

then the identification follows that $E_0 = 0.265 \text{ ev.}$, whilst

$$(8) \quad \exp(\beta/2k) = 19.3 M^{3/2},$$

so that a knowledge of the effective mass ratio is contingent on that of the temperature dependence of the intrinsic gap. The optical transmission and

photoconductive studies reported in Section 2 were carried out with this in mind. Whilst the optical absorption data of Fig. 2 do not provide an absorption edge sufficiently definite to be of much assistance, the photoconductive values for the intrinsic edge are reasonably well defined. The critical photon energies for the three temperatures do in fact fit quite well with a variation

$$(9) \quad E = 0.265 + 1.1 \times 10^{-3} T \text{ ev.}$$

and the occurrence of 0.265 ev. as the extrapolation to 0° K. is indeed remarkable. However, the positive temperature coefficient of the intrinsic gap seems inordinately large by comparison with the values found for other semiconductors. Moreover, if this value for β is substituted in Equation 8, the result is obtained that $M = 10$, which is larger by at least an order of magnitude than would be expected from the values for other intermetallic compounds. Moreover, such a large effective mass ratio is inconsistent with the fairly high mobilities noted both for electrons and for holes in this material.

In these circumstances no definite conclusions can be drawn concerning the place of this ternary alloy in the scheme of semiconducting compounds until more information is available, preferably on both n - and p -type crystals of widely varying impurity content.

ACKNOWLEDGMENTS

The author wishes to thank Mr. T. R. Scott of Standard Telecommunication Laboratories Ltd. for the crystal used in this investigation, and the Defence Research Board of Canada for their support of this work.

REFERENCES

- BLAKEMORE, J. S. 1956. *Can. J. Phys.* **34**, 938.
BRECKENRIDGE, R. G. *et al.* 1954. *Phys. Rev.* **96**, 571.
BURSTEIN, E. 1954. *Phys. Rev.* **93**, 632.
BUSCH, G. and WINKLER, U. 1953. *Helv. Phys. Acta*, **26**, 578.
FREDERIKSE, H. P. R. and BLUNT, R. F. 1955. *Proc. I.R.E.* **43**, 1828.
GOODMAN, C. H. L. and DOUGLAS, R. W. 1954. *Physica*, **20**, 1107.
GORYUNOVA, N. A. and FEDOROVA, N. N. 1955. *J. Tech. Phys.* **25**, 1339.
KOSTER, W. and THOMA, B. 1955. *Z. Metallkunde*, **46**, 293.
LEVITAS, A., WANG, C. C., and ALEXANDER, B. H. 1954. *Phys. Rev.* **95**, 846.
NUSSBAUM, A. 1954. *Phys. Rev.* **94**, 337.
PEARSON, G. L. and BARDEEN, J. 1949. *Phys. Rev.* **75**, 865.
ROBERTS, U. and QUARRINGTON, J. E. 1955. *J. Electronics*, **1**, 152.
WELKER, H. 1954. *Physica*, **20**, 893.
— 1955. *J. Electronics*, **1**, 181.

SELECTIVE REFLECTION FROM MERCURY VAPOR AT HIGH PRESSURES¹

J. A. GALT² AND H. L. WELSH

ABSTRACT

Selective reflection from mercury vapor in the region of the 2537 Å resonance line was investigated at pressures up to 340 atm. using reflection cells of special design. The results were interpreted on the basis of the classical theory of reflection from an absorbing medium. By fitting calculated curves to the experimental reflection contours, values of the oscillator strength, f , and the damping constant, γ , were determined. The f values so obtained are density-dependent and at high pressures are approximately equal to one half the value for the free atom. As predicted by theory, the damping constant varies directly as the density of the atoms in the vapor. This result contradicts the earlier work of Welsh, Kastner, and Lauriston (1950) in which it was concluded that γ varies as the square root of the density. A subsidiary reflection maximum was observed at 2540 Å; it is attributed to Hg₂ molecules which occur in relatively large concentrations at high densities. Some preliminary observations on the selective reflection at the 1850 Å resonance line were made up to 4.4 atm.

INTRODUCTION

Selective reflection from a metallic vapor in the neighborhood of its resonance lines, discovered by Wood (1909) in mercury vapor at 2537 Å, has been studied more recently by Welsh, Kastner, and Lauriston (1950) in mercury and cadmium vapors and by Lauriston and Welsh (1951) in the vapors of the alkali metals. In these later investigations light of continuous spectral distribution was reflected from the inner surface of a window in contact with the vapor and the reflectivity of the interface was determined as a function of frequency. Vapor pressures in the range 0.1 to 15 atm. were used for mercury and cadmium, and 0.02 to 1 atm. for the alkali metals. Selective reflection from mercury vapor has been studied at low vapor pressures by Cojan (1954), employing ingenious methods to resolve the individual hyperfine components of the 2537 Å line.

The classical theory of reflection from an absorbing medium was used by Welsh *et al.* to fit the experimental reflection contours with calculated curves obtained by varying the values of the oscillator strength, f , and the damping constant, γ , in the anomalous dispersion equations. In the medium pressure range the experimental contours could be reasonably well reproduced by using a constant value of f and values of γ which varied as the square root of the number of atoms, N_a , per cubic centimeter. The f value so determined agreed, in general, with the value determined by other methods. At pressures above 5 atm., however, it did not appear possible to obtain calculated contours in agreement with experiment by any variation of f and γ . The density dependence of the damping constant, $\gamma \propto \sqrt{N_a}$, deduced in these selective

¹Manuscript received August 31, 1956.

Contribution from the McLennan Laboratory, University of Toronto, Toronto, Ontario. This research was supported by a grant from the National Research Council of Canada.

²Holder of National Research Council Scholarships, 1950-53. Present address: Research Centre, Du Pont Company of Canada Limited, Kingston, Ontario.

reflection experiments differs fundamentally from the dependence, $\gamma \propto N_a$, which holds quite generally for emission and absorption lines. This apparent difference between the broadening processes involved in selective reflection and in absorption was difficult to understand.

The purpose of the present work was to investigate the apparently anomalous behavior of the selective reflection at high densities. The mercury line at 2537 Å was used, since it lies in a convenient spectral region, and since mercury vapor pressures of several hundred atmospheres can be produced without undue experimental difficulties.

Selective reflection in the neighborhood of the strong resonance line of mercury at 1850 Å has not been previously investigated; some preliminary observations on this line are reported in Appendix I.

EXPERIMENTAL PROCEDURE

To generate vapor pressures of mercury up to, say, 400 atm. requires temperatures up to 1100° C. For pressures lower than 50 atm. the mercury can be contained in a sealed fused quartz tube with thick walls and heated in a simple furnace. At higher pressures it would be necessary to apply an external gas pressure to balance the vapor pressure; the reflection cell and furnace would thus have to be placed in a pressure vessel. However, since at high temperatures fused quartz becomes permeable to gases, the gas in the pressure vessel would diffuse through the window and walls of the cell and mix with the mercury vapor. A satisfactory design of the reflection cell thus presents some difficulties. In the design adopted here the walls of the cell were of stainless steel and the window was a long cone of fused quartz. A temperature difference of over 1000° C. could be maintained between the lower end of the cone, in contact with hot mercury vapor, and the upper end, which was sealed to the steel wall at room temperature.

The essential details of the reflection cell and the pressure vessel are given in Fig. 1. The window of the reflection cell was a truncated cone of fused quartz of high ultraviolet transparency, 10 cm. long, with polished upper and lower surfaces. The cone fitted snugly into a thin steel shell, *B*, to which it was sealed, near the top, by a Teflon packing. A coil of platinum wire embedded in refractory cement, *C*, was used to heat the reflection surface at the lower end of the quartz cone. A long tubular stem, a continuation of the steel shell, connected the space just beneath the reflecting surface with the open reservoir of mercury, *D*. Thermal insulation was provided by Alundum grain surrounding the furnace; however, the insulation was quite inefficient when the Alundum was permeated by high density gas. A copper cooling ring, *F*, helped to keep the mercury in the reservoir cool by conducting heat to the walls of the pressure vessel, which were water-cooled. The parts were assembled, as in Fig. 1(a), in a steel tube, *G*, which was placed first in a vacuum chamber for outgassing and filling with mercury, and then in the pressure vessel shown in Fig. 1(b).

The pressure vessel was designed to withstand pressures up to 1500 atm. A thick fused quartz window, *K*, was contacted to a holder by a thin film

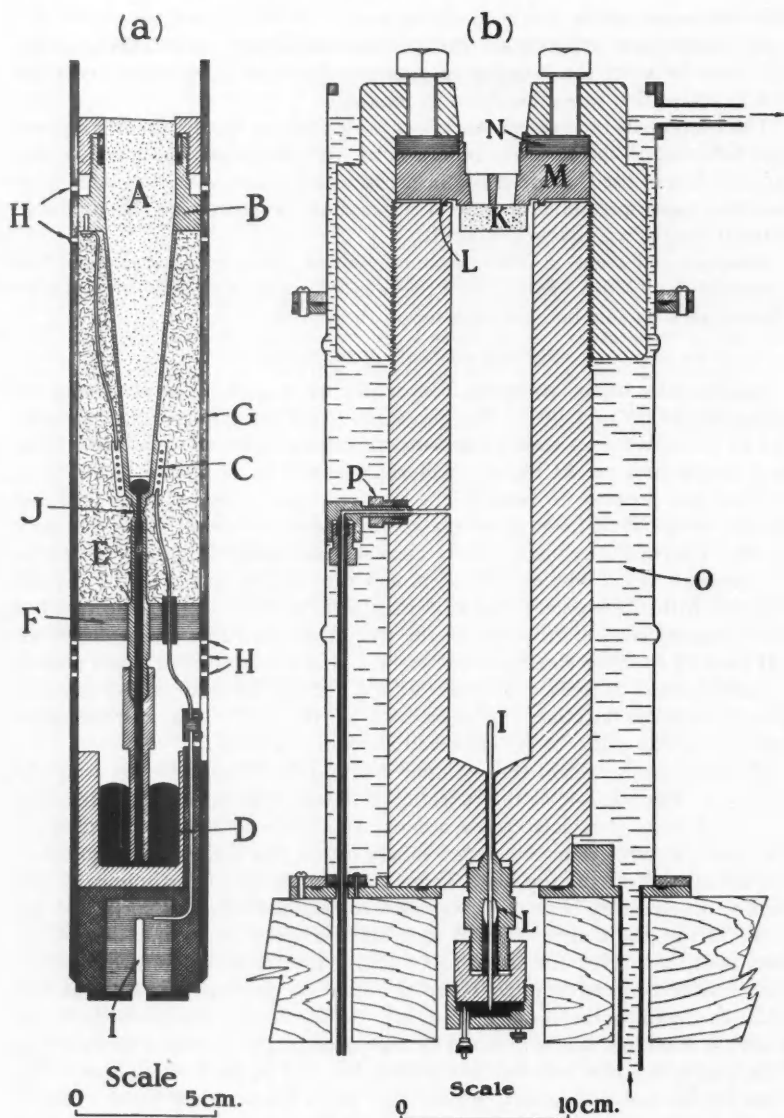


FIG. 1. Apparatus for studying selective reflection from high pressure mercury vapor: (a) reflection cell, (b) high pressure vessel. A—fused quartz cone; B—stainless steel shell; C—platinum wire furnace; D—liquid mercury; E—Alundum insulating grain; F—cooling ring; G—steel tube; H—slots to reduce heat conduction along G; I—electrical connector for furnace power; J—constriction in stem to reduce heat losses; K—pressure window; L—Teflon seal; M—window holder; N—hardened steel thrust ring; O—water bath; P—gas inlet.

of rubber cement. The free area of the window was divided into two parts to allow the light to enter and leave by separate paths. The stainless steel window holder was sealed to the body of the pressure vessel by a Teflon gasket, *L*, which was compressed by eight thrust bolts carried in a retaining cap screwed to the body of the vessel. A high current lead to convey 60-cycle power to the furnace entered the bottom of the vessel through a pressure seal with Teflon packing. Gas from a hand-operated compressor entered the vessel through 1/16 in. steel capillary tubing. Helium was used to furnish the balancing pressure notwithstanding its high thermal conductivity, since, of the gases commercially available, it had the highest ultraviolet transparency. A water bath surrounding the pressure vessel dissipated heat conducted from the furnace in order to keep the mercury reservoir cool and to protect the Teflon seals. To facilitate optical adjustments the pressure vessel was mounted on a base which permitted fine horizontal motion in two perpendicular directions.

The action of the apparatus described can now be clarified. The reflection cell, previously filled with mercury in the auxiliary vacuum chamber, remains full until sufficient heat is applied to create a vapor pressure equal to the gas pressure. The level of the liquid mercury then positions itself so that the pressure of the vapor just beneath the quartz cone is exactly balanced by the pressure of the gas, which is measured by a Bourdon gauge.

With the apparatus described it was not possible to heat the mercury much higher than 1100° C. without melting the platinum heater. An attempt was made to increase the efficiency of the furnace by introducing mercury into the cell from above, thus eliminating conduction losses in the long stem below the furnace; this gave only a slight improvement. That most of the heat losses occurred by convection and conduction in the gas was indicated by the fact that much more power was required to maintain a given temperature at high gas pressures than at lower pressures.

At temperatures above 1000° C. recrystallization of the fused quartz caused the reflection surface to deteriorate rapidly; the useful lifetime of the cell at high temperatures was therefore short and the surface required repolishing after every experiment. Another factor contributing to the difficulties of working at high temperatures was the corrosion of the steel walls of the cell by hot mercury. Small quantities of titanium and magnesium added to the mercury reduced, but did not eliminate, this difficulty. The steel shell had therefore to be renewed frequently.

A hydrogen ultraviolet continuum of the high intensity necessary for the experiments was produced by a discharge, at 3000 v. and 1 amp., between large aluminum electrodes in a water-cooled tube of fused quartz. The discharge, confined to a capillary tube 6 mm. in diameter and 50 cm. long, was viewed end-on. To stabilize the intensity of the lamp a small portion of its light was directed onto a photocell, the output of which was amplified and used to control the lamp current by means of a saturable reactor in series with the primary of the lamp transformer.

By means of a suitable arrangement of mirrors and lenses the light from

the hydrogen lamp was allowed to fall on the lower surface of the quartz cone (Fig. 1(a)) and the reflected light was directed into the spectrograph. The pressure window and the upper surface of the quartz cone were tilted slightly so that light reflected from them did not enter the spectrograph. A Hilger single prism instrument of the Littrow type was used, giving a reciprocal linear dispersion at 2537 Å of 43 cm.⁻¹/mm. In place of the usual photographic plate a detector unit, consisting of an exit slit and a 1P28 photomultiplier tube, was constructed to move along the focal plane of the spectrograph. The photomultiplier tube was coupled through a preamplifier to an electronic pen recorder.

In studying the selective reflection at 2537 Å a spectral region extending 500 cm.⁻¹ on either side of the resonance line was scanned. Silicon emission lines, present in the spectrum of the hydrogen lamp, were used for frequency calibration. At each vapor pressure several recorder traces of the selective reflection were made and averaged to give a mean observed contour. To obtain relative reflected intensities the mean contours were modified by using background traces obtained by reflection from the cold cell before the mercury was introduced.

To establish a scale of percentage reflected intensity, it was assumed that the reflectivity in the wings of the pattern approaches asymptotically a value R_0 at large distances from the resonance frequency. It was further assumed that the asymptotic reflectivity is given by $R = (n' - n_0)^2 / (n' + n_0)^2$ for perpendicular incidence, where n' is the refractive index of fused quartz and n_0 (≈ 1) is the hypothetical refractive index of the mercury vapor in the absence of anomalous dispersion at 2537 Å. The value of n_0 as a function of the density of the vapor was obtained by omitting the 2537 Å term in the dispersion equation of Wulfschön (1933). Since the ultraviolet refractive index of fused quartz has been measured only over a limited range of lower temperatures (International Critical Tables 1929), the values for high temperatures had to be obtained by extrapolation; data for the visible, which cover a larger temperature range, were used to estimate the proper trend in the extrapolation.

The calculation of N_a , the number of free mercury atoms per cubic centimeter, is complicated by the fact that in high pressure mercury vapor there is an appreciable concentration of diatomic molecules. The temperature of the vapor at the window of the reflection cell was calculated from the balancing gas pressure, P , by using the vapor pressure data of Bernhardt (1925), and the density of atoms plus molecules, N , was determined from the relation $N = P/kT$. The densities obtained in this way are probably somewhat too high because the vapor was slightly superheated. Since $N = N_a + N_m$, where N_m is the number of Hg₂ molecules per cubic centimeter, the value of N_a can be obtained only by estimating the molecular density, N_m . From the total absorption of the band system at 2540 Å, ascribed to the Van der Waals Hg₂ molecule, Kuhn (1937) determined the absolute concentration of Hg₂ molecules at a pressure of 8 mm. Hg. In this calculation he assumed that the oscillator strength, f , of the transition in the molecule is the same as in the

free atom. He then calculated the dissociation energy, D_0 , of the ground state of the molecule from the Gibson-Heitler (1928) formula for the equilibrium constant using an estimated value of the moment of inertia, I , and a vibrational frequency, ω_0 , determined from the structure of the 2341-2311 Å band system of the molecule. A reversal of this procedure was used in this investigation to estimate the molecular concentrations in the high pressure vapor. The Gibson-Heitler equation was used in the form

$$\frac{(N_a - N_m)^2}{N_m} = \frac{m^{3/2} k^{1/2} T^{1/2}}{4 \sqrt{\pi h I}} (1 - e^{-h\omega_0/kT}) e^{-D_0/kT},$$

and N_m/N_a was calculated at the various temperatures used in the selective reflection experiments by substituting Kuhn's values of ω_0 , I , and D_0 in the equation. These calculations indicated that at the highest pressure reached, 340 atm., about 35% of the atoms are combined in Hg_2 molecules.

Measurements of the selective reflection were made in the pressure range 41 to 340 atm. Accurate observations at lower pressures were precluded by the tendency of the mercury to boil violently and splash against the window. Table I summarizes the pressures used, the corresponding temperatures calculated from the vapor pressure curve of mercury, the total vapor densities expressed as N/N_0 , where N_0 is Loschmidt's number, and the corresponding atomic and molecular densities, N_a/N_0 and N_m/N_0 . The calculated values of R_0 , the asymptotic reflectivity, are also included in the table.

TABLE I

TEMPERATURE, DENSITIES, AND BACKGROUND REFLECTIVITIES FOR VARIOUS MERCURY VAPOR PRESSURES

Pressure, atm.	Temp., ° C.	Total density, N/N_0	Atomic density, N_a/N_0	Molecular density, N_m/N_0	R_0 , %
41	672	11.8	11.1	0.7	3.86
82	800	20.8	18.9	1.9	3.65
122	880	29.0	25.7	3.3	3.43
184	944	41.4	35.3	6.1	3.13
204	964	45.0	38.0	7.0	3.04
272	1016	57.7	47.6	10.1	2.75
340	1062	69.7	55.2	14.5	2.50

RESULTS AND DISCUSSION

Graphs of reflectivity as a function of wave number for several mercury vapor pressures between 41 and 340 atm. are shown in Figs. 2 and 3. At low pressures the curves follow the characteristic selective reflection pattern, which exhibits a reduced reflectivity on the low frequency side of the resonance line and a greatly increased reflectivity on the high frequency side. The main peak, which is high and narrow at low pressures, reaches a maximum intensity at about 80 atm. and then decreases somewhat irregularly in intensity with further increase in pressure; it also broadens and its frequency decreases slightly with increasing pressure. In the lower pressure contours a

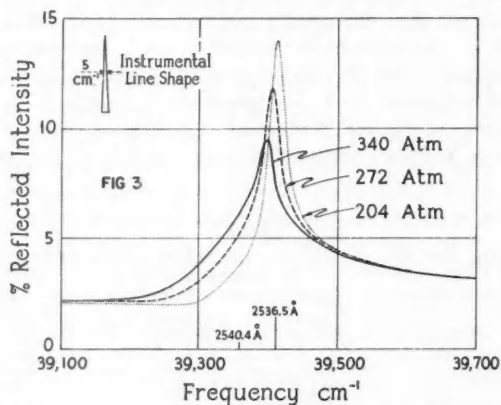
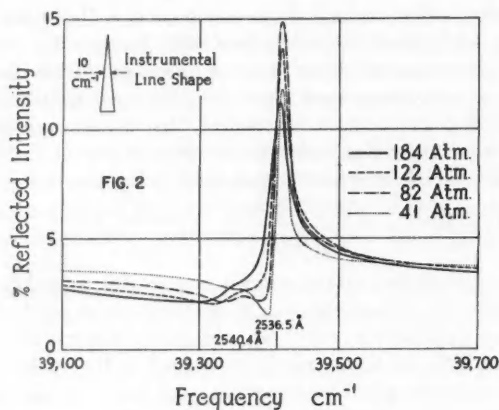


FIG. 2. Selective reflection from mercury vapor at medium pressures.

FIG. 3. Selective reflection from mercury vapor at high pressures.

weak subsidiary maximum is apparent on the low frequency side of the main peak; this increases in intensity as the pressure rises, gradually filling in the minimum of the reflection contour on the low frequency side of the resonance line.

The subsidiary maximum has a wavelength of 2540 Å and thus coincides with the maximum of the system of discrete bands which has been observed in absorption by Wood and Voss (1928), Kuhn and Freudenberg (1932), and Kuhn (1937), and in emission and absorption by Mrozowski (1949). This band system has been attributed to the transition, $0_{u}^{+} \rightarrow 1\Sigma_{g}^{+}$, in the Van der Waals molecule Hg_2 . The subsidiary maximum in the reflection pattern can therefore be ascribed with reasonable certainty to Hg_2 molecules. The presence of the molecular reflection makes the quantitative treatment of the atomic reflection more difficult, since the low frequency portion of the atomic reflec-

tion is strongly overlapped by the molecular reflection. In addition, the calculated number of free atoms, N_a , which is essential for the interpretation, can have considerable error because of the uncertainty in estimating the concentration of molecules.

The normal approach to the interpretation of experimental results on selective reflection is through the classical anomalous dispersion equations, which give the refractive index, n , and the absorption index, k , as a function of frequency, ν :

$$(1) \quad n^2 - k^2 = n_0^2 + \frac{N_a f e^2}{2\pi m \nu_0} \frac{\nu_0 - \nu}{(\nu_0 - \nu)^2 + (\gamma/4\pi)^2},$$

$$(2) \quad 2nk = \frac{N_a f e^2}{2\pi m \nu_0} \frac{(\gamma/4\pi)}{(\nu_0 - \nu)^2 + (\gamma/4\pi)^2}.$$

In these equations n_0 is the hypothetical refractive index in the absence of anomalous dispersion, ν_0 the resonance frequency of the virtual oscillator in sec^{-1} , and f the oscillator strength. The reflectivity, R , for normal incidence is given by the Fresnel relation

$$(3) \quad R = \frac{(n' - n)^2 + k^2}{(n' + n)^2 + k^2},$$

where n' is the refractive index of the bounding medium.

Several attempts were made to fit the experimental contours with reflection curves calculated from equations (1), (2), and (3) with different basic assumptions. The extensive numerical work involved was carried out with the help of the electronic digital computer of the Computation Centre, University of Toronto. The most obvious method of approach is to use the calculated values of N_a and a value of f equal to that of the free atom and to vary the damping constant, γ , until the experimental contour is well reproduced. However, no agreement between the calculated and the experimental curves could be obtained by this method; if the peak heights of the two curves were made to agree, the calculated contour was always much broader than the experimental contour. It became apparent that a satisfactory reproduction of the experimental curves could be obtained only by using $N_a f$ in addition to γ as a parameter in the curve fitting. Examples of the agreement obtained at various vapor pressures are shown in Fig. 4 and the values of $N_a f$ and γ are listed in Table II. It will be noted that the fitting had

TABLE II
OPTICAL CONSTANTS DERIVED FROM THE REFLECTION CONTOURS OF Hg 2537

Pressure, atm.	$N_a f$, cm^{-2}	γ , sec^{-1}	f	Frequency shift, $\nu_0 - \nu_0'$, cm^{-1}
41	4.0×10^{18}	1.3×10^{12}	0.013	2
82	8.3	2.5	0.016	6
122	11.0	3.6	0.016	10
184	13.0	4.8	0.014	13
204	14.0	4.0	0.014	15
272	17.0	5.4	0.013	23
340	20.0	7.3	0.013	33

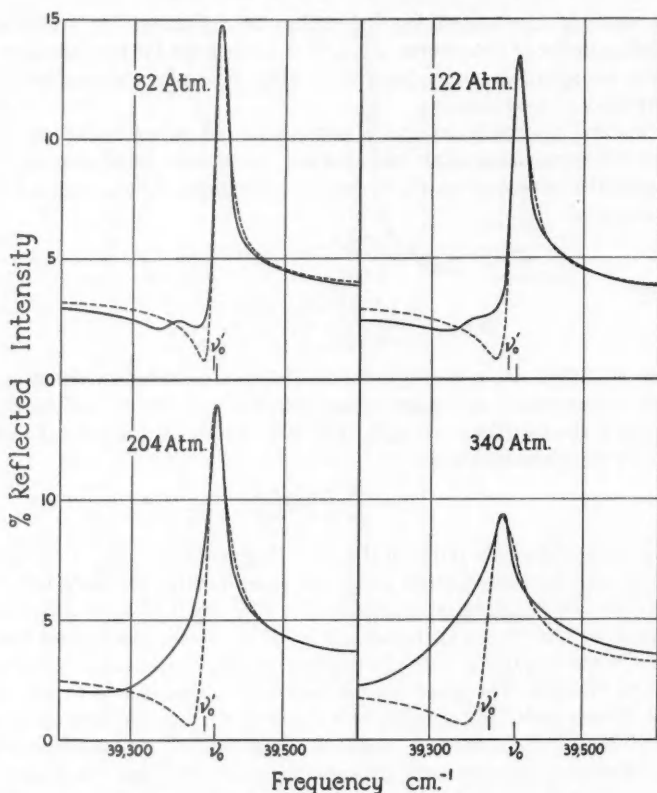


FIG. 4. Comparison of calculated selective reflection curves (dashed) with experimental curves.

to be confined, in general, to the maximum and high frequency wing of the pattern because of the molecular reflection in the low frequency wing. No significance should be attached to the smaller discrepancies in curve fitting since these can be attributed to errors in estimating the background intensity.

In Fig. 5 the values of γ obtained from the curve-fitting procedure are plotted against the relative density of atoms, N_a/N_0 . The experimental points for the four lowest pressures were determined by averaging curves from three separate experiments while the points for the three highest pressures were obtained from a single experiment. The points define fairly accurately a straight line through the origin, indicating that the damping constant is proportional to the density. From the slope of the straight line in Fig. 5 a damping coefficient $\gamma/N_a = 4.8 \times 10^{-9} \text{ sec.}^{-1} \text{ cm.}^3$ is obtained. There seem to be no data available on the broadening of the 2537 Å line in emission or absorption in pure mercury vapor which can be used to calculate a broadening

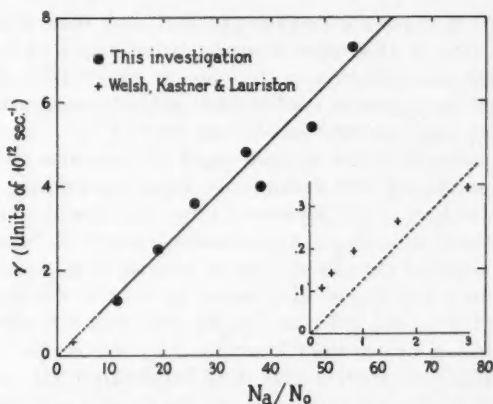


FIG. 5. Variation of the damping constant, γ , with density. In the insert the values of γ determined by Welsh *et al.* (1950) are shown on an expanded scale.

coefficient for comparison. However, Weisskopf (1933) has derived the theoretical formula, $\Delta\nu_{1/2} = (e^2 f / 2\pi m \nu_0) N_a$, for the half width of a spectral line broadened by collisions between similar atoms. Since $\Delta\nu_{1/2} = \gamma / 2\pi$, the formula gives $\gamma / N_a = e^2 f / m \nu_0$ for the damping coefficient. If the f value is taken as 0.0267, the theoretical damping coefficient is $5.7 \times 10^{-9} \text{ sec}^{-1} \text{ cm}^3$, in fair agreement with the value obtained from the selective reflection data.

The Weisskopf formula was derived on the basis of an impact theory involving the dipole interaction of similar atoms; the statistical theory of Margenau and Watson (1936) yields essentially the same formula. In these theories the damping coefficient, γ / N_a , is independent of the temperature. The classical collision theory of Lorentz, on the other hand, leads to a temperature dependence of the damping coefficient as given by the formula $\gamma / N_a = 8\rho^2 \sqrt{(\pi k T / \mu)}$, where μ is the mass of the atom and ρ the "optical collision diameter". Thus, in the Lorentz theory $\gamma / N_a \sqrt{T}$, rather than γ / N_a , is constant. Since the selective reflection data have considerable experimental error and are confined to the interval 945° K. to 1335° K. , it is not possible to say for certain which of the theories is in better accord with experiment; the evidence is, however, slightly in favor of a temperature-independent broadening coefficient. It is of interest to note that the collision diameter calculated from the Lorentz formula is 12.2 \AA .

In the curve-fitting procedure outlined above, the product $N_a f$ was treated as a parameter rather than as a known quantity. If the values of $N_a f$ thus determined are divided by the corresponding calculated values of N_a , the f numbers listed in Table II are obtained. The results show that for all the pressures used in the experiments the oscillator strength is of the order of one half of the value, 0.0267, for the free atom. If the value for 41 atm., which appears to be in error, is disregarded, the f value shows a systematic decrease with increasing pressure; it appears to decrease from the "free atom" value

fairly rapidly in the pressure range 0–150 atm. and then more slowly. To establish the reality of this trend it would be necessary to make a careful study of the selective reflection in the pressure range up to 50 atm.; with the experimental arrangement used in the present investigation this study was unfortunately not possible.

It cannot be affirmed that a dependence of the oscillator strength on density has been established with certainty in these experiments. Nevertheless, a careful consideration of the sources of error indicates that the conclusion is at least qualitatively correct. An overestimation of N_a because of superheating of the vapor at the cell window or because of an underestimation of N_m could lead to a lowering of the f value, but not to the extent observed. Overlapping of the atomic reflection by the molecular reflection would have the effect of raising rather than lowering the f value. The calculation of N_m rests on Kuhn's assumption that the f value in the Hg_2 molecule is the same as for the atomic transition. If, on the other hand, the molecular f value is lower than that of the free atom, as is indicated by the density dependence found in this investigation, the f value determined from the selective reflection would be still further lowered.

There appears to be no theoretical evidence for or against a pressure dependence of the oscillator strength. A theoretical treatment of the variation of f at high densities has been given by Möglich and Rompe (1942), but the results are not stated in a form which can be applied to the present case. There is no reliable experimental evidence that atomic transition probabilities are changed by foreign gases at high pressures; this question has been discussed in some detail by Kuhn (1937). Also, it will be shown in a later publication that very high pressures of foreign gases do not alter the oscillator strength determined from selective reflection (Galt and Welsh 1957). However, it can be argued that like atoms at high densities might exhibit changes in the f values of electronic transitions if coupling effects are present. Because of the high opacity of mercury vapor in the region of its resonance line, it would be very difficult to establish by absorption measurements that the f value decreases. It is, in fact, one of the advantages of the reflection method that optical constants can be determined in many cases which would be inaccessible to observation by the more conventional transmission methods.

In fitting a calculated reflection curve to the experimental curve at a given pressure, it was found that the resonance frequency ν_0' of the calculated curve did not coincide with the frequency ν_0 of the Hg 2537 line. The frequencies ν_0 and ν_0' are marked on the graphs of Fig. 4 and the frequency shifts $\nu_0' - \nu_0$, tabulated in Table II, are plotted as a function of $N_a f$ in Fig. 6. A shift of the resonance frequency caused by coupling of atoms has been predicted by Weisskopf (1933); the coupling shift, which is proportional to $N_a f$ (Born 1933), is plotted as a dashed line in Fig. 6. At low densities the experimental curve approaches the Weisskopf curve asymptotically but at higher densities there is a large deviation. The frequency shifts are well represented by a relation of the form $\nu_0' - \nu_0 = aN_a + bN_a^2$, where the linear term represents the Weisskopf coupling shifts. However, there seems to be no theoretical interpretation of the term in N_a^2 .

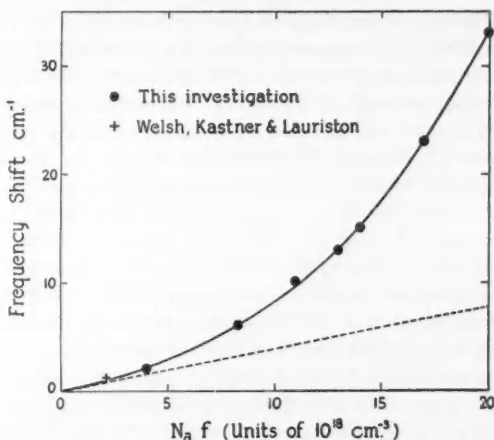


FIG. 6. Shift of the resonance frequency, $\nu_0 - \nu'_0$, as a function of $N_a f$.

An attempt was made to calculate the effect of the molecular reflection with dispersion equations involving two separate resonance terms, one for the 2537 Å line and one for the 2540 Å line. At pressures up to 82 atm. this method could be made to account for the shape of the molecular reflection with fair accuracy but at higher pressures it was totally inadequate. It appears that the molecular band of frequencies can not be accurately represented by a single frequency in the dispersion formula.

The conclusions reached in the high pressure experiments differ radically from those of Welsh, Kastner, and Lauriston (1950) and of Lauriston and Welsh (1951) at lower pressures; a critical reconsideration of these earlier experiments was therefore undertaken. In particular, the validity of the relation $\gamma \propto \sqrt{N_a}$, which was believed to be established at low pressures, now appears questionable. The values of γ determined by Welsh, Kastner, and Lauriston in the pressure range 1/2 to 8 atm. are plotted on an expanded scale in Fig. 5, which also shows the straight line determined in the present investigation. The highest pressure points are in reasonable agreement with the straight line relation but the low pressure points all lie considerably above the line. It is believed that the discrepancy can be attributed to two independent sources of error, each of which would tend to increase the values of γ assigned at the lower pressures without greatly affecting the higher pressure values. The first source of error concerns the slit width corrections which were applied to the calculated curves before they were compared with the experimental curves. The correction which was applied assumed a spectral slit width of 1.0 cm^{-1} , a value determined from the geometry of the spectrograph. It has since been established (St. John 1952) that aberrations in the optics of this spectrograph impose a lower limit of 1.4 cm^{-1} on the spectral slit width which can be realized in practice. The second source of error resulted from the assumption that the resonance line could be represented by a single frequency, ν_0 . However, the separation of the extreme

hyperfine components of the 2537 Å line is about 0.7 cm^{-1} (Schüler and Keyston 1931), which is an appreciable fraction of the width of the reflection pattern. In fact, the experimental curve of Cojan (1954) obtained with resolving power high enough to show the individual hyperfine components is only one third as wide as the curve of Welsh *et al.* taken at approximately the same pressure ($1/2 \text{ atm.}$). To determine whether these two sources of error could adequately explain the apparent deviation from the $\gamma \propto N$ law at low pressures, selective reflection curves were calculated using the anomalous dispersion equations involving terms for five separate resonance frequencies. The numerical value of $N_a f$ was divided among the five individual hyperfine components in proportion to the relative intensities of lines as determined by Schüler and Keyston. The curves so calculated were modified for a slit width of 1.4 cm^{-1} and compared with the experimental curve. The best agreement of the calculated curve with the experimental curve was obtained with a damping constant smaller than that originally assigned and in good agreement with the $\gamma \propto N_a$ relation. It is therefore concluded that the measurements of Welsh, Kastner, and Lauriston are not in disagreement with the present results. A re-examination of the selective reflection curves in the neighborhood of the 2288 Å line of cadmium, obtained by Welsh, Kastner, and Lauriston, also indicates the validity of the $\gamma \propto N_a$ relation; the results of these calculations are given in Appendix II.

APPENDIX I. SELECTIVE REFLECTION FROM MERCURY VAPOR AT 1850 Å

A preliminary investigation of selective reflection in the neighborhood of the 1850 Å resonance line of mercury was made for pressures up to 4.4 atm. The mercury was contained in a sealed fused quartz reflection cell and the vapor pressure estimated from the temperature of a side tube containing liquid mercury. Light from a low voltage hydrogen arc was reflected from the

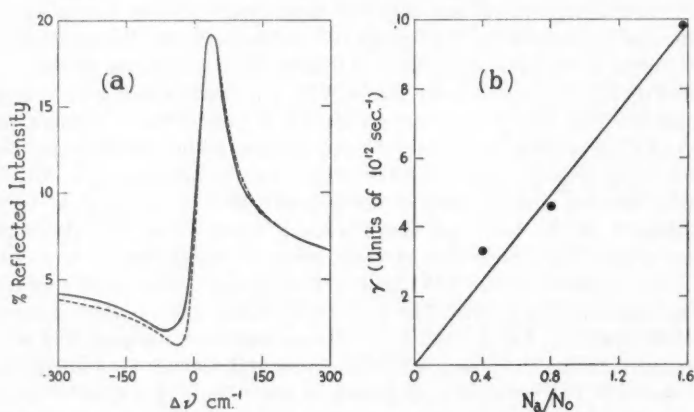


FIG. 7. Selective reflection from mercury vapor at Hg 1850: (a) comparison of calculated contour (dashed) with the experimental curve for 4.4 atm., (b) variation of the damping constant with density.

inner surface of the cell window into a fluorite spectrograph, and the entire optical path was evacuated to eliminate atmospheric absorption. Oil sensitized photographic plates, Kodak 103a0 U.V., were calibrated for intensity measurements by a series of six exposures of equal duration taken through wire screens of various mesh sizes.

The selective reflection contour for a pressure of 4.4 atm. is shown in Fig. 7(a). The large extent of the region of selective reflection even at this comparatively low pressure is a consequence of the high oscillator strength of the 1850 Å resonance line. Theoretical curves were calculated to fit the experimental curves for pressures of 4.4, 2.2, and 1 atm. In each case the value of f used was 1.16, as determined by Wolfsohn (1933) from refractive index measurements. The very satisfactory agreement between the calculated and experimental curves is illustrated in Fig. 7(a). The values of γ determined from the curve fitting are plotted against the density, N_a/N_0 , in Fig. 7(b). The relation $\gamma \propto N_a$ is adequately confirmed.

APPENDIX II. SELECTIVE REFLECTION FROM THE VAPORS OF CADMIUM AND THE ALKALI METALS

Selective reflection in the neighborhood of the cadmium resonance line at 2288 Å was investigated by Welsh, Kastner, and Lauriston (1950) for pressures up to 14.7 atm. They stated that their results confirmed the $\gamma \propto \sqrt{N_a}$ relation found for the Hg 2537 line, but noted a marked discrepancy between their calculated and experimental contours at higher vapor pressures. With the improved computation facilities now available a new analysis of the data on the cadmium selective reflection was undertaken.

The experimental contours, obtained by Welsh *et al.* for cadmium vapor pressures of 5.4 and 14.7 atm., were fitted by calculated curves. The oscillator strength, f , was given the value 1.38, as determined by the earlier authors at lower pressures, and only the value of γ was varied in the curve-fitting procedure. In Fig. 8(a) the calculated contour for 14.7 atm. is compared with the experimental curve. The fit is fairly satisfactory and could be improved if the experimental curve were rotated slightly; this would merely indicate an error in estimating the original background intensity contour. The recalculated values of γ are plotted in Fig. 8(b), along with the values assigned by the earlier authors. It can be seen that a linear dependence of γ on N_a represents the data much better than a square root dependence. It is possible that the values of γ at low densities are spuriously high because of inadequate slit width correction but there is no direct evidence to show that this is so. Since the higher vapor densities in these measurements were rather uncertain it was not considered worth while to try to establish, by more refined calculations, a possible variation of the f value with density.

The selective reflection from the alkali metal vapors was considered by Lauriston and Welsh (1951) to support the relation $\gamma \propto \sqrt{N_a}$, although here also discrepancies were observed at higher pressures. In these experiments the vapor densities were deduced from the experimental reflectivity curves and, for this reason, it does not seem worth while to attempt a new analysis. For both sodium and potassium vapors the reflection maxima decreased in

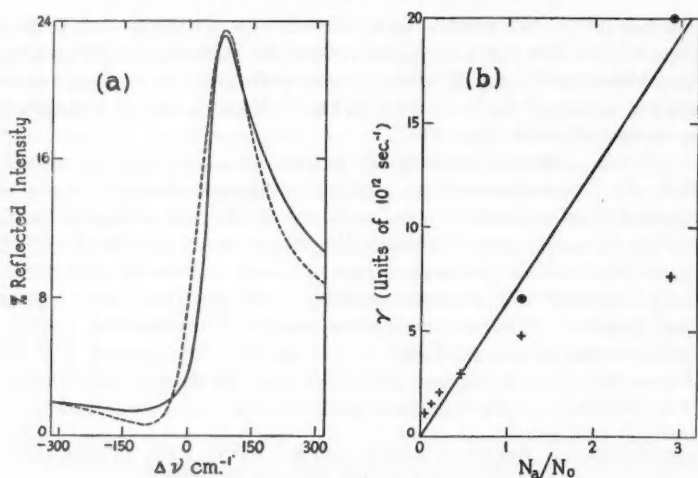


FIG. 8. Selective reflection from cadmium vapor at Cd 2288: (a) comparison of calculated contour (dashed) with the experimental curve for 14.7 atm., (b) variation of the damping constant with density (+ Welsh, Kastner, and Lauriston (1950), ● recalculated values).

intensity at the highest vapor pressures; this behavior is in accordance with the $\gamma \propto N_a$ relation but not with the $\gamma \propto \sqrt{N_a}$ relation.

The formula $\Delta\nu_{1/2} = (e^2/2\pi m\nu_0)N_a$, derived by Weisskopf (1933) and by Margenau and Watson (1936) for collision broadening by like atoms, indicates that the ratio $\gamma\nu_0/N_af$ should be a constant for all spectral lines. A verification of this conclusion by measurements of half-widths of absorption lines is difficult, but the selective reflection data for Hg 2537, Hg 1850, and Cd 2288 can be used as a qualitative check. These data are summarized in Table III. Since, for these lines, the ratio $\gamma\nu_0/N_af$ varies by a factor of two at most, although the f values differ by factors up to 100, it is concluded that

TABLE III
VALUES OF $\gamma\nu_0/N_af$ AND ρ FROM SELECTIVE REFLECTION DATA

Line	f value*	γ/N_a , $\text{cm}^2 \text{ sec}^{-1}$	$\gamma\nu_0/N_af$, $\text{cm}^2 \text{ sec}^{-2}$	ρ , Å
Hg 2537	$\begin{cases} 0.0267 \\ 0.014^* \end{cases}$	$\begin{cases} 0.48 \times 10^{-8} \\ 0.48 \end{cases}$	$\begin{cases} 2.1 \times 10^7 \\ 4.0 \end{cases}$	12
Hg 1850	1.16	2.3	3.2	32
Cd 2288	1.38*	2.4	2.3	24

*The f values marked with an asterisk were determined from selective reflection.

the formula of Weisskopf is at least qualitatively correct. In the last column of Table III collision cross-sections, ρ , calculated from the Lorentz formula, are tabulated. The large cross-sections calculated for Hg 1850 and Cd 2288 as compared with Hg 2537 illustrate the lack of physical reality of the Lorentz

collision theory as applied to broadening by similar atoms. On the other hand, the large broadening coefficient for lines with high oscillator strengths is a natural consequence of the dipole interaction theory of Weisskopf and of the statistical theory of Margenau and Watson.

ACKNOWLEDGMENTS

The authors are indebted to the National Research Council of Canada for the financial assistance which made this research possible, to Professor W. H. Watson, Director of the Computation Centre, University of Toronto, for the use of computation facilities, and to Professors C. C. Gotlieb and J. N. P. Hume for advice on computation matters.

REFERENCES

- BERNHARDT, F. 1925. *Physik. Z.* **26**, 265.
BORN, M. 1933. *Optik* (Verlag von Julius Springer, Berlin).
COJAN, J. L. 1954. *Ann. phys.* (12), **9**, 385.
GALT, J. A. and WELSH, H. L. 1957. *Can. J. Phys.* **35**, 114.
GIBSON, G. E. and HEITLER, W. 1928. *Z. Physik*, **49**, 465.
International Critical Tables. 1929. Vol. 6 (McGraw-Hill Book Company, Inc., New York), p. 342.
KUHN, H. 1937. *Proc. Roy. Soc. (London)*, A, **158**, 212, 230.
KUHN, H. and FREUDENBERG, K. 1932. *Z. Physik*, **76**, 38.
LAURISTON, A. C. and WELSH, H. L. 1951. *Can. J. Phys.* **29**, 217.
MARGENAU, H. and WATSON, W. W. 1936. *Revs. Mod. Phys.* **8**, 22.
MÖGLICH, F. and ROMPE, R. 1942. *Z. Physik*, **120**, 741.
MROZOWSKI, S. 1949. *Phys. Rev.* **76**, 1714.
SCHÜLER, H. and KEYSTON, J. E. 1931. *Z. Physik*, **72**, 423.
ST. JOHN, G. E. 1952. Ph.D. Thesis, University of Toronto, Toronto, Ont.
WEISSKOPF, V. 1933. *Physik. Z.* **34**, 1.
WELSH, H. L., KASTNER, J., and LAURISTON, A. C. 1950. *Can. J. Research*, A, **28**, 93.
WOLFSOHN, G. 1933. *Z. Physik*, **83**, 234.
WOOD, R. W. 1909. *Phil. Mag.* **18**, 187.
WOOD, R. W. and VOSS, V. 1928. *Proc. Roy. Soc. (London)*, A, **119**, 698.

INFLUENCE OF FOREIGN GASES AT HIGH PRESSURES ON THE SELECTIVE REFLECTION FROM MERCURY VAPOR¹

J. A. GALT² AND H. L. WELSH

ABSTRACT

The influence of the foreign gases hydrogen, helium, nitrogen, and argon on the selective reflection from mercury vapor at 2537 Å was studied at pressures up to 1500 atm. The results were interpreted on the basis of the classical theory of reflection from an absorbing medium. The damping constant was found to vary linearly with foreign gas density as predicted by collision broadening theory. Frequency shifts and collision diameters determined from selective reflection data agree fairly well with values measured in absorption by other workers.

INTRODUCTION

Selective reflection of light from high pressure mercury vapor in the neighborhood of the resonance line, 2537 Å, has been studied by Galt and Welsh (1957). It was shown that the reflection contours could be interpreted in terms of the classical theory of reflection from an absorbing medium. In particular, the damping constant, γ , was found to be proportional to the number of atoms, N_a , per cubic centimeter; however, the oscillator strength, f , which had to be assigned to the line in the high pressure vapor, is markedly smaller than the accepted value for the free atom. The variation of the damping constant, $\gamma \propto N_a$, in selective reflection is in accordance with most theoretical treatments of collision damping in emission and absorption. However, no comparison of the selective reflection data with absorption data is possible because the high absorption index of the resonance line makes quantitative absorption measurements difficult even at low pressures. On the other hand the influence of foreign gases on the absorption line can be studied even at high pressures. Thus the absorption of mercury vapor at 2537 Å was studied by Füchtbauer, Joos, and Dinkelacker (1923) in the presence of foreign gases at pressures up to 50 atm. More recently, Robin and Robin (1951) and Robin (1954) have investigated the same absorption line with foreign gas pressures as high as 1500 atm. A direct comparison of the effects of foreign gases in absorption and in selective reflection is therefore possible.

The influence of foreign gases on the selective reflection from mercury vapor at 2537 Å was studied by Schnettler (1930), who measured the intensity of the resonance line from a mercury arc after it had been reflected from a quartz-mercury vapor interface. Since only a slight reduction in intensity was observed for foreign gas pressures up to 15 atm., Schnettler concluded that, unlike the case of resonance radiation, the mean lifetime of the excited atom plays no role in selective reflection; this conclusion was later confirmed more directly by Hansen and Webb (1947). The slight decrease in intensity at high pressures observed by Schnettler could be inter-

¹Manuscript received August 31, 1956.

Contribution from the McLennan Laboratory, University of Toronto, Toronto, Ontario. This research was supported by a grant from the National Research Council of Canada.

²Holder of National Research Council Scholarships, 1950-53. Present address: Research Centre, Du Pont Company of Canada Limited, Kingston, Ontario.

preted as a diminution of the absorption index at the resonance frequency by collision broadening of the line. Since nearly monochromatic light was used for observing the selective reflection, no measurement of the damping constant was possible.

In the present investigation, light of continuous spectral distribution was used to study the effect of foreign gases at pressures up to 1500 atm. on the selective reflection at 2537 Å. With an adaptation of the apparatus used for pure mercury vapor at high pressures, the intensity contour of the selective reflection was studied as a function of foreign gas pressure.

EXPERIMENTAL PROCEDURE

The reflection cell, the detail of which is shown in Fig. 1, was a modification of the cell used for pure mercury vapor, and was operated in the same pressure

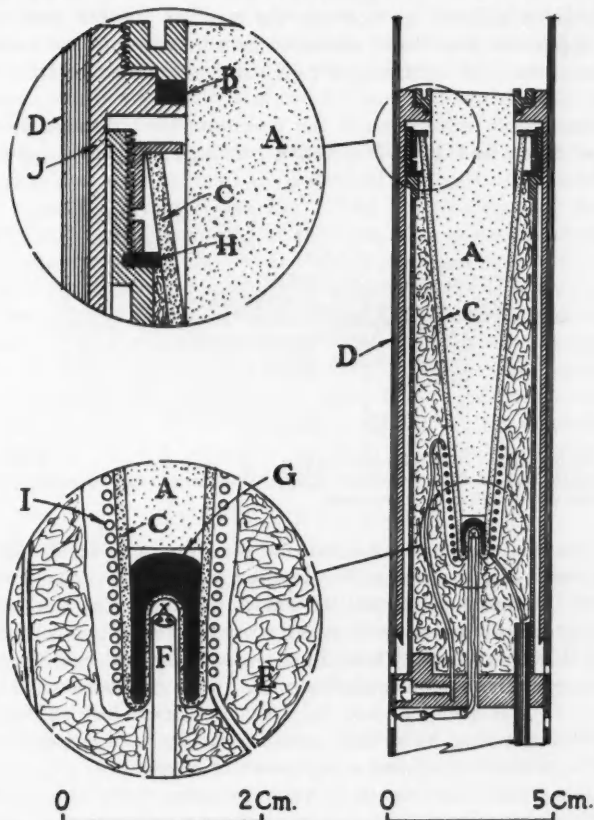


FIG. 1. Reflection cell for the study of selective reflection from mixtures of mercury vapor and foreign gases. A—fused quartz cone; B—Teflon packing; C—fused quartz shell; D—steel tube; E—Alundum insulating grain; F—porcelain insulator for thermocouple wires; G—liquid mercury; H—Teflon seat for C; I—platinum wire furnace; J—supporting tube for A.

vessel with the same optical arrangement (Galt and Welsh 1957). The shell, *C*, surrounding the conical fused quartz window was made of fused quartz rather than of steel since, in this case, it need not be impermeable to gas. Liquid mercury filled the lower end of the shell to within one millimeter of the reflecting surface. A channel formed by a narrow flat strip ground on the solid quartz cone allowed gas to enter the space between the window and the mercury meniscus to mix with the mercury vapor. The mercury and the lower end of the conical window were heated to temperatures between 650° C. and 750° C. by a coil of platinum wire embedded in refractory cement. To measure the temperature of the mercury pool, a Pt: Pt-Rh thermocouple was inserted into a small re-entrant tube in the bottom of the fused quartz shell. The space surrounding the outer cone was filled with Alundum grain for thermal insulation. The solid cone was fastened to a metal sleeve, *J*, and could be easily withdrawn to replenish the mercury without disturbing the rest of the apparatus. This sleeve also served as a labyrinth to prevent mercury vapor diffusing into the light path between the quartz cone and the pressure window.

The thermocouple wires entered the pressure vessel through two glands of the type shown in Fig. 2. The Teflon packing, *B*, forms a pressure seal

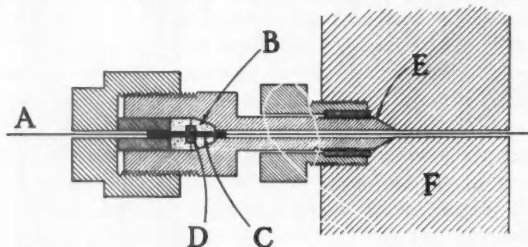


FIG. 2. High pressure thermocouple lead-in. *A*—platinum wire; *B*—Teflon packing; *C*—steel capillary tube hard soldered to *A*; *D*—collar soldered to *C*; *E*—conventional cone-type pressure seal; *F*—wall of pressure vessel.

and also provides electrical insulation for the wire, *A*. The lead should, of course, be continuous in passing through the pressure wall to avoid a spurious e.m.f. in the thermocouple circuit. However, platinum wire by itself is too soft to withstand the pinching-off effect when the packing is compressed. It was found that a satisfactory seal could be made by soldering the platinum wire into a piece of fine steel capillary, *C*. To give added support a small steel collar, *D*, was soldered onto the steel capillary. Electrical lead-ins employing Teflon packing have been used frequently in this laboratory, and appear to be quite reliable even at a pressure of 5000 atm.

In contrast to the experiments with pure mercury vapor at high pressures, the foreign gas experiments were relatively easy to perform. The reflectivity curves were more self-consistent than those for pure mercury vapor because the complete sequence of curves was obtained without dismantling the

apparatus. Also, because of the lower temperatures used, there was no deterioration of the reflecting surface due to recrystallization of the silica. During an experiment the temperature of the liquid mercury was held constant to give a vapor pressure in the range 40 to 70 atm., and the total pressure applied by the foreign gas, as measured on a Bourdon gauge on the gas compressor, was varied between 100 and 1500 atm. The partial pressure of the mercury was taken to be the vapor pressure, calculated from the data of Bernhardt (1925), at the temperature indicated by the thermocouple, and any change in vapor pressure caused by the presence of the gas was neglected. The temperature shown by the thermocouple was used to calculate also the foreign gas densities, although radiation pyrometer measurements indicated that the temperature of the reflecting surface was somewhat higher. The densities for hydrogen were obtained by extrapolating the isothermal data of Michels and Goudekot (1941), and for helium by extrapolating the straight line relationship for the temperature variation of the second virial coefficient given by Schneider and Duffie (1949). The estimated high temperature virial coefficients given in Circular 564 of the National Bureau of Standards (1955) were used for nitrogen and argon.

Intensity traces of the selective reflection were obtained with the recording spectrograph and were reduced by a method similar to that used for pure mercury vapor (Galt and Welsh 1957). The determination of the absolute reflectivity was complicated by the presence of a gas with an appreciable index of refraction in contact with the window. The contributions to the refractive index, $n_g - 1$, from the foreign gas, and $n_v - 1$, from the mercury vapor, were calculated separately from the partial densities and added. At the highest pressure the presence of the gas decreased the background reflectivity, R_0 , from 4% to 3% for argon and nitrogen; for hydrogen and helium the decrease was much smaller. Most of the experiments were carried out with the liquid mercury at a temperature of 685°C., for which the relative density, N_g/N_0 (N_0 = Loschmidt's number), of the vapor was 12. The relative densities of the foreign gas, N_g/N_0 , ranged from 15 to 180.

RESULTS AND DISCUSSION

Examples of the changes in the selective reflection from mercury vapor produced by the addition of foreign gases at high pressures are shown in Figs. 3 and 4. The predominant effect is a lowering of the maximum of the reflection contour, which tends to obliterate the pattern at the highest pressures. A weak subsidiary maximum is observed at 2540 Å on the curves for the lower pressures; this maximum has been previously interpreted in terms of Hg₂ molecules (Galt and Welsh 1957).

The main features of the experimental reflection contours can be explained satisfactorily by the classical theory of anomalous dispersion. With the facilities of the Computation Centre, University of Toronto, theoretical curves were calculated to fit the experimental curves using a procedure similar to that employed for pure mercury vapor. For the oscillator strength, f , the value 0.0267 for the free atom was used, and the number of atoms per

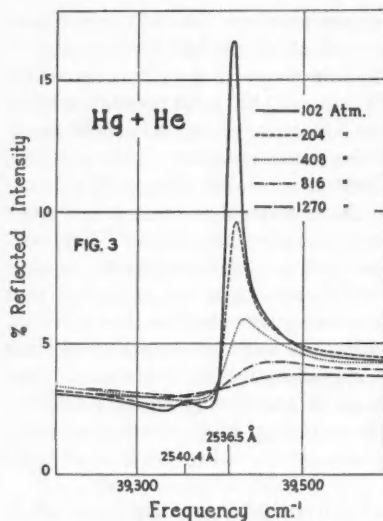


FIG. 3. Selective reflection from mixtures of mercury vapor and helium at various total pressures.

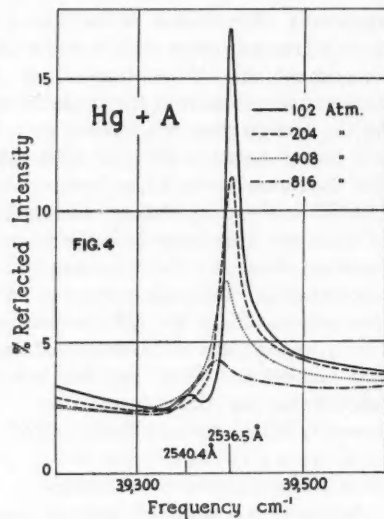


FIG. 4. Selective reflection from mixtures of mercury vapor and argon at various total pressures.

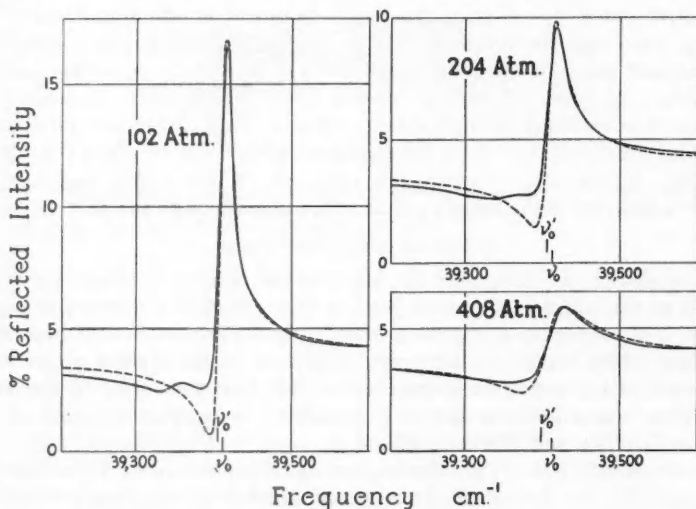


FIG. 5. Comparison of calculated (dashed curve) and experimental reflection curves for mixtures of mercury vapor and helium.

cubic centimeter, N_a , was calculated as outlined by Galt and Welsh (1957). The damping constant, γ , was determined from the best agreement of the calculated reflection curves with the experimental curves, using a trial and

error procedure. The calculated curves for the lowest pressures were modified slightly to correct for the instrumental line shape of the spectrograph before they were compared with the experimental curves. Fig. 5 shows some of the theoretical curves for helium as foreign gas and the experimental curves to which they correspond. The fit is poor on the low frequency side because of the Hg_2 reflection which could not be allowed for in the calculations. The agreement between the calculated and experimental curves for the other foreign gases was similar to that shown for helium. In most cases the calculations were confined to the lower part of the pressure range since the reflection patterns at the highest pressures were comparatively poorly defined (Figs. 3 and 4).

The values of γ obtained from the curve-fitting procedure are plotted in Fig. 6 as a function of the relative density, N_g/N_0 , of the foreign gas. In-

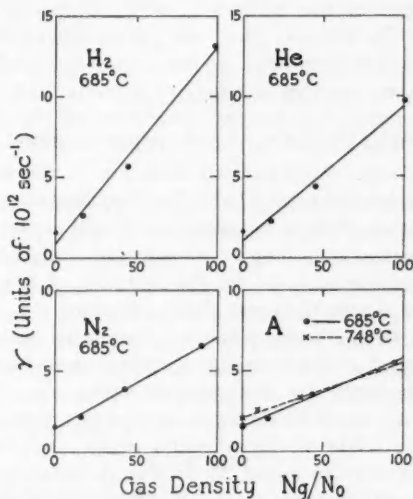


FIG. 6. Variation of the damping constant, γ , with density for the various foreign gases.

cluded in the plots are the values of γ for $N_g = 0$, calculated from the damping coefficient, $\gamma/N_g = 4.8 \times 10^{-9} \text{ cm}^3 \text{ sec}^{-1}$, for pure mercury vapor (Galt and Welsh 1957). In all cases γ increases linearly with N_g so that a damping coefficient, γ/N_g , can be determined for each foreign gas; these are listed in Table I.

The optical collision diameter, ρ , which can be considered as an indication of the average extent of the intermolecular forces, can be derived from the slope of the lines in Fig. 6 by means of the relation

$$\rho^2 = \frac{\gamma}{4N_g} \sqrt{\frac{\mu}{2\pi kT}},$$

where μ is the reduced mass of the mercury atom and the foreign gas molecule (Weisskopf 1933). In Table I the values of ρ obtained from the selective

TABLE I
DAMPING COEFFICIENTS AND COLLISION DIAMETERS FOR Hg 2537

Foreign gas	Selective reflection		Absorption
	Damping coefficient, γ/N_g , cm. ² sec. ⁻¹ $\times 10^9$	Collision diameter, Å	Collision diameter, Å
H ₂	4.47 (685° C.)	4.7	{ 5.3*
He	3.09 (685° C.)	4.6	{ 4.7†
N ₂	2.11 (685° C.)	6.1	{ 5.4†
A	{ 1.57 (685° C.)	{ 5.7	{ 8.1*
	{ 1.25 (748° C.)	{ 5.0	{ 9.4*

*Calculated from the data of Füchtbauer, Joos, and Dinkelacker (1923).

†Calculated from the data of Robin (1954).

reflection measurements are compared with values calculated from the absorption data of Füchtbauer, Joos, and Dinkelacker (1923) and of Robin (1954). The agreement, although not good, can be considered satisfactory evidence that damping in selective reflection is produced by the same collision processes that are responsible for the broadening of the absorption line.

One experiment was carried out at a higher temperature, 748° C., with argon as the foreign gas. As is evident from Fig. 6, the damping coefficient and hence the collision diameter (Table I) is smaller at the higher temperature. This temperature effect is not what one would expect and may perhaps be spurious. The matter could not be investigated further because the experiments were abruptly terminated by the bursting of the pressure window and the destruction of essential parts of the apparatus.

As the pressure of the foreign gas increases, the peak of the reflection shifts towards higher frequencies for hydrogen and helium (Fig. 3) and towards lower frequencies for nitrogen and argon (Fig. 4). However, when theoretical curves are fitted to the experimental contours, it is seen that the displacement of the *origin* of the reflection pattern, ν_0' , from the frequency of the unperturbed resonance line, ν_0 , is always towards lower frequencies. For nitrogen and argon the shift, $\nu_0 - \nu_0'$, is a linear function of the gas density (Fig. 7). For hydrogen and helium the shifts appear to increase more rapidly than linearly at the higher densities. The shifts for hydrogen, argon, and nitrogen are in the same direction and of the same order of magnitude as the frequency shifts of the maximum of the absorption line, as measured by Füchtbauer, Joos, and Dinkelacker (1923). The shift observed with helium as foreign gas is in the direction opposite to that observed by Robin (1954) for the absorption line; however, the absorption measurements may be complicated by the presence of HgHe molecules, which do not seem to be present to any extent at the high temperature used in the reflection experiments.

The effect of foreign gases at high pressures on the selective reflection from mercury can thus be interpreted in a straightforward way in terms of collision damping. The main difference between the results with foreign gases and

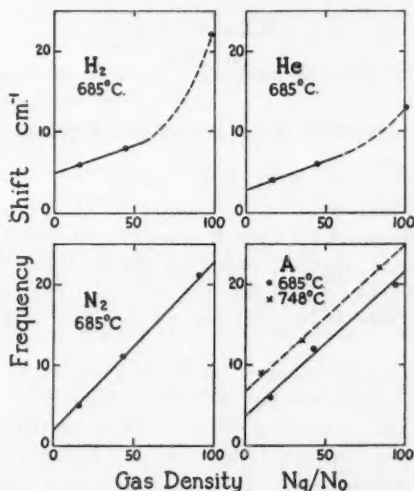


FIG. 7. Shift of the resonance frequency, $\nu_0 - \nu_0'$, as a function of gas density for the various foreign gases.

the results with pure mercury vapor at high pressures is that, for the former, the oscillator strength is that of the free atom while, for the latter, an oscillator strength decreasing with increasing mercury vapor pressure must be assumed. This effect in pure mercury vapor must be a consequence of coupling of the mercury atoms, and it appears that the coupling is not present when foreign gases at 100 atm. or more are mixed with the vapor. The range of foreign gas pressures up to 100 atm., which could not be investigated in the present apparatus, should show effects indicative of the decoupling of the mercury atoms with increasing foreign gas pressure.

REFERENCES

- BERNHARDT, F. 1925. *Physik. Z.* **26**, 265.
 FÜCHTBAUER, C., JOOS, G., and DINKELACKER, O. 1923. *Ann. Physik*, **71**, 204.
 GALT, J. A. and WELSH, H. L. 1957. *Can. J. Phys.* **35**, 98.
 HANSEN, J. M. and WEBB, H. W. 1947. *Phys. Rev.* **72**, 332.
 MICHELS, A. and GOUDEKET, M. 1941. *Physica*, **8**, 347.
 NATIONAL BUREAU OF STANDARDS. 1955. Circular 564, Tables of Thermal Properties of Gases (U.S. Department of Commerce, Washington, D.C.).
 ROBIN, J. 1954. *Compt. rend.* **238**, 1491.
 ROBIN, J. and ROBIN, S. 1951. *Compt. rend.* **233**, 928.
 SCHNEIDER, W. G. and DUFFIE, J. A. H. 1949. *J. Chem. Phys.* **17**, 751.
 SCHNETTLER, O. 1930. *Z. Physik*, **65**, 55.
 WEISSKOFF, V. 1933. *Physik. Z.* **34**, 1.

NOTES

A NOTE ON A PROOF BY DYSON

R. O. A. ROBINSON

In the second edition of his Cornell notes Dyson (1952) gives a simplified proof of the important theorem regarding the expansion in normal form of any simple product O of electron-positron and electromagnetic field operators. The object of this note is to point out an omission from the proof and to rectify it.

The theorem is stated as follows: "We define a factor-pairing of O by picking out from O a certain even number of factors, either all or none of any intermediate number, and associating them together in pairs. To each factor-pairing n corresponds a normal constituent O_n obtained as follows: for each pair of factors PQ which is paired in n , O_n contains the numerical factor $\langle PQ \rangle$ (the vacuum expectation value of the product PQ), the order of P and Q being maintained as it was in O . The remaining unpaired factors R_1, R_2, \dots appear in O_n rearranged in normal form, viz.

$$(1) \quad O_n = \pm \langle PQ \rangle \langle P'Q' \rangle \dots N(R_1 R_2 \dots),$$

the sign in front being $+$ or $-$ according to the even or odd character of the permutation of the electron-positron operators from the order in which they are written in O to the order in which they are written in equation 1. With this definition of O_n we have the following theorem. Every operator product O is identically equal to the sum of the O_n obtained from all its factor-pairings."

Let O be a product of m factors. Since from the definition of the normal product the theorem is trivially true for $m = 1$ and $m = 2$, it is only necessary to prove it true for arbitrary m assuming it true for $m-2$. This is done in two steps. First Dyson shows that if O' is an operator involving $m-2$ factors, the theorem is true for all

$$(2) \quad O = (PQ \mp QP)O'$$

where P and Q are field operators and where the plus sign appears only if P and Q are both electron-positron operators. Further, by using the *commutation rules* it is always possible to write

$$(3) \quad O = N(O) + \Sigma$$

where Σ is a sum of terms of type 2. The theorem is trivially true for $N(O)$. Since it is also true for Σ , the conclusion is made that it is true for O .

However, in order to make this complete it must be shown that expansions in accordance with the theorem are additive, i.e. Expansion of $A +$ Expansion of $B =$ Expansion of $(A + B)$, A and B being any two products. For example, let $P_1 Q_1$, $P_2 Q_2$, and PQ be products of two fermion operators satisfying the relation

$$(4) \quad P_1 Q_1 + P_2 Q_2 = PQ$$

and let O be any product. Expanding the products, PQO , and cancelling the appropriate terms, we must verify that

$$(5) \quad \langle P_1 L \rangle N(Q_1, O-L) - \langle Q_1 L \rangle N(P_1, O-L) \pm \langle P_1 L \rangle \langle Q_1 M \rangle N(O-L-M) \\ + \langle P_2 L \rangle N(Q_2, O-L) - \langle Q_2 L \rangle N(P_2, O-L) \pm \langle P_2 L \rangle \langle Q_2 M \rangle N(O-L-M) \\ = \langle PL \rangle N(Q, O-L) - \langle QL \rangle N(P, O-L) \pm \langle PL \rangle \langle QM \rangle N(O-L-M)$$

where L, M are factors of O , and $O-L, O-M, O-L-M$ represent the products obtained by omitting from O one or both factors. Both sides of equation 5 are to be summed over L and M . The \pm signs depend on the ordering of the fermion operators of O , but the point of importance is that, for any given ordering, they are either all $+$ or all $-$.

The complexity of equation 5 disappears if attention is restricted to the requirements of equation 3. We are concerned only with combinations effected by using the commutation relations. Thus factors are always combined in pairs as in 4 and the only case to be considered for fermion operators is:

$$(6) \quad P_1 = Q_2, \quad P_2 = Q_1, \quad P \text{ and } Q \text{ both } c\text{-numbers.}$$

Subject to these conditions, the right-hand side of equation 5 vanishes, since the vacuum expectation value of single operators is always zero. Substituting for P_2 and Q_2 and using the relation

$$(7) \quad \sum_{L,M} \langle Q_1 L \rangle \langle P_1 M \rangle N(O-L-M) = - \sum_{L,M} \langle P_1 L \rangle \langle Q_1 M \rangle N(O-L-M)$$

the left-hand side also vanishes. The minus sign on the right-hand side of equation 7 results from the interchange in position of the fermion operators* L and M in corresponding normal constituents in accordance with equation 1.

In the case where products of two boson operators are combined, we choose, analogously to equation 4,

$$(8) \quad P_1 Q_1 - P_2 Q_2 = PQ.$$

The conditions 6 remain unchanged while equation 5 becomes

$$(9) \quad \langle P_1 L \rangle N(Q_1, O-L) + \langle Q_1 L \rangle N(P_1, O-L) + \langle P_1 L \rangle \langle Q_1 M \rangle N(O-L-M) \\ - \langle P_2 L \rangle N(Q_2, O-L) - \langle Q_2 L \rangle N(P_2, O-L) - \langle P_2 L \rangle \langle Q_2 M \rangle N(O-L-M) \\ = \langle PL \rangle N(Q, O-L) + \langle QL \rangle N(P, O-L) + \langle PL \rangle \langle QM \rangle N(O-L-M).$$

In this case L and M must both be boson operators, since otherwise the vacuum expectation values vanish, and so the \pm signs do not arise. It is easy to see that equation 9 holds subject to the conditions 6. Finally, the proof remains essentially unchanged if instead of expanding products such as PQO we consider more general products of the form $OPQO'$. This completes the theorem as required.

*If L and M are not both fermion operators the corresponding terms in 7 vanish on account of the vacuum expectation values.

ACKNOWLEDGMENT

The grant of a Summer Research Fellowship by the National Research Council of Canada is gratefully acknowledged.

DYSON, F. J. 1952. *Advanced quantum mechanics*, 2nd ed. (Cornell Univ. Press, Ithaca, N.Y.).

RECEIVED 13 JULY, 1956.
DEPARTMENT OF MATHEMATICS,
UNIVERSITY OF TORONTO,
TORONTO, ONT., CANADA.

PREPARATION OF PURE LITHIUM SAMPLES
FOR ELECTRICAL MEASUREMENTS*

W. B. PEARSON

The normal method of preparing samples of the alkali metals for electrical measurements is to run the molten metal under vacuum into a soft-glass mold which has platinum leads sealed in at the required positions. It has, however, not been possible to use this method for preparing lithium samples because of the rapid reaction of molten lithium with the glass. Some attention has therefore been given to making special non-reactive glasses, and MacDonald and Stanworth (1950) have for instance shown that it is possible to prepare pure lithium samples in a special borate-clad glass, C 10.

We now find that pure lithium samples can be prepared in soft-glass molds by the following method. The lithium is first immersed in mineral oil (Stanolax) and cut to the appropriate size but then, instead of the Stanolax being washed off with benzene in the normal manner, it is rapidly mopped off the surface with cloth or absorbent paper before the metal is placed in the melting tube. The film of oil remaining on the surface of the lithium is sufficient to cover the surface of the melting tube and mold and prevent reaction, provided that the lithium is driven down into the mold with a small pressure of helium gas as soon as it has melted, and also that the specimen tube is immediately removed from the hot oil bath and placed in a cold oil bath. This can be done quite conveniently and a pure specimen with a clean shiny surface is obtained. If, however, the metal is not quenched, it starts to react with the glass in a few seconds and the shiny metal-glass interface turns dark brown.

The residual resistance ratio of a specimen prepared in this manner for Hall effect measurements was 1.9×10^{-3} , compared with 1.5×10^{-3} for an extruded wire of lithium of rather similar initial purity.

MACDONALD, D. K. C. and STANWORTH, J. E. 1950. *Proc. Phys. Soc. B*, **63**, 455.

RECEIVED OCTOBER 5, 1956.
DIVISION OF PURE PHYSICS,
NATIONAL RESEARCH COUNCIL,
OTTAWA, CANADA.

*Issued as N.R.C. No. 4154.

HEIGHT-GAIN IN THE FORWARD-SCATTERING OF RADIO WAVES BY METEOR TRAILS*

C. O. HINES AND M. O'GRADY

Radio signals in the V.H.F. band can be transmitted over long paths by means of forward-scattering from meteor trails (Forsyth and Vogan 1955). Even if the parent meteors were incident on the atmosphere uniformly and isotropically, the trails which are effective in the scattering process would not be distributed uniformly. Instead, various observational effects tend to emphasize the contribution from certain regions of the sky and suppress that from others. The factors involved are fairly well understood, and contour charts of the relevant distribution functions have been presented (Eshleman and Manning 1954; Hines and Pugh 1956). In particular, regions somewhat to either side of the great circle path tend to dominate the distribution.

The observed occurrence rate of useful meteors and the mean received signal level will, of course, depend on the particular antenna systems employed. The dependence can be predicted theoretically by combining the antenna illumination pattern at the meteoric height \mathfrak{S} with the pertinent distribution function, and then integrating the product, for each assumed antenna system in turn.

Typical results of this process have been presented (Hines, Forsyth, Vogan, and Pugh 1955), to illustrate the effect of various changes in the azimuthal gain pattern. In those calculations, simplified single-lobed vertical gain patterns were adopted for both transmitter and receiver, with elevations such that the maxima of the two antenna beams intersected at the \mathfrak{S} level, and \mathfrak{S} was taken to be 100 km.

It is by no means evident that the optimum elevation angle for meteoric scattering is the one previously adopted. Moreover, while 100 km. is a typical height for meteors, it is by no means exclusive; fairly wide variations must be anticipated, particularly towards lower values. At the suggestion of Dr. P. A. Forsyth, a new set of computations was undertaken to investigate the effect of variations in elevation angle and in \mathfrak{S} . The results of the computations are summarized here.

A relatively refined antenna pattern was assumed in this work, where the amplitude gain function was of the form

$$\sin[(2\pi h/\lambda) \sin e] \frac{\sin[(\pi a/\lambda) \sin e]}{\sin e} \frac{\sin[(\pi b/\lambda) \cos e \sin \alpha]}{\cos e \sin \alpha}$$

This is the Fraunhofer form appropriate to an effective aperture of vertical dimension a and horizontal dimension b , radiating at wavelength λ , and situated at a height h above a perfectly conducting ground. The normal to the aperture lies in the great circle direction towards the opposite end of the transmission path; e measures elevation above the local horizontal plane, and α

*The work was performed under project PCC. No. D48-95-11-01.

measures azimuth from the great circle direction. The antennas contemplated were five-element Yagis mounted horizontally, with vertical beam width (between half-power points) of 64° and horizontal beam width of 50° , corresponding to $a = 0.84\lambda$ and $b = 1.05\lambda$. For the range of h 's considered, the first factor in the gain expression gives rise to the dominant variation with elevation angle. It results, of course, from the reflective interference introduced by the ground, and more than one of its lobes must be taken into account in obtaining a proper estimate of height-gain in meteoric scattering.

The values $\mathfrak{S} = 80, 90, 100$, and 110 km. were adopted in succession. In each case, the azimuths and elevations were determined for a large number of points at the \mathfrak{S} level, and the corresponding antenna gains were calculated both for the transmitting and for the receiving antenna, assuming a transmitter-receiver separation of 1000 km. This was repeated for several values of h in turn, to give the effect of changing antenna heights. The resultant set of illumination patterns was then combined, each pattern in turn, with the contour charts giving the distribution of observable meteors and of mean signal sources, and the products in turn were integrated over the \mathfrak{S} level. (The charts employed, those drawn as solid lines by Hines and Pugh, were based on an assumed \mathfrak{S} of 100 km.; but they are not expected to be as strongly dependent on \mathfrak{S} as are the gain functions, so their continued use seems justified.)

The results of this synthesis are displayed by the solid-line curves in Fig. 1. The first column of graphs indicates the variation, with antenna height and with meteoric height, in the number of meteors detected with received signals exceeding some arbitrary counting level. The second depicts the corresponding variations in mean signal level, or in total duration above a counting level. The scales of ordinates in the two columns are arbitrary, but they are consistent from one row to the next. The heights, h_0 , at which the antennas would have to be placed to get maxima intersecting at the appropriate \mathfrak{S} level are indicated by arrowheads on the horizontal axis.

On the whole, the graphs speak for themselves, but a few points may be emphasized. The dominant feature of each curve is the hump which appears, centered on a height near h_0 , and attributable to a degree of intermeshing of the two main antenna beams at the meteoric level. As h increases beyond h_0 , subsidiary antenna lobes play a more important part, and the fall-off is not as rapid as might have been expected; in fact, a secondary maximum arises for large \mathfrak{S} . This behavior suggests that the form of the curves is dominated by the variations in antenna illumination alone. The modifying effects of the distribution functions are appreciable, however, as is indicated by the differences between corresponding members of the two columns.

In addition to the symmetrical situation so far considered, with the two antennas at the same height, calculations were made on the assumption of different antenna heights. Typical curves are shown for the $\mathfrak{S} = 90$ and 100 km. levels. These obtain when one antenna is maintained at a height of 1.3λ (dotted curves) or 2.2λ (broken curves), the other antenna being allowed to vary in height.

Meteor trails are produced, on the average, at greater heights in the morning

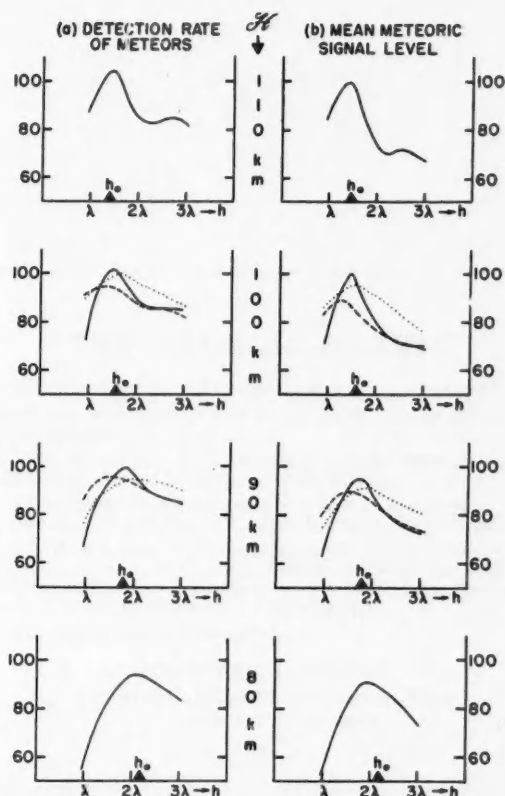


FIG. 1. Height-gain in meteoric forward-scattering. The ordinates indicate, on arbitrary scales, (a) the detection rate of meteors above a counting level and (b) the mean signal strength obtained by meteoric scattering, for various heights H of the meteor level and for a range of heights h of the antennas.

hours and at lesser heights in the afternoon hours. Accordingly, with fixed heights for the antennas, a diurnal variation will be introduced in the apparent meteoric rate and mean signal strength as a result of H changes alone, quite apart from actual variations in the absolute meteoric rate. In this connection, it should be noted that the mean signal level is inversely proportional to the ambipolar diffusion coefficient, which may be expected to increase by a factor of four as the H level increases by 10 km.; this change has *not* been incorporated in the graphs.

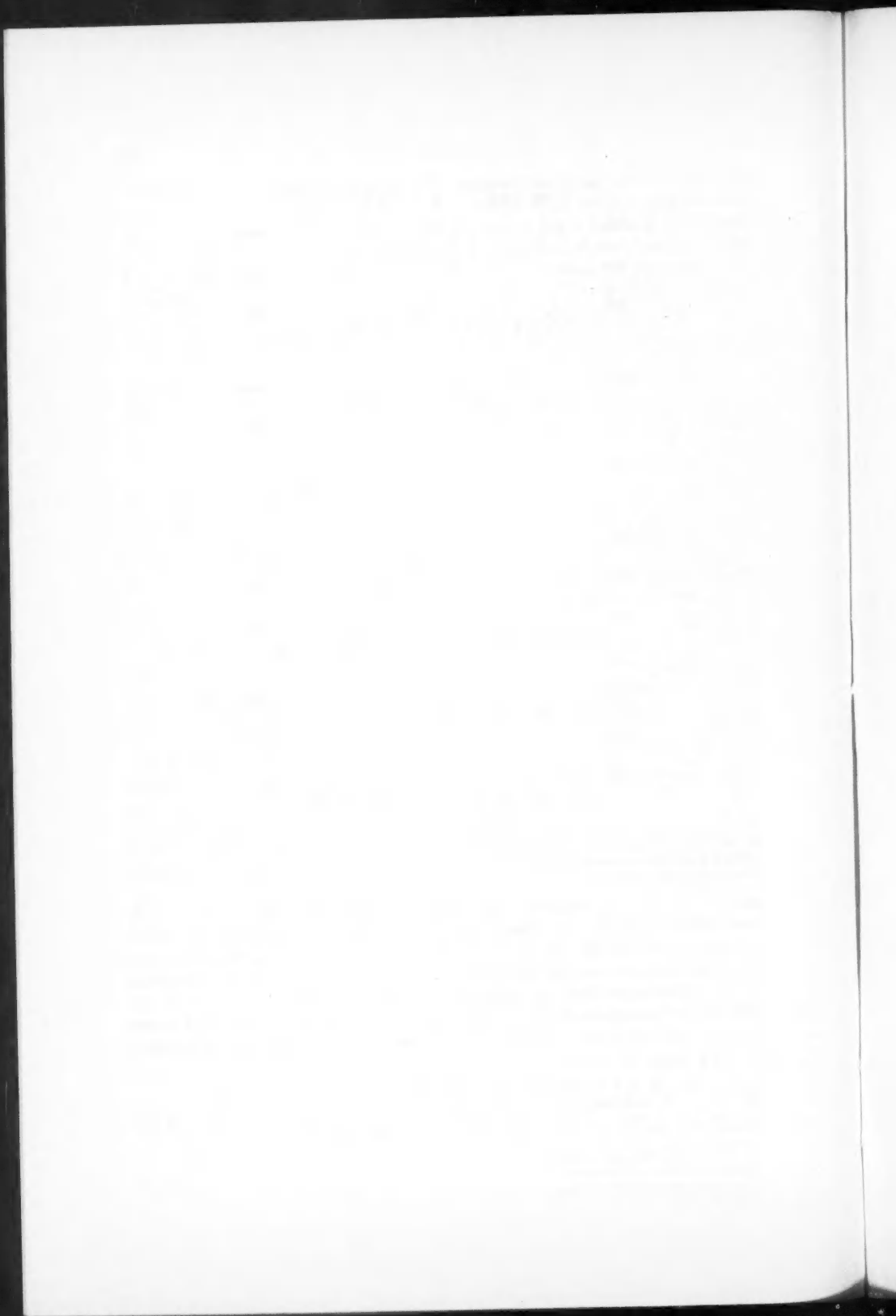
ESHLEMAN, V. R. and MANNING, L. A. 1954. *Proc. Inst. Radio Engrs.* **42**, 530.

FORSYTH, P. A. and VOGAN, E. L. 1955. *Can. J. Phys.* **33**, 176.

HINES, C. O., FORSYTH, P. A., VOGAN, E. L., and PUGH, R. E. 1955. *Can. J. Phys.* **33**, 609.

HINES, C. O. and PUGH, R. E. 1956. *Can. J. Phys.* **34**, 1005.

RECEIVED SEPTEMBER 17, 1956.
RADIO PHYSICS LABORATORY,
DEFENCE RESEARCH BOARD,
OTTAWA, CANADA.



THE PHYSICAL SOCIETY

MEMBERSHIP of the Society is open to all who are interested in Physics.

FELLOWS pay an Entrance fee of £1 1s. (\$3.00) and an Annual Subscription of £2 2s. (\$6.00).

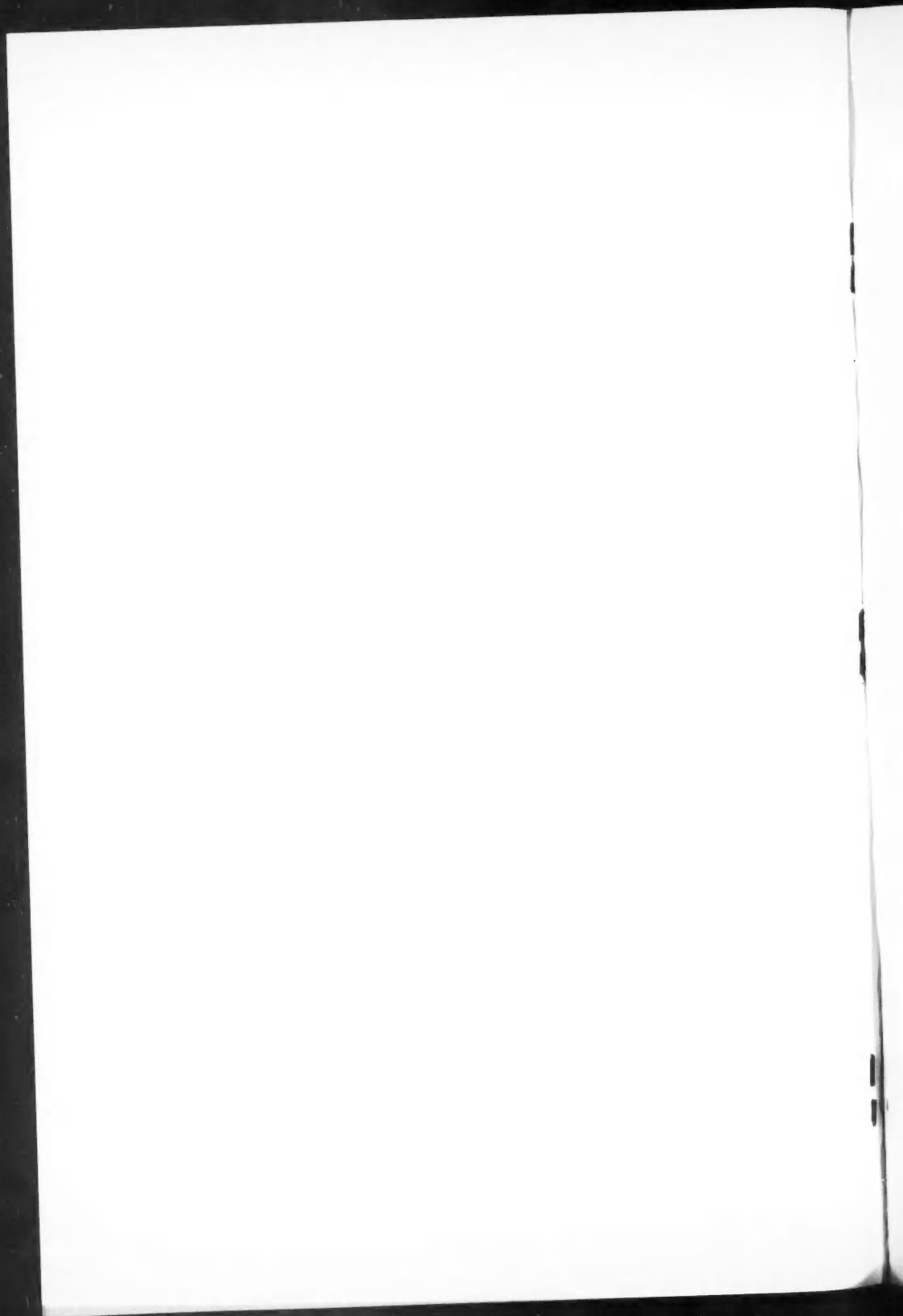
STUDENTS: A candidate for Studentship must be between the ages of 18 and 26, and pays an Annual Subscription of 5s. (\$0.75).

MEETINGS: Fellows and Students may attend all Meetings of the Society including the annual Exhibition of Scientific Instruments and Apparatus.

PUBLICATIONS include the *Proceedings of the Physical Society*, published monthly in two sections, and *Reports on Progress in Physics*, published annually. Volume XVIII, 1955, is now available (price 50s. (\$7.15)). Members are entitled to receive many of the Publications at a reduced rate.

Further information can be obtained from:

THE PHYSICAL SOCIETY
1, LOWTHER GARDENS, PRINCE CONSORT ROAD
LONDON, S.W.7, ENGLAND



CANADIAN JOURNAL OF PHYSICS

Notes to Contributors

Manuscripts

(i) **General.** Manuscripts, in English or French, should be typewritten, double spaced, on paper $8\frac{1}{2} \times 11$ in. **The original and one copy are to be submitted.** Tables and captions for the figures should be placed at the end of the manuscript. Every sheet of the manuscript should be numbered.

Style, arrangement, spelling, and abbreviations should conform to the usage of this journal. Names of all simple compounds, rather than their formulas, should be used in the text. Greek letters or unusual signs should be written plainly or explained by marginal notes. Superscripts and subscripts must be legible and carefully placed.

Manuscripts and illustrations should be carefully checked before they are submitted. Authors will be charged for unnecessary deviations from the usual format and for changes made in the proof that are considered excessive or unnecessary.

(ii) **Abstract.** An abstract of not more than about 200 words, indicating the scope of the work and the principal findings, is required, except in Notes.

(iii) **References.** References should be listed **alphabetically by authors' names**, unnumbered, and typed after the text. The form of the citations should be that used in issues of this journal published in 1956; in references to papers in periodicals, titles should not be given and only initial page numbers are required. The names of periodicals should be abbreviated in the form given in the most recent *List of Periodicals Abstracted by Chemical Abstracts*. All citations should be checked with the original articles and each one referred to in the text by the authors' names and the year.

(iv) **Tables.** Tables should be numbered in roman numerals and each table referred to in the text. Titles should always be given but should be brief; column headings should be brief and descriptive matter in the tables confined to a minimum. Vertical rules should be used only when they are essential. Numerous small tables should be avoided.

Illustrations

(i) **General.** All figures (including each figure of the plates) should be numbered consecutively from 1 up, in arabic numerals, and each figure referred to in the text. The author's name, title of the paper, and figure number should be written in the lower left corner of the sheets on which the illustrations appear. Captions should not be written on the illustrations (see Manuscripts (i)).

(ii) **Line Drawings.** Drawings should be carefully made with India ink on white drawing paper, blue tracing linen, or co-ordinate paper ruled in blue only; any co-ordinate lines that are to appear in the reproduction should be ruled in black ink. Paper ruled in green, yellow, or red should not be used unless it is desired to have all the co-ordinate lines show. All lines should be of sufficient thickness to reproduce well. Decimal points, periods, and stippled dots should be solid black circles large enough to be reduced if necessary. Letters and numerals should be neatly made, preferably with a stencil (**do NOT use typewriting**) and be of such size that the smallest lettering will be not less than 1 mm. high when reproduced in a cut 3 in. wide.

Many drawings are made too large; originals should not be more than 2 or 3 times the size of the desired reproduction. In large drawings or groups of drawings the ratio of height to width should conform to that of a journal page but the height should be adjusted to make allowance for the caption.

The original drawings and one set of clear copies (e.g. small photographs) are to be submitted.

(iii) **Photographs.** Prints should be made on glossy paper, with strong contrasts. They should be trimmed so that essential features only are shown and mounted carefully, with rubber cement, on white cardboard with no space or only a very small space (less than 1 mm.) between them. In mounting, full use of the space available should be made (to reduce the number of cuts required) and the ratio of height to width should correspond to that of a journal page ($4\frac{1}{2} \times 7\frac{1}{2}$ in.); however, allowance must be made for the captions. Photographs or groups of photographs should not be more than 2 or 3 times the size of the desired reproduction.

Photographs are to be submitted in duplicate; if they are to be reproduced in groups one set should be mounted, the duplicate set unmounted.

Reprints

A total of 50 reprints of each paper, without covers, are supplied free. Additional reprints, with or without covers, may be purchased.

Charges for reprints are based on the number of printed pages, which may be calculated approximately by multiplying by 0.6 the number of manuscript pages (double-spaced typewritten sheets, $8\frac{1}{2} \times 11$ in.) and including the space occupied by illustrations. An additional charge is made for illustrations that appear as coated inserts. The cost per page is given on the reprint requisition which accompanies the galley.

Any reprints required in addition to those requested on the author's reprint requisition form must be ordered officially as soon as the paper has been accepted for publication.

Contents

	Page
Higher-order Focusing in the $\pi\sqrt{2}$ β -Spectrometer— <i>G. E. Lee-Whiting and E. A. Taylor</i> - - - - -	1
Half-life Determination of Some Radionuclides— <i>W. F. Merritt, P. J. Campion, and R. C. Hawkings</i> - - - - -	16
Spallation Yields from High Energy Proton Bombardment of Heavy Elements— <i>J. D. Jackson</i> - - - - -	21
The Effects of Grain Boundaries on the Plastic Deformation of Zinc Crystals— <i>G. B. Craig and B. Chalmers</i> - - - - -	38
Numerical Analysis of a Unitary Particle Model— <i>F. A. Kaempffer and Edith M. Kennedy</i> - - - - -	48
Multilayer Problems in the Spherical Harmonics Method— <i>B. Davison</i> - - - - -	55
The Emission Spectrum of AlF in the Vacuum Ultraviolet— <i>S. M. Naudé and T. J. Hugo</i> - - - - -	64
The Spectrum of Silicon Hydride— <i>A. E. Douglas</i> - - - - -	71
The Freezing Points of High Purity Metals as Precision Temperature Standards. I. Precision Measurements with Standard Resistance Thermometers— <i>E. H. McLaren</i> - - - - -	78
Properties of Gallium Indium Antimonide— <i>J. S. Blakemore</i> - - - - -	91
Selective Reflection from Mercury Vapor at High Pressures— <i>J. A. Galt and H. L. Welsh</i> - - - - -	98
Influence of Foreign Gases at High Pressures on the Selective Reflection from Mercury Vapor— <i>J. A. Galt and H. L. Welsh</i> - - - - -	114
 Notes:	
A Note on a Proof by Dyson— <i>R. O. A. Robinson</i> - - - - -	122
Preparation of Pure Lithium Samples for Electrical Measurements— <i>W. B. Pearson</i> - - - - -	124
Height-gain in the Forward-scattering of Radio Waves by Meteor Trails— <i>C. O. Hines and M. O'Grady</i> - - - - -	125

